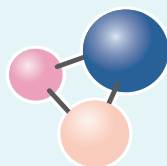


ISSN 1997-308X
eISSN 2412-8767

ИЗВЕСТИЯ ВУЗОВ



ПОРОШКОВАЯ МЕТАЛЛУРГИЯ
И ФУНКЦИОНАЛЬНЫЕ ПОКРЫТИЯ

POWDER METALLURGY
AND FUNCTIONAL COATINGS

2024

Том 18 № 3
Vol. No.

powder.misis.ru

ISSN 1997-308X
eISSN 2412-8767

POWDER METALLURGY AND FUNCTIONAL COATINGS

Scientific and Technical Journal
Founded in 2007
Six issues per year

2024

Том 18 № 3
Vol. 18 No. 3

ИЗВЕСТИЯ ВУЗОВ ПОРОШКОВАЯ МЕТАЛЛУРГИЯ И ФУНКЦИОНАЛЬНЫЕ ПОКРЫТИЯ

Научно-технический журнал
Основан в 2007 г.
Выходит 6 раз в год

POWDER METALLURGY AND FUNCTIONAL COATINGS

SCIENTIFIC AND TECHNICAL JOURNAL
FOUNDED IN 2007
SIX ISSUES PER YEAR

<http://powder.misis.ru>

ISSN 1997-308X
eISSN 2412-8767



Founder: National University of Science
and Technology "MISIS"

Address: 4 bld. 1 Leninskiy Pros., Moscow 119049, Russian Federation
<http://www.misis.ru>

Editor-in-Chief

Evgeny A. Levashov

Prof., Dr. Sci. (Eng.), Acad. of the RANS, NUST MISIS, Moscow, Russian Federation

Journal is included into the List of peer-reviewed scientific publications recommended by the Highest Attestation Commission
of the Ministry of Education and Science of the Russian Federation for publishing the results of doctoral and candidate dissertations.
Abstracting/Indexing: Scopus, Russian Science Citation Index (RSCI), Ulrich's Periodicals Directory, VINITI Database (Abstract Journal).

Editorial Board

M. I. Alymov – Dr. Sci. (Eng.), Corresponding Member of the RAS, Merzhanov Institute of Structural Macrokinetics and Materials Sciences of the RAS, Chernogolovka, Russia
A. P. Amosov – Prof., Dr. Sci. (Phys.-Math.), Samara State Technical University, Samara, Russia
G. A. Bagliuk – Prof., Dr. Sci. (Eng.), Acad. of the NASU, IPMS NASU, Kiev, Ukraine
I. V. Blinkov – Prof., Dr. Sci. (Eng.), NUST MISIS, Moscow, Russia
M. V. Chukin – Prof., Dr. Sci. (Eng.), Magnitogorsk State Technical University, Magnitogorsk, Russia
H. Danning – Prof., Dr. Sci., Vienna University of Technology, Vienna, Austria
B. Derin – Assoc. Prof., Dr. Sci. (Phil.), Istanbul Technical University, Maslak, Istanbul, Turkey
V. Yu. Dorofeyev – Prof., Dr. Sci. (Eng.), South-Russian State Polytechnical University (NPI), Novocherkassk, Russia
Yu. Estrin – Prof., Dr. Sci. (Nat.), Monash University, Clayton, Australia
A. Ph. Ilyushchanka – Prof., Dr. Sci. (Eng.), Acad. of the NAS of Belarus, State Research and Production Powder Metallurgy Association, Minsk, Belarus
Yu. R. Kolobov – Prof., Dr. Sci. (Phys.-Math.), Federal Research Center of Problems of Chemical Physics and Medicinal Chemistry of the RAS, Chernogolovka, Russia
V. S. Komlev – Prof., Dr. Sci. (Eng.), Corresponding Member of the RAS, Institute of Metallurgy of the RAS, Moscow, Russia
I. Konyashin – Prof., Dr. Sci. (Econ.), Element Six GmbH, Burghaun, Germany
Yu. M. Korolyov – Prof., Dr. Sci. (Eng.), Scientific and Technical Association "Powder Metallurgy", Moscow, Russia
D. Yu. Kovalev – Dr. Sci. (Phys.-Math.), Merzhanov Institute of Structural Macrokinetics and Materials Sciences of the RAS, Chernogolovka, Russia
S. A. Kulinich – Assoc. Prof., PhD (Chem.), Tokai University, Hiratsuka, Kanagawa, Japan
S. V. Kuzmin – Prof., Dr. Sci. (Eng.), Corresponding Member of the RAS, Volgograd State Technical University, Volgograd, Russia
V. P. Kuznetsov – Prof., Dr. Sci. (Eng.), Ural Federal University, Ekaterinburg, Russia
Yu. V. Levinsky – Prof., Dr. Sci. (Eng.) Merzhanov Institute of Structural Macrokinetics and Materials Sciences of the RAS, Chernogolovka, Russia
A. E. Ligachyov – Prof., Dr. Sci. (Phys.-Math.), Prokhorov General Physics Institute of the RAS, Moscow, Russia
V. Yu. Lopatin – Cand. Sci., NUST MISIS, Moscow, Russia
A. A. Lozovan – Prof., Dr. Sci. (Eng.), Moscow Aviation Institute (NRU), Moscow, Russia

V. I. Lysak – Prof., Dr. Sci. (Eng.), Acad. of the RAS, Volgograd State Technical University, Volgograd, Russia
A. V. Makarov – Dr. Sci. (Eng.), Corresponding Member of the RAS, M.N. Mikheev Institute of Metal Physics of the Ural Branch of the RAS, Ural Federal University, Ekaterinburg, Russia
L. L. Mishnaevsky – Dr. Habil. (Eng.), Technical University of Denmark, Roskilde, Denmark
A. S. Mukasyan – Prof., Dr. Sci. (Phys.-Math.), University of Notre Dame, Notre Dame, USA
S. A. Ogлезneva – Prof., Dr. Sci. (Eng.), Perm National Research Polytechnical University, Perm, Russia
R. Orrù – Prof., Dr. Sci. (Eng.), University of Cagliari, Cagliari, Italy
I. B. Panteleev – Prof., Dr. Sci. (Eng.), St. Petersburg State Technological Institute (Technical University), St. Petersburg, Russia
F. Peizhong – Prof., Dr. Sci., China University of Mining and Technology, Xuzhou, P.R. China
C. Pengwan – Prof., Dr. Sci., Beijing Institute of Technology, Beijing, P.R. China
M. I. Petrzhik – Dr. Sci. (Eng.), NUST MISIS, Moscow, Russia
Yu. S. Pogozhev – Assoc. Prof., Cand. Sci. (Eng.), NUST MISIS, Moscow, Russia
V. V. Polyakov – Prof., Dr. Sci. (Phys.-Math.), Altai State University, Barnaul, Russia
A. A. Popovich – Prof., Dr. Sci. (Eng.), Corresp. Member of the RANS, St. Petersburg State Polytechnical University (National Research University), St. Petersburg, Russia
S. E. Porozova – Dr. Sci. (Eng.), Perm National Research Polytechnical University, Perm, Russia
A. A. Rempel – Prof., Dr. Sci. (Phys.-Math.), Acad. of the RAS, Institute of Metallurgy of the Ural Branch of the RAS, Ekaterinburg, Russia
F. Rustichelli – Prof., Dr. Sci. (Phys.), University of Marches, Ancona, Italy
S. D. Shlyapin – Prof., Dr. Sci. (Eng.), Moscow Aviation Institute (NRU), Moscow, Russia
D. V. Shtansky – Prof., Dr. Sci. (Phys.-Math.), NUST MISIS, Moscow, Russia
A. N. Timofeev – Dr. Sci. (Eng.), JSC "Komposite", Korolev, Russia
P. A. Vityaz' – Prof., Dr. Sci. (Eng.), Acad. of the NAS of Belarus, Minsk, Belarus
A. A. Zaitsev – Assoc. Prof., Cand. Sci. (Eng.), NUST MISIS, Moscow, Russia
Zheng YongTing – Prof., Dr. Sci., Harbin Institute of Technology, Harbin, P.R. China
F. Zhengyi – Prof., Dr. Sci., Wuhan University of Technology, Wuhan, P.R. China

Editorial Staff

Address: NUST MISIS,
4 bld. 1 Leninskiy Pros., Moscow 119049, Russian Federation

Phone: +7 (495) 638-45-35. E-mail: izv.vuz@misis.ru

Certificate of registration No. FS77-27955 (12.04.2007)

Re-registration PI No. FS77-79230 (25.09.2020)



PM & FC © NUST MISIS, Moscow, 2024



Articles are available under Creative Commons
Attribution Non-Commercial No Derivatives

Leading Editor: A.A. Kudinova

Executive Editor: O.V. Sosnina

Layout Designer: V.V. Rasenets

Signed print 20.06.2024. Format 60×90 1/8

Offset paper No. 1. Digital printing. Quires 10.75

Order 20000. Free price

Printed in the printing house of the MISIS Publish House

4 bld. 1 Leninskiy Pros., Moscow, 119049 Russian Federation

Phone/fax: +7 (499) 236-76-17

ИЗВЕСТИЯ ВУЗОВ ПОРОШКОВАЯ МЕТАЛЛУРГИЯ И ФУНКЦИОНАЛЬНЫЕ ПОКРЫТИЯ

ISSN 1997-308X
eISSN 2412-8767



Учредитель:

ФГАОУ ВО Национальный исследовательский
технологический университет «МИСИС»

Адрес: 119049, Москва, Ленинский пр-т, 4, стр. 1

<https://www.misis.ru>

Главный редактор

Евгений Александрович Левашов

д.т.н., академик РАН, профессор, НИТУ МИСИС, г. Москва

НАУЧНО-ТЕХНИЧЕСКИЙ ЖУРНАЛ

ОСНОВАН В 2007 Г.

ВЫХОДИТ 6 РАЗ В ГОД

<http://powder.misis.ru>

Журнал включен в Перечень рецензируемых научных изданий, рекомендованных ВАК Минобрнауки РФ
для публикации результатов диссертаций на соискание ученых степеней.

Журнал включен в базы данных: Scopus, Russian Science Citation Index (RSCI), Ulrich's Periodicals Directory, РИНЦ, БД/РЖ ВИНТИ.

Редакционная коллегия

М. И. Алымов – д.т.н., чл.-корр. РАН, проф., ИСМАН, г. Черноголовка
А. П. Амосов – д.ф.-м.н., проф., СамГТУ, г. Самара
Г. А. Баглюк – д.т.н., акад. НАНУ, проф., ИПМ НАН Украины, г. Киев
И. В. Блинков – д.т.н., проф., НИТУ МИСИС, г. Москва
П. А. Витязь – д.т.н., акад. НАНБ, проф., НАН Беларуси, г. Минск
В. Ю. Дорофеев – д.т.н., проф., ЮРГПУ (НПИ), г. Новочеркасск
А. А. Зайцев – к.т.н., доц., НИТУ МИСИС, г. Москва
А. Ф. Ильющенко – д.т.н., акад. НАН Беларуси, проф.,
ГНПО ПМ НАН Беларуси, г. Минск
Д. Ю. Ковалев – д.ф.-м.н., ИСМАН, г. Черноголовка
Ю. Р. Колобов – д.ф.-м.н., проф., ФИЦ ПХФ и МХ РАН, г. Черноголовка
В. С. Комлев – д.т.н., чл.-корр. РАН, проф., ИМЕТ РАН, г. Москва
Ю. М. Королев – д.т.н., проф., НТА «Порошковая металлургия»,
г. Москва
В. П. Кузнецов – д.т.н., проф., УрФУ, г. Екатеринбург
С. В. Кузьмин – д.т.н., чл.-корр. РАН, проф., ВолгГТУ, г. Волгоград
Ю. В. Левинский – д.т.н., проф., ИСМАН, г. Черноголовка
А. Е. Лигачев – д.ф.-м.н., проф., ИОФ РАН, г. Москва
А. А. Лозован – д.т.н., проф., МАИ (НИУ), г. Москва
В. Ю. Лопатин – к.т.н., доц., НИТУ МИСИС, г. Москва
В. И. Лысак – д.т.н., акад. РАН, проф., ВолгГТУ, г. Волгоград
А. В. Макаров – д.т.н., чл.-корр. РАН, ИФМ УрО РАН, УрФУ,
г. Екатеринбург
С. А. Оглезнева – д.т.н., проф., ПНИПУ, г. Пермь
И. Б. Пантелеев – д.т.н., проф., СПбГТИ (ТУ), г. Санкт-Петербург
М. И. Петриж – д.т.н., проф., НИТУ МИСИС, г. Москва
Ю. С. Погужев – к.т.н., доц., НИТУ МИСИС, г. Москва
В. В. Поляков – д.ф.-м.н., проф., АлтГУ, г. Барнаул
А. А. Попович – д.т.н., чл.-корр. РАН, проф., СПбГПУ,
г. Санкт-Петербург

С. Е. Порозова – д.т.н., проф., ПНИПУ, г. Пермь
А. А. Ремпель – д.ф.-м.н., акад. РАН, проф., ИМЕТ УрО РАН,
г. Екатеринбург
А. Н. Тимофеев – д.т.н., АО «Композит», г. Королев
М. В. Чукин – д.т.н., проф., МГТУ, г. Магнитогорск
С. Д. Шляпин – д.т.н., проф., МАИ (НИУ), г. Москва
Д. В. Штанский – д.ф.-м.н., проф., НИТУ МИСИС, г. Москва
H. Danning – Dr. Sci., Prof., Vienna University of Technology,
Vienna, Austria
B. Derin – Dr. Sci. (Phil.), Assoc. Prof., Istanbul Technical University,
Maslak, Istanbul, Turkey
Yu. Estrin – Dr. Sci. (Nat.), Prof., Monash University, Clayton, Australia
I. Konyashin – Dr. Sci. (Econ.), Prof., Element Six GmbH, Burghausen,
Germany
S. A. Kulinich – PhD (Chem.), Associate Prof., Tokai University, Hiratsuka,
Kanagawa, Japan
L. L. Mishnaevsky – Dr. Habil. (Eng.), Technical University of Denmark,
Roskilde, Denmark
A. S. Mukasyan – Dr. Sci. (Phys.-Math.), Prof., University of Notre Dame,
Notre Dame, USA
R. Orrù – Dr. Sci. (Eng.), Prof., University of Cagliari, Cagliari, Italy
F. Peizhong – Dr. Sci., Prof., China University of Mining and Technology,
Xuzhou, P.R. China
C. Pengwan – Dr. Sci., Prof., Beijing Institute of Technology,
Beijing, P.R. China
F. Rusticelli – Dr. Sci. (Phys.), Prof., University of Marches, Ancona, Italy
Zheng YongTing – Dr. Sci., Prof., Harbin Institute of Technology, Harbin,
P.R. China
F. Zhengyi – Dr. Sci., Prof., Wuhan University of Technology, Wuhan,
P.R. China

Редакция журнала

Адрес: 119049, Москва,
Ленинский пр-т, 4, стр. 1. НИТУ МИСИС

Тел.: +7 (495) 638-45-35. Эл. почта: izv.vuz@misis.ru

Свидетельство о регистрации № ФС77-27955 от 12.04.2007 г.
Перерегистрация 25.09.2020 г. ПИ № ФС77-79230



© НИТУ МИСИС, Москва, 2024



Статьи доступны под лицензией Creative Commons
Attribution Non-Commercial No Derivatives

Ведущий редактор: А.А. Кудинова
Выпускающий редактор: О.В. Соснина
Дизайн и верстка: В.В. Расенец

Подписано в печать 20.06.2024. Формат 60×90 1/8
Бум. офсетная № 1. Печать цифровая. Усл. печ. л. 10,75
Заказ 20000. Цена свободная
Отпечатано в типографии Издательского Дома МИСИС
119049, г. Москва, Ленинский пр-т, 4, стр. 1
Тел./факс: +7 (499) 236-76-17

Contents



Содержание

Production Processes
and Properties of Powders

- Avdeeva Yu.A., Luzhkova I.V.,
Murzakaev A.M., Ermakov A.N.
Plasma-chemical synthesis of highly dispersed
core-shell structures from a mechanical mixture
of titanium carbide and titanium nickelide 5

Theory and Processes of Formation
and Sintering of Powder Materials

- Dorofeyev V.Yu., Bessarabov E.N., Sviridova A.N.,
Ivanova I.V., Svistun L.I., Vodolazhenko R.A.
Structure and properties of hot-forged
powder steel-bronze bimetal with SiC additives 16

Refractory, Ceramic,
and Composite Materials

- Pesin V.A., Vasilyeva M.V., Osmakov A.S.
Features of the linear intercept method used
for measuring the grain size in WC-Co hardmetals 28

- Suvorova V.S., Nepapushev A.A.,
Suvorov D.S., Kuskov K.V., Moskovskikh D.O.
Self-propagating high-temperature synthesis
and spark plasma sintering of high-entropy
(Hf,Ta,Nb)(C,N) carbonitride 38

Porous Materials and Biomaterials

- Ageeva M.V., Demin V.A., Demina T.V.
Physical and mathematical model of the silicon
vapor transport during high-temperature silicification
of a porous carbon media 49

Materials and Coatings Fabricated Using
the Additive Manufacturing Technologies

- Farber E.M., Borisov E.V., Popovich A.A.
Features of obtaining TiNi alloy samples
from commercial powders with high oxygen content
using the SLM technique 62

- Bubnenkov B.B., Zharmukhambetov A.S.,
Ivanov I.A., Yudin A.V., Taktashov A.E.,
Starkov A.M., Sharapov I.S., Alekseeva E.M.
Investigation of influence of technological
parameters on the properties of SiC samples fabricated
by selective laser sintering. Part 1 71

Процессы получения
и свойства порошков

- Авдеева Ю.А., Лужкова И.В.,
Мурзакаев А.М., Ермаков А.Н.
Плазмохимический синтез высокодисперсных
структур «ядро-оболочка» из механической смеси
карбида титана с никелидом титана 5

Теория и процессы формования
и спекания порошковых материалов

- Дорофеев В.Ю., Бессарабов Е.Н., Свиридова А.Н.,
Иванова И.В., Свистун Л.И., Водолаженко Р.А.
Структура и свойства горячештампованного
порошкового биметалла типа «сталь-бронза»
с добавками SiC 16

Тугоплавкие, керамические
и композиционные материалы

- Песин В.А., Васильева М.В., Осмаков А.С.
Особенности метода секущих, используемого
для определения размера зерна в сплавах WC-Co 28

- Суворова В.С., Непанушев А.А.,
Суворов Д.С., Кусков К.В., Московских Д.О.
Самораспространяющийся высокотемпературный
синтез и искровое плазменное спекание
высокоэнтропийного карбонитрида (Hf,Ta,Nb)(C,N) 38

Пористые материалы и биоматериалы

- Агеева М.В., Демин В.А., Демина Т.В.
Физико-математическая модель доставки
паров кремния в ходе высокотемпературного
силицирования пористых углеродных материалов 49

Материалы и покрытия, получаемые
методами аддитивных технологий

- Фарбер Э.М., Борисов Е.В., Попович А.А.
Особенности получения образцов сплава TiNi
методом СЛС из коммерческих порошков
с повышенным содержанием кислорода 62

- Бубнёнков Б.Б., Жармухамбетов А.С.,
Иванов И.А., Юдин А.В., Такташов А.Е.,
Старков А.М., Шарапов И.С., Алексеева Е.М.
Исследование влияния технологических параметров
на свойства образцов из SiC, получаемых методом
селективного лазерного спекания. Часть 1 71



UDC 546.261'82'74-047.84-022.532

<https://doi.org/10.17073/1997-308X-2024-3-5-15>Research article
Научная статья

Plasma-chemical synthesis of highly dispersed core-shell structures from a mechanical mixture of titanium carbide and titanium nickelide

Yu. A. Avdeeva¹ , I. V. Luzhkova¹, A. M. Murzakaev², A. N. Ermakov¹¹ Institute of Solid State Chemistry, Ural Branch, Russian Academy of Sciences
91 Pervomaiskaya Str., Yekaterinburg, Sverdlovsk Region 620990, Russia² Institute of Electrophysics, Ural Branch, Russian Academy of Sciences
106 Amundsen Str., Yekaterinburg, Sverdlovsk Region 620216, Russia y-avdeeva@list.ru

Abstract. In this paper, we studied the formation of ultrafine and nanocrystalline core-shell structures based on refractory compounds of titanium with nickel during plasma-chemical synthesis of a mechanical mixture of TiC and TiNi in a low-temperature nitrogen plasma. Cooling took place in an intensely swirling nitrogen flow in a quenching chamber. The derived products were separated in a vortex-type cyclone and a bag-type fabric filter. After processing, the products were subjected to encapsulation aimed at reducing the pyrophoricity for long-term storage of the resulting finely dispersed powders under normal conditions. X-ray diffraction and high-resolution transmission electron microscopy were used to study the resulting powder products of plasma-chemical synthesis, and density measurements were conducted. Additionally, to define the average particle size more accurately, the specific surface was measured using the BET method. The instrumental research revealed the presence of ultra- and nanodispersed particles with a core-shell structure in the powder products. These particles included titanium carbide-nitride compounds as a refractory core and metallic nickel as a metallic shell. In addition, the presence of complex titanium-nickel nitride $\text{Ti}_{0.7}\text{Ni}_{0.3}\text{N}$ was recorded. According to direct measurements, the average particle size of the nanocrystalline fraction is 18.9 ± 0.2 nm. The obtained research results enabled us to develop a chemical model of crystallization of TiC_xN_y -Ni core-shell structures, which is implemented in a hardening chamber at a crystallization rate of 10^5 °C/s. To fabricate the model, we used the reference data on the boiling and crystallization temperatures of the elements and compounds being a part of highly dispersed compositions and recorded by X-ray diffraction, as well as the $\Delta G(t)$ dependences for TiC and TiN.

Keywords: titanium nickelide, titanium carbide, plasma-chemical synthesis, low-temperature plasma, X-ray phase analysis, high-resolution transmission electron microscopy

Acknowledgements: The work was carried out in accordance with the state assignment for the Institute of Solid State Chemistry of the Ural Branch of the Russian Academy of Sciences (theme No. 24020600024-5).

For citation: Avdeeva Yu.A., Luzhkova I.V., Murzakaev A.M., Ermakov A.N. Plasma-chemical synthesis of highly dispersed core-shell structures from a mechanical mixture of titanium carbide and titanium nickelide. *Powder Metallurgy and Functional Coatings*. 2024;18(3):5–15. <https://doi.org/10.17073/1997-308X-2024-3-5-15>

Плазмохимический синтез высокодисперсных структур «ядро–оболочка» из механической смеси карбида титана с никелидом титана

Ю. А. Авдеева¹, И. В. Лужкова¹, А. М. Мурзакаев², А. Н. Ермаков¹

¹ Институт химии твердого тела УрО РАН

Россия, 620990, Свердловская обл., г. Екатеринбург, ул. Первомайская, 91

² Институт электрофизики УрО РАН

Россия, 620216, Свердловская обл., г. Екатеринбург, ул. Амундсена, 106

✉ y-avdeeva@list.ru

Аннотация. Проведены исследования, направленные на формирование ультрадисперсных и нанокристаллических структур «ядро–оболочка» на основе тугоплавких соединений титана с никелем в ходе плазмохимического синтеза механической смеси TiC и TiNi в низкотемпературной азотной плазме. Охлаждение происходило в интенсивно закрученном потоке газообразного азота в закалочной камере. Продукты переработки сепарировались в условиях циклона вихревого типа и тканевого фильтра рукавного типа. После переработки продукты подвергались капсулированию, направленному на понижение пиррофорности для длительного хранения полученных высокодисперсных порошков в нормальных условиях. Переработанные порошковые продукты плазмохимического синтеза исследовались методами рентгенографии, просвечивающей электронной микроскопии высокого разрешения и измерения плотности. Дополнительно, для уточнения среднего размера частиц, проводились измерения удельной поверхности по методике BET. Результаты аппаратных исследований показали наличие ультра- и нанодисперсных частиц со структурой «ядро–оболочка» в порошковых продуктах. Эти частицы включали карбидно-нитридные соединения титана в качестве тугоплавкого ядра и металлический никель в виде металлической оболочки. Дополнительно зафиксировано присутствие сложного титан-никелевого нитрида $Ti_{0.7}Ni_{0.3}N$. Нанокристаллическая фракция по результатам прямых измерений характеризуется средним размером частиц $18,9 \pm 0,2$ нм. На основе полученных результатов исследований была сформирована химическая модель кристаллизации структур «ядро–оболочка» TiC_xN_y-Ni , реализуемая в условиях закалочной камеры со скоростью кристаллизации 10^5 °C/с. Для составления модели использовались справочные данные о температурах кипения и кристаллизации элементов и соединений, входящих в состав высокодисперсных композиций и зафиксированных рентгенографически, а также зависимости $\Delta G(t)$ для TiC и TiNi.

Ключевые слова: никелид титана, карбид титана, плазмохимический синтез, низкотемпературная плазма, рентгенофазовый анализ, просвечивающая электронная микроскопия высокого разрешения

Благодарности: Работа выполнена в соответствии с государственным заданием Института химии твердого тела УрО РАН (тема № 124020600024-5).

Для цитирования: Авдеева Ю.А., Лужкова И.В., Мурзакаев А.М., Ермаков А.Н. Плазмохимический синтез высокодисперсных структур «ядро–оболочка» из механической смеси карбида титана с никелидом титана. *Известия вузов. Порошковая металлургия и функциональные покрытия*. 2024;18(3):5–15. <https://doi.org/10.17073/1997-308X-2024-3-5-15>

Introduction

At present, the nanocrystalline state of matter is extensively investigated [1–5] as it has a number of unique physicochemical and physicomechanical properties determined by the high dispersion of particles. For example, the most productive methods for the formation of nanocrystalline materials include plasma-chemical synthesis in a low-temperature gas plasma [6]. From the standpoint of fundamental research [7], “quasi-equilibrium” processes occurring during plasma-chemical synthesis in a low-temperature gas plasma enable one to use the laws of equilibrium thermodynamics to calculate the final state of the reacting system.

The formation of core–shell structures of a given composition during synthesis of ultra- and nanodisperse

materials based on refractory compounds of IV–VIA subgroups of the periodic table, with the participation of metals such as Ni and Co, makes it possible to synthesize composite powder products suitable for direct use. One of the technological examples is the use of nanomaterials, obtained during plasma-chemical synthesis in a low-temperature nitrogen plasma and based on refractory compounds of titanium, vanadium, zirconium and other elements of IV–VIA subgroups, as modifiers for casting steels and non-ferrous alloys, as described in [8–10]. During extra-furnace steel processing, nanocrystalline materials are placed into a ladle using different methods and are rather evenly distributed throughout the molten steel or non-ferrous alloy, acting as artificial nuclei during crystallization. The metal components of composite nanocrystalline

particles, therefore, serve as a buffer layer between the melt and the refractory core, protecting the latter from early solid-phase dissolution. The microquantities of such modifiers improve the physical and mechanical properties of cast materials while maintaining their specified chemical composition.

On the other hand, refractory compounds based on elements of IV–VIA subgroups of the periodic table, with high hardness values, are used as the basis for tool materials [11]. The binding phases are metals and their intermetallic compounds, which allow metal ceramic compositions to be formed, where the matrix in the form of grains of refractory compounds is impregnated with a metal melt during high-temperature sintering in vacuum with the participation of a liquid phase. The patterns of such processes for various powder compositions based on titanium carbonitride $\text{TiC}_{0.5}\text{N}_{0.5}$ were earlier described in [12–16].

The main objective of this paper is to study the patterns for the formation of ultradisperse and nanocrystalline particles with a core-shell structure during plasma-chemical synthesis of a mechanical mixture of TiC and TiNi (1:1) in a low-temperature nitrogen plasma.

Methods

Microcrystalline powders of titanium carbide (50 μm) and titanium nickelide (40 μm) were used as the initial components of the charge for plasma-chemical synthesis. The industrial plasma-chemical plant described in [6] was used for plasma-chemical synthesis. The plant productivity can reach 1 t/h, which confirms a quite reasonable cost of this technology.

The capacity of the plasma chemical plant (FSUE SRIOCCT, Saratov) was 25 kW, voltage – 200–220 V, current – 100–110 A, plasma flow speed – 55 m/s, gaseous nitrogen flow rate in the plasma reactor – 25–30 m^3/h (of which plasma formation accounted for 6 m^3/h and stabilization and hardening – 19–24 m^3/h). The initial mechanical mixture consumption was 200 g/h.

The pneumatic transport transferred the processed ultrafine and nanocrystalline powder into a vortex-type cyclone and a bag-type fabric filter for separation. Nitrogen was used as a transport gas. After cooling, air was slowly introduced into the separation units to form a thin passivating oxide film. At the next passivation stage, the materials were encapsulated in a specialized unit of a plasma-chemical plant (capsulator), which ensures long-term storage of highly dispersed materials under normal conditions. The technique of plasma-chemical synthesis in a low-temperature nitrogen plasma based on the plasma recondensation scheme is described in more detail in [6].

The core-shell structures processed in the form of ultrafine and nanocrystalline powders were studied by X-ray diffraction (SHIMADZU XRD 7000 X-ray diffractometer, CuK_α -cathode, Japan) and high-resolution transmission electron microscopy (HR TEM) (JEOL JEM 2100 transmission electron microscope, Japan). The X-ray investigation results were processed using the WinXPOW software (ICDD database) to determine the phase composition of the resulting core-shell structures. The crystallographic parameters of the phase components were specified in the PowderCell 2.3 software package using the ICSD file located on the Springer Materials e-platform. The electron microscope images were processed to measure particle sizes in Mesurer software and then in standard mathematical editors to construct distribution histograms and determine the average particle size. High-resolution images were processed in the DigitalMicrograph 7.0 software. The results of interplanar spacing measurements were compared with the ICDD database file to specify the phase composition and determine the local states of additionally detected phases.

The density of the final synthesis products was assessed using a helium pycnometer (AccuPyc II 1340 V1.09, Micromeritics, USA). The specific surface area was measured on a specific surface area analyzer (Gemini VII 2390 V1.03 (V1.03 t), USA) using the BET method. The average particle size was determined for each of the processed fractions based on the values of density and specific surface area [17].

Results and discussion

The results of X-ray investigations of fractions of core-shell structures obtained during plasma-chemical synthesis in a low-temperature nitrogen plasma of a mechanical mixture of TiC and TiNi are presented in Fig. 1 and in the table. The refractory phase in both fractions of dispersed materials is represented by cubic compounds.

While specifying the unit cell parameters, we revealed that during crystallization in a quenching chamber at a rate of 10^5 $^\circ\text{C}/\text{s}$, oxycarbide and carbonitride phases of various compositions are formed in each fraction, as indicated in the table. The carbonitride composition is formed with a predominant amount of nitrogen in the non-metallic sublattice.

According to X-ray diffraction results, the cubic Ni phase ($Fm-3m$ space group) is observed only in the fabric filter fraction, where its amount is determined to be 5 wt. % (see the Table). At the same time, the X-ray diffraction pattern of the powder composi-

tion from the filter contains complex titanium-nickel nitride $\text{Ti}_{0.7}\text{Ni}_{0.3}\text{N}$ in the amount of 5 wt. %. According to the X-ray diffraction patterns (see Fig. 1), titanium-nickel nitride $\text{Ti}_{0.7}\text{Ni}_{0.3}\text{N}$, the visualization of which was presented in [18], is in a highly deformed state causing changes in intensities [19]. The resulting preferential orientation of the crystal lattice, in accordance

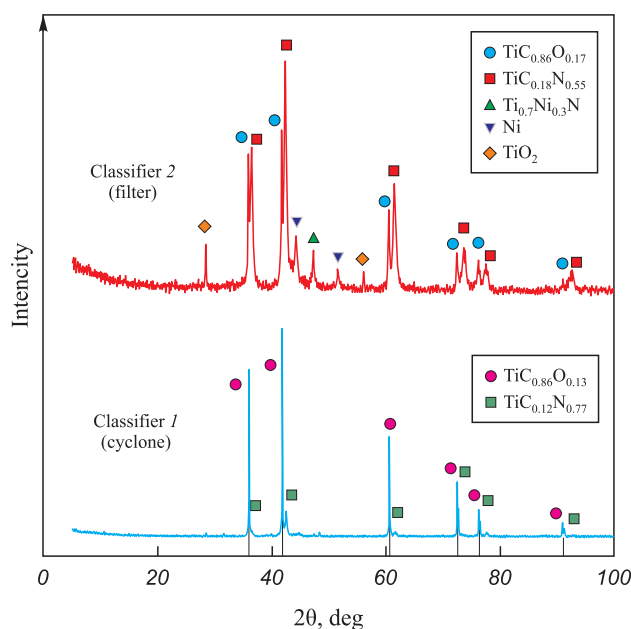


Fig. 1. X-ray diffraction patterns of highly dispersed fractions obtained from a mechanical mixture of TiC and TiNi (1:1) during plasma-chemical synthesis in a low-temperature nitrogen plasma

Рис. 1. Рентгенограммы высокодисперсных фракций, полученных из механической смеси TiC–TiNi (1:1) в процессе плазмохимического синтеза в низкотемпературной азотной плазме

with [20], can be ensured by the high rate of crystallization of the obtained powders. The issues related to formation and identification of $\text{Ti}_{0.7}\text{Ni}_{0.3}\text{N}$ using the example of the TiN–Ni core–shell structure, studied within the framework of high-resolution transmission electron microscopy, are discussed in [21]. The rutile modification of TiO_2 is formed in the course of forced acidification by slow inflow of air into classifiers 1 and 2, its share being 2 wt. %.

The measurements of pycnometric density and specific surface area by the BET method, presented in the table, revealed that the core–shell structures formed differ in density values. This effect can be attributed to the quantitative content of the processed compositions.

Visualization of the core–shell structure using the example of a nanocrystalline fraction from classifier 2 – a bag-type fabric filter – was confirmed by high-resolution transmission electron microscopy (Fig. 2).

Figure 2, *a, b* shows the general picture, which demonstrates that the fraction from the filter is really nanodispersed, since the average particle size based on the results of 767 measurements is 18.9 ± 0.2 nm; the histogram of particle size distribution is shown in Fig. 2, *c*.

The presence of a core–shell structure is determined by the presence of high-contrast areas at the periphery of the grains, and the grains themselves have both a round and faceted shape, as shown in Fig. 3.

Figure 3 shows the results of fixation of metallic nickel (plot 1) and titanium carbide TiC (plot 2). According to the results of measurements of interplanar spacing in plot 1, cubic metallic Ni (*Fm-3m*

Phase composition, density (ρ), specific surface area (S_{sp}) and the calculated value of the average size of the resulting particles (d_{avg}) from the mechanical mixture of TiC and TiNi (1:1) after plasma-chemical synthesis in a low-temperature nitrogen plasma

Фазовый состав, плотность (ρ), удельная поверхность ($S_{уд}$) и расчетное значение среднего размера полученных частиц ($d_{ср}$) из механической смеси TiC–TiNi (1:1) после плазмохимического синтеза в низкотемпературной азотной плазме

Fraction	Phase composition	Space group	Phase fraction, wt. %	Lattice parameter, nm	ρ , g/cm ³	S_{sp} , m ² /g	d_{avg} , μm
Classifier 1 (cyclone)	$\text{TiC}_{0.86}\text{O}_{0.13}$	<i>Fm-3m</i>	86	$a = 0.43162$	5.99	5.27	0.19
	$\text{TiC}_{0.12}\text{N}_{0.77}$	<i>Fm-3m</i>	14	$a = 0.42496$			
Classifier 2 (filter)	TiC	<i>Fm-3m</i>	44	$a = 0.43222$	5.66	106.00	0.01
	$\text{TiC}_{0.18}\text{N}_{0.55}$	<i>Fm-3m</i>	44	$a = 0.42606$			
	Ni	<i>Fm-3m</i>	5	$a = 0.35406$			
	TiO_2	<i>P42/mnm</i>	2	$a = 0.44860$			
				$c = 0.29859$			
	$\text{Ti}_{0.7}\text{Ni}_{0.3}\text{N}$	<i>P-6m2</i>	5	$a = 0.29735$			
				$c = 0.28934$			

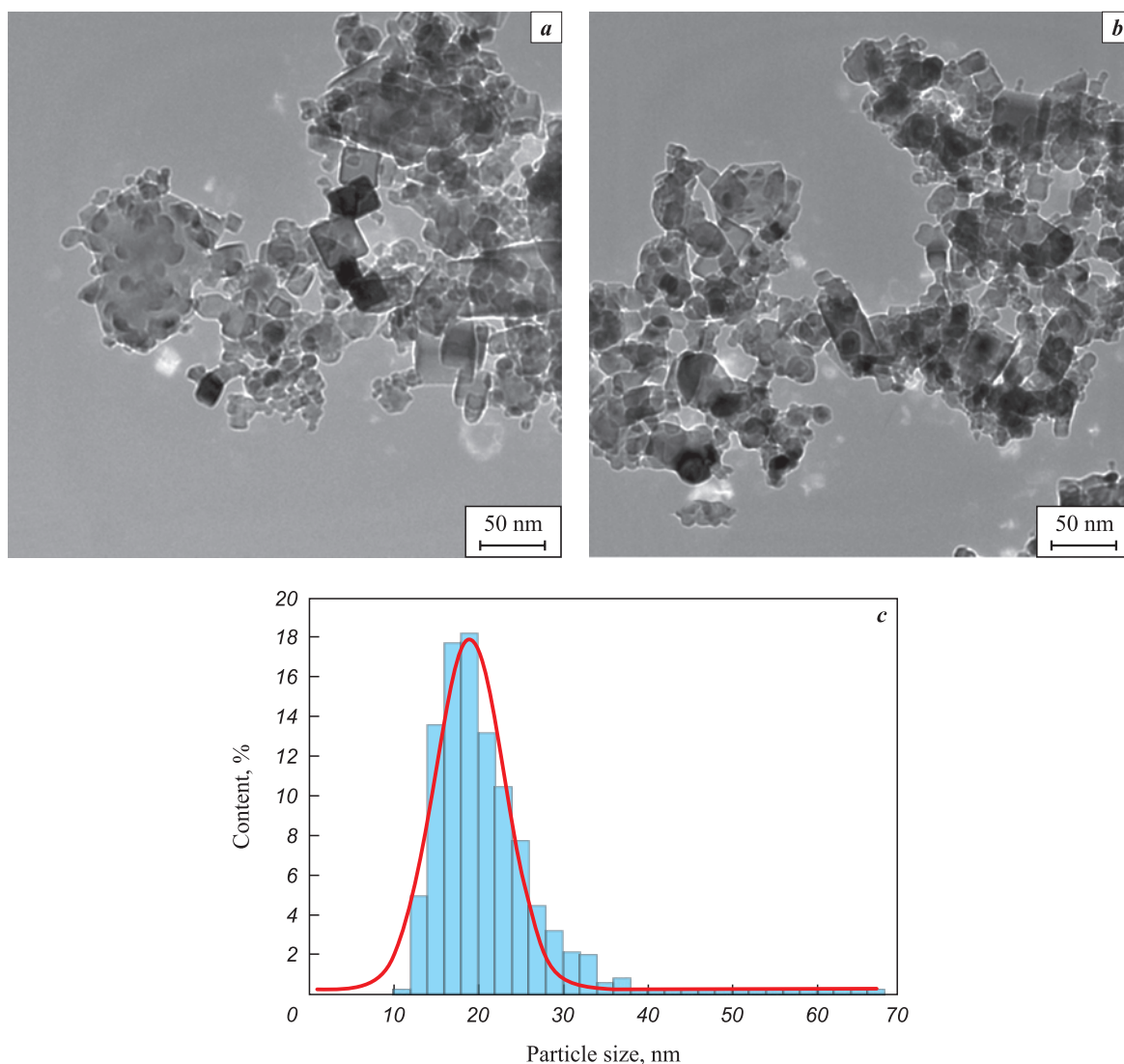


Fig. 2. HR TEM of a nanocrystalline powder with a core-shell structure obtained from a powder mechanical mixture of TiC and TiNi (1:1) during plasma-chemical synthesis in a low-temperature nitrogen plasma (*a, b*) and histogram of particle size distribution plotted based on direct measurements (*c*)

Рис. 2. ПЭМ ВР нанокристаллического порошка со структурой «ядро-оболочка», полученного из порошковой механической смеси TiC–TiNi (1:1) в ходе плазмохимического синтеза в низкотемпературной азотной плазме (*a, b*), и гистограмма распределения размеров частиц, построенная на основе прямых измерений (*c*)

space group) is characterized by interplanar spacings $d_{200} = 0.1797$ nm, $d_{111} = 0.2054$ nm, and $d_{-111} = 0.2087$ nm. In plot 2, the identified planes belong to TiC ($Fm-3m$ space group), $d_{111} = 0.2533$ nm.

The hexagonal Ni is present in the form of a (002) plane with interplanar spacing $d_{002} = 0.2189$ nm in the section of the electron microscope image shown in Fig. 4.

The presence of titanium-nickel nitride $Ti_{0.7}Ni_{0.3}N$ of the hexagonal modification ($P-6m2$ space group, $d_{100} = 0.2543$ nm) along with hexagonal Ni (space group $P6_3/mmc$, $d_{100} = 0.2250$ nm) and cubic TiC ($Fm-3m$ space group, $d_{111} = 0.2568$ nm) is shown in Fig. 5.

Based on the TEM studies, Fig. 6 shows an example of the presence of faceted particles of cubic titanium carbide TiC – the composition of the presented faceted particle is interpreted by the (200) TiC plane ($Fm-3m$ space group), $d_{200} = 0.2150$ nm.

Summarizing the findings of X-ray diffraction and high-resolution transmission electron microscopy, we can formulate a chemical model of the core-shell structures formed during plasma-chemical synthesis in a low-temperature nitrogen plasma followed by crystallization in an intensely swirling nitrogen flow (Fig. 7). The model is based on the physicochemical properties of all interpreted phase components, which include boiling, condensation and crystallization tem-

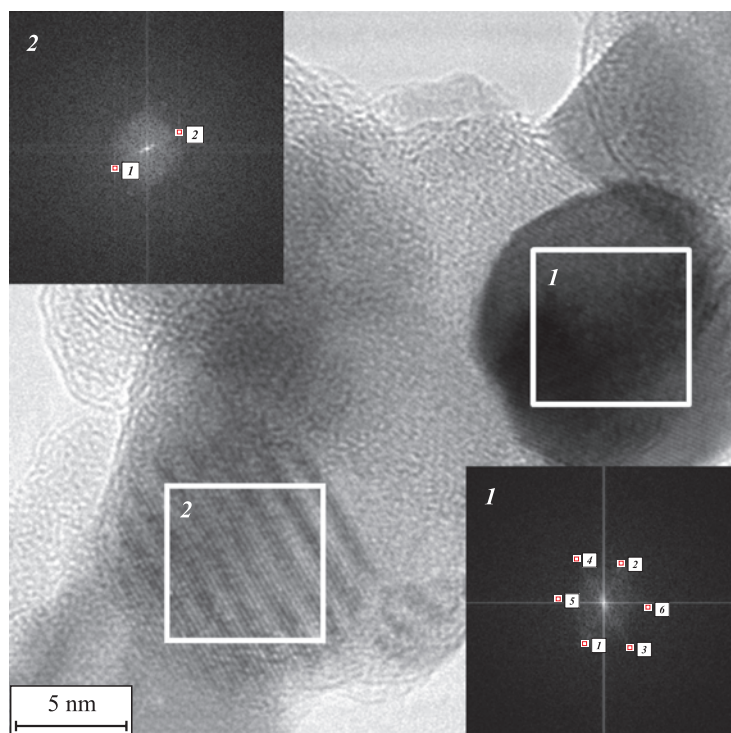


Fig. 3. HR TEM of nanocrystalline powder particles with a core–shell structure obtained from a powder mechanical mixture of TiC and TiNi (1:1) during plasma-chemical synthesis in a low-temperature nitrogen plasma, taking into account the presence of metallic Ni (plot 1) and titanium carbide TiC (plot 2)

Рис. 3. ПЭМ ВР нанокристаллических частиц порошка со структурой «ядро–оболочка», полученного из порошковой механической смеси TiC–TiNi (1:1) в ходе плазмохимического синтеза в низкотемпературной азотной плазме, с учетом присутствия металлического Ni (участок 1) и карбида титана TiC (участок 2)

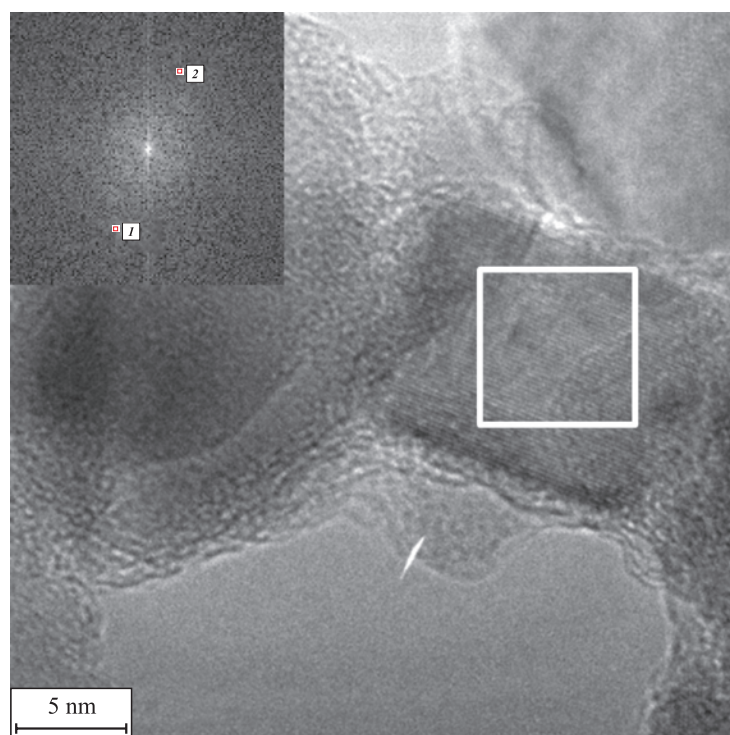


Fig. 4. Localized state of hexagonal metallic Ni according to the results of HR TEM and fast Fourier transform

Рис. 4. Локализованное состояние металлического Ni гексагональной модификации по результатам ПЭМ ВР и быстрого преобразования Фурье

peratures [22; 23], as well as functional dependences $\Delta G(t)$ under equilibrium conditions [24]. Additionally, information on the wettability of refractory com-

pounds [22] by molten nickel metal was utilized to justify the metallic shell on the periphery of nanocrystalline refractory particles.

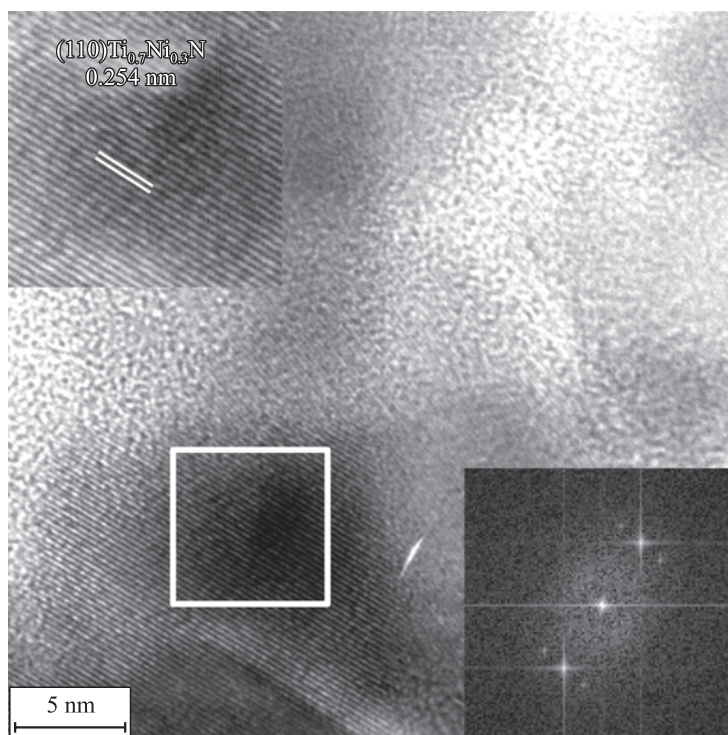


Fig. 5. Localized state of $\text{Ti}_{0.7}\text{Ni}_{0.3}\text{N}$ ($P-6m2$ space group) according to the results of HR TEM

Рис. 5. Локализованное состояние $\text{Ti}_{0.7}\text{Ni}_{0.3}\text{N}$ (пр. гр. $P-6m2$) по результатам ПЭМ ВР

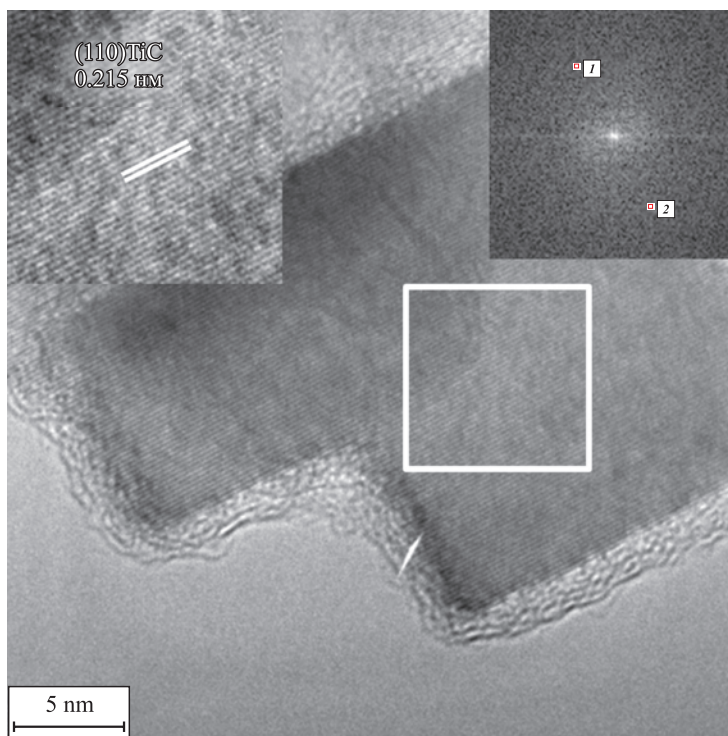


Fig. 6. Faceted nanocrystalline TiC particle coated with an amorphous layer of metallic nickel

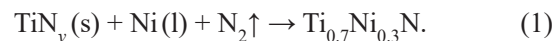
Рис. 6. Ограниченная нанокристаллическая частица TiC, покрытая аморфным слоем металлического никеля

Within the framework of this model, the flow of low-temperature plasma with a mechanical mixture of TiC and TiNi is separated by temperature barriers as it enters the quenching chamber filled with nitrogen. The boiling or crystallization temperatures of all phase components determined by *X*-ray diffraction are selected as temperature barriers.

Keeping in mind that low-temperature plasma can exist only in the temperature range of 4000–6000 °C, the first temperature barrier responsible for the crystallization of the refractory components of the emerging core-shell structures can be identified as the transition of titanium carbide from a gaseous state to a solid state described in [25–28], its temperature is 4300 °C [23]. Considering the significant excess of gaseous nitrogen in the entire volume of the quenching chamber, it can be stated that under these conditions it interacts with solid-phase TiC with the subsequent formation of carbonitride TiC_xN_z (see the Table). The functional dependences $\Delta G(t)$ for these processes [24] and the data on phase formation in the Ti–C–N system [29] confirm that mutual solid solutions with wide homogeneity regions can be formed. At the same time, during the crystallization of refractory components in the quenching chamber, TiNy titanium nitride nanoparticles, isomorphic to Ti–C–N compounds, can be formed on the surface.

Separately, it should be mentioned that passing the temperature range of 4300–3930 °C nickel remains in a gaseous state up to the temperature of 2730 °C [30], at which it passes from a gaseous to a liquid state and which is the second temperature barrier. Passing the boiling point, liquid nickel actively

interacts with refractory grains. Under these conditions, titanium-nickel nitride $\text{Ti}_{0.7}\text{Ni}_{0.3}\text{N}$ is formed [21] according to the theory of heterogeneous nucleation by B. Chalmers [31], some provisions of which are given in [8] by the reaction equation



It should be noted that the complex nitride $\text{Ti}_{0.7}\text{Ni}_{0.3}\text{N}$ and its analogue $\text{Ti}_{0.7}\text{Co}_{0.3}\text{N}$ were earlier detected by *X*-ray diffraction and transmission electron microscopy and described in [21; 32–34].

Reaction (1) occurs in the temperature range from 1600 °C [18] to 1455 °C, which corresponds to the crystallization temperature of metallic nickel and constitutes the third temperature barrier in the presented model. As nickel crystallizes, no chemical interactions occur in the formed core-shell structures, and all the resulting compositions can only cool down at this stage. Next, the mixture of processed fractions is transported to classifiers 1 and 2 for separation.

Conclusion

As a result of plasma-chemical synthesis in a low-temperature nitrogen plasma, we obtained ultrafine and nanocrystalline fractions of particles with a core-shell structure from a mechanical mixture of titanium carbide TiC and titanium nickelide TiNi in the ratio of 1:1.

All the resulting powder compositions were studied by *X*-ray diffraction and helium pycnometry. The specific surface area was determined using the BET method. The nanocrystal-

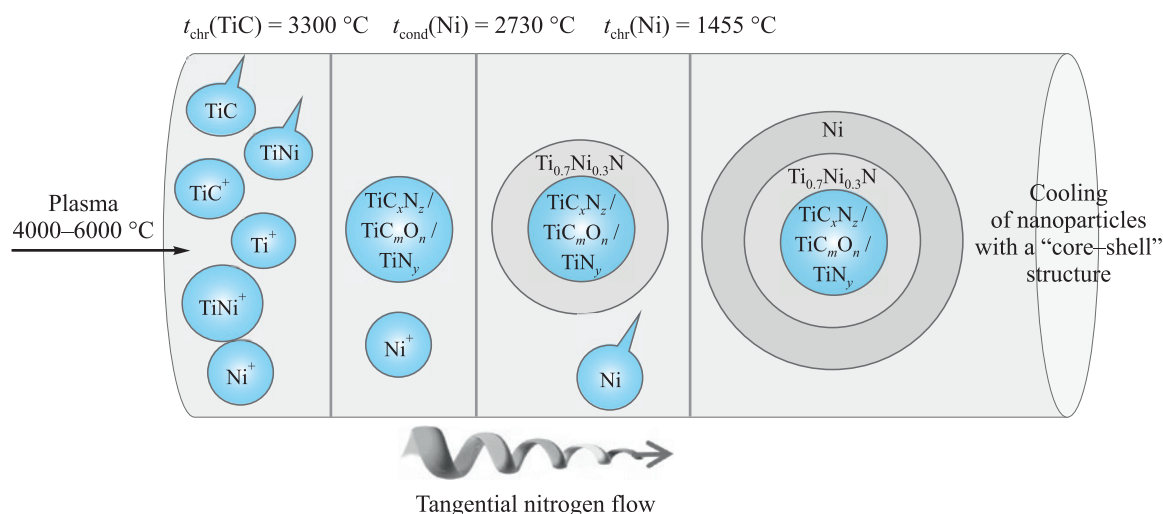


Fig. 7. Chemical mechanism of formation of a core-shell structure during plasma-chemical synthesis of the powder mixture of TiC and TiNi (1:1) in a low-temperature nitrogen plasma

Рис. 7. Химический механизм формирования структуры «ядро-оболочка» в ходе плазмохимического синтеза порошковой смеси TiC–TiNi (1:1) в низкотемпературной азотной плазме

line fraction was thoroughly investigated using high-resolution transmission electron microscopy.

Based on the research findings, the following conclusions can be drawn:

1. The ultra- and nanodispersed compositions formed during plasma-chemical synthesis have a core-shell structure. According to *X*-ray phase analysis confirmed by the results of high-resolution transmission electron microscopy, the refractory core is the $\text{TiC}/\text{TiC}_x\text{N}_y/\text{TiC}_x\text{O}_z$ compound coated with a metallic Ni shell; the complex titanium-nickel nitride $\text{Ti}_{0.7}\text{Ni}_{0.3}\text{N}$ acts as an interphase layer.

2. Based on *X*-ray diffraction and transmission electron microscopy data, taking into account the physico-chemical features of the detected phase components, we formulated the chemical mechanism for the formation of ultradisperse and nanocrystalline particles with a core-shell structure under crystallization conditions at a rate of 10^5 °C/s in a tangential nitrogen flow in a quenching chamber of the plasmatron.

3. The chemical mechanism of the formation of nanocrystalline particles is the overcoming of temperature barriers by the plasma flow, with elements evaporated in it that are a part of the charge. The crystallization temperatures of phase components that are present, according to *X*-ray diffraction, in ultradisperse and nanocrystalline particles act as temperature barriers.

References / Список литературы

1. Song M., Yang Y., Xiang M., Zhu Q., Zhao H. Synthesis of nano-sized TiC powders by designing chemical vapor deposition system in a fluidized bed reactor. *Powder Technology*. 2021;380:256–264. <https://doi.org/10.1016/j.powtec.2020.11.045>
2. Dorosheva I.B., Vokhmintsev A.S., Weinstein I.A., Rempel A.A. Induced surface photovoltage in TiO_2 sol-gel nanoparticles. *Nanosystems: Physics, Chemistry, Mathematics*. 2023;14(4):447–453. <https://doi.org/10.17586/2220-8054-2023-14-4-447-453>
3. Kozlova T.O., Popov A.L., Romanov M.V., Savintseva I.V., Vasilyeva D.N., Baranchikov A.E., Ivanov V.K. Ceric phosphates and nanocrystalline ceria: selective toxicity to melanoma cells. *Nanosystems: Physics, Chemistry, Mathematics*. 2023;14(2):223–230. <https://doi.org/10.17586/2220-8054-2023-14-2-223-230>
4. Balestrat M., Cheype M., Gervais C., Deschanel X., Bernard S. Advanced nanocomposite materials made of TiC nanocrystals in situ immobilized in SiC foams with boosted spectral selectivity. *Materials Advances*. 2023;(4):1161–1170. <https://doi.org/10.1039/D2MA00886F>
5. Kapusta K., Drygas M., Janik J.F., Olejniczak Z. New synthesis route to kesterite $\text{Cu}_2\text{ZnSnS}_4$ semiconductor nanocrystalline powders utilizing copper alloys and a high energy ball milling-assisted process. *Journal of Materials Research and Technology*. 2020;9(6):13320–13331. <https://doi.org/10.1016/j.jmrt.2020.09.062>
6. Storozhenko P.A., Guseinov Sh.L., Malashin S.I. Nano-dispersed powders: Synthesis methods and practical applications. *Nanotechnologies in Russia*. 2009;4:262–274. <https://doi.org/10.1134/S1995078009050024>
 Стороженко П.А., Гусейнов Ш.Л., Малашин С.И. Нанодисперсные порошки: Методы получения и способы практического применения. *Российские нанотехнологии*. 2009;4(1–2):27–39. <https://doi.org/10.1134/S1995078009050024>
7. Tsvetkov Yu.V. Plasma metallurgy: current state, problems and prospects. *Pure and Applied Chemistry*. 1999;71(10):1853–1862. <https://doi.org/10.1351/pac199971101853>
8. Zhukov M.F., Cherskiy I.N., Cherepanov A.N., Konovarov N.A., Saburov V.P., Pavlenko N.A., Galevskiy G.V., Andrianova O.A., Krushenko G.G. Hardening of metallic polymeric and elastomer materials by ultrafine powders of plasma-chemical synthesis. Novosibirsk: Nauka, 1999. 307 p. (In Russ.).
 Жуков М.Ф., Черский И.Н., Черепанов А.Н., Коновалов Н.А., Сабуров В.П., Павленко Н.А., Галевский Г.В., Андрианова О.А., Крушенко Г.Г. Упрочнение металлических полимерных и эластомерных материалов ультрадисперсными порошками плазмохимического синтеза. Новосибирск: Наука, 1999. 307 с.
9. Ermakov A.N., Luzhkova I.V., Avdeeva Yu.A., Dyakov A.A., Maurin N.I. Steel modification method: Patent 2781940 (RF). 2022. (In Russ.).
 Ермаков А.Н., Лужкова И.В., Авдеева Ю.А., Дьяков А.А., Маурин Н.И. Способ модифицирования стали: Патент 2781940 (РФ). 2022.
10. Ermakov A.N., Luzhkova I.V., Avdeeva Yu.A. Steel modification method: Patent 2781935 (RF). 2022. (In Russ.).
 Ермаков А.Н., Лужкова И.В., Авдеева Ю.А. Способ модифицирования стали: Пат. 2781935 (РФ). 2022.
11. Pastor H. Titanium-carbonitride-based hard alloys for cutting tools. *Materials Science and Engineering: A*. 1988;105–106:401–409. [https://doi.org/10.1016/0025-5416\(88\)90724-0](https://doi.org/10.1016/0025-5416(88)90724-0)
12. Askarova L.Kh., Grigorov I.G., Zainulin Yu.G. Liquid-phase interaction in the $\text{TiC}_{0.5}\text{N}_{0.5}$ -TiNi-Ti system. *Metal-ly*. 1998;(2):20–24. (In Russ.).
 Аскарова Л.Х., Григоров И.Г., Зайнулин Ю.Г. Жидкофазное взаимодействие в системе $\text{TiC}_{0.5}\text{N}_{0.5}$ -TiNi-Ti. *Металлы*. 1998;2:20–24.
13. Askarova L.Kh., Shchipachev E.V., Ermakov A.N., Grigorov I.G., Zainulin Yu.G. Influence of vanadium and niobium on the phase composition of cermets based on carbide-titanium nitride with a titanium-nickel bond. *Neorganicheskie Materialy*. 2001;37(2):207–210. (In Russ.).
 Аскарова Л.Х., Щипачев Е.В., Ермаков А.Н., Григоров И.Г., Зайнулин Ю.Г. Влияние ванадия и ниобия на фазовый состав керметов на основе карбида – нитрида титана с титан-никелевой связкой. *Неорганические материалы*. 2001;37(2):207–210.
14. Askarova L.Kh., Grigorov I.G., Fedorenko V.V., Zainulin Yu.G. Liquid-phase interaction in $\text{TiC}_{0.5}\text{N}_{0.5}$ -TiNi-Ti-Zr

- and $\text{TiC}_{0.5}\text{N}_{0.5}$ -TiNi-Ti-Zr alloys. *Metally*. 1998;(5):16–19. (In Russ.).
- Аскарова Л.Х., Григоров И.Г., Федоренко В.В., Зайнулин Ю.Г. Жидкофазное взаимодействие в сплавах $\text{TiC}_{0.5}\text{N}_{0.5}$ -TiNi-Ti-Zr и $\text{TiC}_{0.5}\text{N}_{0.5}$ -TiNi-Ti-Zr. *Металлы*. 1998;(5):16–19.
15. Askarova L.Kh., Grigorov I.G., Zainulin Yu.G. Liquid-phase interaction in $\text{TiC}_{0.5}\text{N}_{0.5}$ -TiNi-Mo and $\text{TiC}_{0.5}\text{N}_{0.5}$ -TiNi-Ti-Mo alloys. *Metally*. 1998;(6):24–27. (In Russ.).
 Аскарова Л.Х., Григоров И.Г., Зайнулин Ю.Г. Жидкофазное взаимодействие в сплавах $\text{TiC}_{0.5}\text{N}_{0.5}$ -TiNi-Mo и $\text{TiC}_{0.5}\text{N}_{0.5}$ -TiNi-Ti-Mo. *Металлы*. 1998;(6):24–27.
 16. Askarova L.Kh., Grigorov I.G., Zainulin Yu.G. Features of phase and structure formation during liquid-phase sintering of $\text{TiC}_{0.5}\text{N}_{0.5}$ -TiNi-Nb and $\text{TiC}_{0.5}\text{N}_{0.5}$ -TiNi-Ti-Nb alloys. *Metally*. 2000;(1):130–133. (In Russ.).
 Аскарова Л.Х., Григоров И.Г., Зайнулин Ю.Г. Особенности фазо- и структурообразования при жидкофазном спекании сплавов $\text{TiC}_{0.5}\text{N}_{0.5}$ -TiNi-Nb и $\text{TiC}_{0.5}\text{N}_{0.5}$ -TiNi-Ti-Nb. *Металлы*. 2000;(1):130–133.
 17. Sadovnikov S.I., Gusev A.I. Effect of particle size and specific surface area on the determination of the density of nanocrystalline silver sulfide Ag_2S powders. *Physics of the Solid State*. 2018;60:877–881.
<https://doi.org/10.1134/S106378341805027X>
 Садовников С.И., Гусев А.И. Влияние размера частиц и удельной поверхности на определение плотности нанокристаллических порошков сульфида серебра Ag_2S . *Физика твердого тела*. 2018;60(5):875–879.
<https://doi.org/10.21883/FTT.2018.05.45780.313>
 18. Bhaskar U.K., Pradhan S.K. Microstructural evolution of nanostructured $\text{Ti}_{0.7}\text{Ni}_{0.3}\text{N}$ prepared by reactive ball-milling. *Materials Research Bulletin*. 2013;48:3129–3135.
<https://doi.org/10.1016/j.materresbull.2013.04.061>
 19. Bunaciu A.A., Udriștioiu E.G., Aboul-Enein H.Y. X-ray diffraction: Instrumentation and applications. *Critical Reviews in Analytical Chemistry*. 2015;45(4):289–299.
<https://doi.org/10.1080/10408347.2014.949616>
 20. Fultz B., Howe J.M. Transmission electron microscopy and diffractometry of materials, 3rd ed. Berlin, Heidelberg: Springer, 2008. 758 p.
<https://doi.org/10.1007/978-3-540-73886-2>
 Фульц Б., Хау Дж.М. Просвечивающая электронная микроскопия и дифрактометрия материалов. М.: Техносфера, 2011. 904 с.
<https://doi.org/10.1007/978-3-540-73886-2>
 21. Ermakov A.N., Luzhkova I.V., Avdeeva Yu.A., Murzakaev A.M., Zainulin Yu.G., Dobrinsky E.K. Formation of complex titanium-nickel nitride $\text{Ti}_{0.7}\text{Ni}_{0.3}\text{N}$ in the “core-shell” structure of TiN-Ni. *International Journal of Refractory Metals and Hard Materials*. 2019;84:104996.
<https://doi.org/10.1016/j.ijrmhm.2019.104996>
 22. Mhadhbi M., Driss M. Titanium carbide: Synthesis, properties and applications. *Brilliant Engineering*. 2021;2:1–11.
<https://doi.org/10.36937/ben.2021.002.001>
 23. Banaszek K., Klimek L. Wettability and surface free energy of Ti(C,N) coatings on nickel-based casting prosthetic alloys. *Archives of Foundry Engineering*. 2015;15:11–16.
<https://doi.org/10.1515/afe-2015-0050>
 24. Barin I. Thermochemical data of pure substances. 3rd ed. Weinheim, New York, Basel, Cambridge, Tokyo: VCH, 1995. 2003 с.
 25. Gusev A.I., Rempel A.A. Nonstoichiometry, disorder and order in a solid. Ekaterinburg: NISO UrO RAN, 2001. 579 p. (In Russ.).
 Гусев А.И., Ремпель А.А. Нестехиометрия, беспорядок и порядок в твердом теле. Екатеринбург: НИСО УрО РАН, 2001. 579 с.
 26. Samokhin A.V., Polyakov S.N., Astashov A.G., Tsvetkov Yu.V. Simulation of the process of synthesis of nanopowders in a plasma reactor jet type. I. Statement of the problem and model validation. *Fizika i Khimiya Obrabotki Materialov*. 2013;(6):40–46. (In Russ.).
 Самохин А.В., Поляков С.Н., Асташов А.Г., Цветков Ю.В. Моделирование процесса синтеза нанопорошков в плазменном реакторе струйного типа. I. Постановка задачи и проверка модели. *Физика и химия обработки материалов*. 2013;(6):40–46.
 27. Samokhin A.V., Polyakov S.N., Astashov A.G., Tsvetkov Yu.V. Simulation of the process of nanopowder synthesis in a jet-type plasma reactor. II. Nanoparticles formation. *Inorganic Materials: Applied Research*. 2014;5(3):224–229. <https://doi.org/10.1134/S2075113314030149>
 Самохин А.В., Поляков С.Н., Асташов А.Г., Цветков Ю.В. Моделирование процесса синтеза нанопорошков в плазменном реакторе струйного типа. II. Формирование наночастиц. *Физика и химия обработки материалов*. 2014;(3):12–17.
<https://doi.org/10.1134/S2075113314030149>
 28. Shiryayeva L.S., Gorbuzova A.K., Galevsky G.V. Production and application of titanium carbide (assessment, trends, forecasts). *Nauchno-tekhnicheskie vedomosti Sankt-Peterburgskogo Gosudarstvennogo Universiteta*. 2014;2(195):100–107. (In Russ.).
 Ширяева Л.С., Горбузова А.К., Галевский Г.В. Производство и применение карбида титана (оценка, тенденции, прогнозы). *Научно-технические ведомости Санкт-Петербургского государственного политехнического университета*. 2014;2(195):100–107.
 29. Binder S., Lengauer W., Ettmayer P., Bauer J., Debuinge J., Bohn M. Phase equilibria in the systems Ti-C-N, Zr-C-N and Hf-C-N. *Journal of Alloys and Compounds*. 1995;217(1):128–136.
[https://doi.org/10.1016/0925-8388\(94\)01314-8](https://doi.org/10.1016/0925-8388(94)01314-8)
 30. Moghimi Z.A., Halali M., Nusheh M. An investigation on the temperature and stability behavior in the levitation melting of nickel. *Metallurgical and Materials Transactions B*. 2006;37B:997–1005.
<https://doi.org/10.1007/BF02735022>
 31. Filkov M., Kolesnikov A. Plasmachemical synthesis of nanopowders in the system Ti(O,C,N) for material structure modification. *Journal of Nanoscience*. 2016;2016:1361436. <https://doi.org/10.1155/2016/1361436>
 32. Avdeeva Yu.A., Luzhkova I.V., Ermakov A.N. Mechanism of formation of nanocrystalline particles with core-shell structure based on titanium oxynitrides with nickel

in the process of plasma-chemical synthesis of TiNi in a low-temperature nitrogen plasma. *Nanosystems: Physics, Chemistry, Mathematics*. 2022;13(2):212–219.

<https://doi.org/10.17586/2220-8054-2022-13-2-212-219>

33. Avdeeva Yu.A., Luzhkova I.V., Ermakov A.N. Formation of titanium-cobalt nitride $Ti_{0.7}Co_{0.3}N$ under plasma-chemical synthesis conditions in a low-temperature nitrogen plasma. *Nanosystems: Physics, Chemistry, Mathematics*. 2021;12(5):641–649.

<https://doi.org/10.17586/2220-8054-2021-12-5-641-649>

34. Avdeeva Yu.A., Luzhkova I.V., Ermakov A.N. Plasma-chemical synthesis of TiC–Mo–Co nanoparticles with a core-shell structure in a low-temperature nitrogen plasma. *Russian Metallurgy*. 2022;(9):1019–1026.


<https://doi.org/10.1134/s0036029522090038>

Авдеева Ю.А., Лужкова И.В., Ермаков А.Н. Плазмохимический синтез наночастиц TiC–Mo–Co со структурой «ядро–оболочка» в низкотемпературной азотной плазме. *Металлы*. 2022;(5):41–49.

<https://doi.org/10.1134/s0036029522090038>


Information about the Authors

Yuliya A. Avdeeva – Research Scientist at the Institute of Solid State Chemistry (ISSC) UB RAS

 **ORCID:** 0000-0002-1470-0476


 **E-mail:** y-avdeeva@list.ru

Irina V. Luzhkova – Research Scientist at the ISSC UB RAS

 **ORCID:** 0000-0001-9123-5371

 **E-mail:** key703@yandex.ru

Aidar M. Murzakaev – Cand. Sci. (Phys.-Math.), Senior Researcher at the Institute of Electrophysics UB RAS

 **ORCID:** 0000-0003-4440-427X

 **E-mail:** aidar@iep.uran.ru

Alexey N. Ermakov – Cand. Sci. (Chem.), Senior Researcher at the ISSC UB RAS

 **ORCID:** 0000-0002-2746-5292

 **E-mail:** ermakovihim@yandex.ru

Сведения об авторах

Юлия Александровна Авдеева – науч. сотрудник Института химии твердого тела (ИХТТ) УрО РАН

 **ORCID:** 0000-0002-1470-0476

 **E-mail:** y-avdeeva@list.ru

Ирина Викторовна Лужкова – науч. сотрудник ИХТТ УрО РАН

 **ORCID:** 0000-0001-9123-5371

 **E-mail:** key703@yandex.ru


Айдар Маркович Мурзакаев – к.ф.-м.н., ст. науч. сотрудник Института электрофизики УрО РАН

 **ORCID:** 0000-0003-4440-427X

 **E-mail:** aidar@iep.uran.ru

Алексей Николаевич Ермаков – к.х.н., ст. науч. сотрудник ИХТТ УрО РАН

 **ORCID:** 0000-0002-2746-5292

 **E-mail:** ermakovihim@yandex.ru

Contribution of the Authors

Yu. A. Avdeeva – processing the XRF and HR TEM results, participating in the discussion of the results.

I. V. Luzhkova – conducting experiments, participating in the discussion of the results.

A. M. Murzakaev – conducting HR TEM, processing the HR TEM results, participating in the discussion of the results.

A. N. Ermakov – determining the purpose of the work, conducting experiments, writing the article, participating in the discussion of the results.

Вклад авторов

Ю. А. Авдеева – обработка результатов РФА, ПЭМ ВР, участие в обсуждении результатов.

И. В. Лужкова – проведение экспериментов, участие в обсуждении результатов.

А. М. Мурзакаев – проведение ПЭМ ВР, обработка ПЭМ ВР, участие в обсуждении результатов.

А. Н. Ермаков – определение цели работы, проведение экспериментов, написание статьи, участие в обсуждении результатов.

Received 28.06.2023

Revised 16.11.2023

Accepted 20.11.2023

Статья поступила 28.06.2023 г.

Доработана 16.11.2023 г.

Принята к публикации 20.11.2023 г.



UDC 621.762.016


<https://doi.org/10.17073/1997-308X-2024-3-16-27>

Research article

Научная статья



Structure and properties of hot-forged powder steel-bronze bimetal with SiC additives

V. Yu. Dorofeyev¹ , E. N. Bessarabov¹, A. N. Sviridova¹,
I. V. Ivanova¹, L. I. Svistun², R. A. Vodolazhenko³

¹ Platov South-Russian State Polytechnic University (NPI)

132 Prosveshcheniya Str., Novocherkassk, Rostov Region 346428, Russia

² Kuban State Technological University

2 Moskovskaya Str., Krasnodar 350072, Russia

³ Synergy University

G Bld, 80 Leningradskiy Prosp., Moscow 129090, Russia

 dvyu56.56@mail.ru

Abstract. One of the main problems in the production of bimetals is associated with the difference in the physico-mechanical and structural properties of the materials being joined. Both solid-phase and liquid-phase methods are used to obtain bimetals. The main technological task is to create conditions for the formation of a transition zone between the working layer and adhesively bound substrate. We analyzed the known methods for producing compact and powder bimetals (insert molding, diffusion welding in the solid phase, infiltration, hot isostatic pressing, etc.). The bonding strength of bimetal layers is evaluated according to the results of mechanical shear or pull tests; however, such an assessment does not enable to determine if the product can be operated in the mode of frequent thermal cycles. The above method, which involves joint hot repressing of previously separately cold-pressed and sintered blanks of the working layer and substrates, is promising in terms of improving the mechanical and tribotechnical properties, reducing the risk of structural degradation of particles of hardening additives, as well as enhancing the quality of the connection of steel-bronze bimetal layers. In this case, the working layer is heated through heat transfer from the side of the substrate warmed up to a higher temperature. We studied the impact of technological conditions for obtaining hot-forged powder steel-bronze bimetal on the structure, features of thermal fatigue failure and tribological properties and presented the research results. For structural analysis, thermal fatigue and tribotechnical tests, the bimetal samples with vertical and horizontal arrangement of layers were obtained. The atomized iron powder PZhrV 3.200.28 was used as a base for fabricating the substrate from PK40 steel. Graphite powder GK-3 (GOST 4404-78) was used as a carbonaceous additive. The working layer was fabricated from BrO10 bronze powder obtained by atomizing. To improve the tribotechnical characteristics of the working layer, bronze powder was mixed with superfine grinding micropowder F1000 of black silicon carbide 53S. The quality of bonding of bimetal layers was assessed based on the thermal shock test results. Tribotechnical tests were carried out in the dry friction mode according to the “shaft–block” scheme. We proposed the technique for producing hot-forged powder bimetal “PK40 steel–BrO10 bronze”, which includes the following independent procedures: cold pressing of the substrate and working layer blanks, their sintering in a reducing environment, pre-deformation heating of the substrate and working layer at temperatures that ensure their satisfactory formability, assembly of heated substrate and working layer blanks in the mold and subsequent joint hot repressing. The resulting bimetal is characterized by increased values of thermal fatigue and wear resistance in comparison with the control samples manufactured using the traditional technology of hot repressing of the cold-pressed bimetallic blank.

Keywords: hot forging, porous blanks, powder bimetal, discontinuities, microcracks, thermal fatigue failure, structural powder steel, tin bronze, working layer, substrate, wear, friction coefficient, silicon carbide

Acknowledgements: Structural and elemental analysis using Quanta 200 i 3D scanning electron/microprobe analyzer was carried out at Nanotechnology, a resource sharing center operated by Platov South-Russian State Polytechnic University (NPI).

Forcitation: Dorofeyev V. Yu., Bessarabov E. N., Sviridova A. N., Ivanova I. V., Svistun L. I., Vodolazhenko R. A. Structure and properties of hot-forged powder steel-bronze bimetal with SiC additives. *Powder Metallurgy and Functional Coatings*. 2024;18(3):16–27. <https://doi.org/10.17073/1997-308X-2024-3-16-27>

Структура и свойства горячештампованного порошкового биметалла типа «сталь–бронза» с добавками SiC

В. Ю. Дорофеев¹, Е. Н. Бессарабов¹, А. Н. Свиридова¹,
И. В. Иванова¹, Л. И. Свистун², Р. А. Водолаженко³

¹ Южно-Российский государственный политехнический университет им. М.И. Платова (НПИ)

Россия, 346428, Ростовская обл., г. Новочеркасск, ул. Просвещения, 132

² Кубанский государственный технологический университет

Россия, 350072, г. Краснодар, ул. Московская, 2

³ Университет «Синергия»

Россия, 129090, г. Москва, Ленинградский пр-т, 80, корп. Г

✉ dvyu56.56@mail.ru

Аннотация. Одна из главных проблем при получении биметаллов (БМ) связана с различием физико-механических и структурных характеристик соединяемых материалов. При получении БМ нашли применение как твердофазные, так и жидкофазные методы. Основная задача технологии заключается в необходимости создания условий формирования переходной зоны между рабочим слоем и подложкой, имеющей с ними адгезионные связи. Приведен анализ известных способов получения компактных и порошковых биметаллов (заливка, диффузионная сварка в твердой фазе, инфильтрация, горячее изостатическое прессование и др.). Оценка прочности связи слоев БМ зачастую проводится по результатам механических испытаний на срез или отрыв, однако такая оценка не обеспечивает возможность анализа осуществимости эксплуатации изделия в режиме частых теплосмен. Перспективным в плане повышения показателей механических и триботехнических свойств, снижения риска структурной деградации частиц упрочняющих добавок, а также улучшения характеристик качества соединения слоев биметаллов «сталь–бронза» является использование ранее предложенного способа, заключающегося в совместной горячей допрессовке предварительно отдельно холоднопрессованных и спеченных заготовок рабочего слоя и подложки. При этом разогрев рабочего слоя осуществляется за счет передачи тепла со стороны подложки, нагретой до более высокой температуры. Представлены результаты исследования влияния технологических условий получения горячештампованного порошкового биметалла «сталь–бронза» на структуру, особенности термоусталостного разрушения и трибологические свойства. Для проведения структурного анализа, термоусталостных и триботехнических испытаний получали образцы БМ с вертикальным и горизонтальным расположением слоев. При получении подложки из стали ПК40 в качестве основы применяли распыленный железный порошок ПЖРВ 3.200.28. Углеродсодержащей добавкой служил порошок графита ГК-3 (ГОСТ 4404-78). Рабочий слой изготавливали из порошка бронзы БрО10, полученного методом распыления. Для повышения триботехнических характеристик рабочего слоя порошок бронзы смешивали с измельченным шлифовальным микропорошком F1000 карбида кремния черного 53С. Оценка качества соединения слоев БМ проводили по результатам испытаний на термоудар. Триботехнические испытания проводили в режиме сухого трения по схеме «вал–колодка». Предложена технология получения горячештампованного порошкового биметалла «сталь ПК40 – бронза БрО10», включающая самостоятельное выполнение операций холодного прессования заготовок подложки и рабочего слоя, их спекания в восстановительной среде, преддеформационного нагрева подложки и рабочего слоя при температурах, обеспечивающих удовлетворительную деформируемость подложки и рабочего слоя, сборки нагретых заготовок подложки и рабочего слоя в пресс-форме и последующей совместной горячей допрессовки. Полученный биметалл характеризуется повышенными значениями термо- и износостойкости в сравнении с образцами-свидетелями, изготовленными по традиционной технологии горячей допрессовки холоднопрессованной биметаллической заготовки.

Ключевые слова: горячая штамповка, пористые заготовки, порошковый биметалл, несплошности, микротрещины, термоусталостное разрушение, конструкционная порошковая сталь, оловянистая бронза, рабочий слой, основа, износ, коэффициент трения, карбид кремния

Благодарности: Структурный и элементный анализ на растровом микроскопе-микроанализаторе «Quanta 200 i 3D» проведен в Центре коллективного пользования «Нанотехнологии» ЮРГПУ (НПИ).

Для цитирования: Дорофеев В.Ю., Бессарабов Е.Н., Свиридова А.Н., Иванова И.В., Свистун Л.И., Водолаженко Р.А. Структура и свойства горячештампованного порошкового биметалла типа «сталь–бронза» с добавками SiC. *Известия вузов. Порошковая металлургия и функциональные покрытия*. 2024;18(3):16–27. <https://doi.org/10.17073/1997-308X-2024-3-16-27>

Introduction

The use of bimetals in industrial production enables to significantly reduce the specific quality of metal per structure and enhance their operating parameters and reliability [1]. The main problem with bimetals is that the materials to be joined have different physical, mechanical and structural properties (coefficients of thermal conductivity and linear expansion, crystal lattice parameters, structure of electronic shells, formability, melting temperatures, etc.). Both solid-phase and liquid-phase methods are used to obtain bimetals. The main technological task is to create conditions for the formation of a transition zone between the working layer and adhesively bound substrate.

The impact of the temperature of the bimetal production process on the transition zone thickness and the bonding strength of layers is not straightforward. When bimetals are obtained by insert molding, diffusion in the steel–copper boundary zone occurs at temperatures above 850 °C [2]. Plastic deformation of bimetal by 45–50 % helps to reduce the temperature of the diffusion onset to 700 °C. The size of the transition zone and the bonding strength of bimetal layers during diffusion welding in the solid phase is noticeably affected by the phase transformation in the steel substrate: Fe diffusion from AISI 1010 steel to copper at the transformation temperature of 845 °C is lower than at $t = 770$ °C due to the consumption of the internal energy for the phase transformation [3].

When solid phase diffusion welding is carried out to join tin bronzes and steels, no dendritic or zone liquations, or shrinkage interdendritic porosity, characteristic of bronzes of this class and associated with a wide temperature and concentration range of their solidification, are formed in the working layer [1]. Lowering of welding temperature prevents growth of liquation precipitates of tin in the joint zone, which reduces the probability of defect formation [4]. Thus produced joints are stable at short-time heating to 800–850 °C, which allows later to perform heat treatment of the steel substrate that forms part of bimetal to increase its strength properties.

The solid phase diffusion welding ($t = 680$ °C; $\tau = 1$ h) of lead bronze–steel bimetal ensures the formation of a diffusion layer with low microhardness at the interface, which helps to avoid possible brittle rupture in this zone [5]. On the contrary, when bronze–stainless steel bimetal is prepared by the method of vacuum casting ($t = 1160$ °C; $\tau = 1$ h), the interface transition layer formed has higher microhardness and elastic modulus than the matrix alloys. The fracture of this bimetal prefers to occur along the interface transition layer, and the fracture mode is cleavage

fracture [6]. The transition zone embrittlement is also caused by the diffusion of bronze atoms along the steel grain boundaries. The microstructure of grain boundaries is formed as the network of eutectic structure “leaks” between the grains.

A similar effect is observed when the sinter–brazing technique is implemented [7]. Prolonged contact of molten solder results in a network along the grain boundaries of the base material, which leads to cracking when the material cools down and shrinks. The presence of bronze in the structure of the grain boundaries of the bimetal transition zone represents a potential danger in terms of initiation of destruction during testing and operation. In particular, during the friction process, the grain boundary (or interparticle) network of the copper-containing phase can be deformed, which will reduce wear resistance by analogy with infiltrated powder steel [8]. The use of the material in the mode of frequent thermal cycles can lead to emergence of cracks, the localization of which can be associated with the iron–copper interphase boundaries within the transition zone, not only with the layers interface.

It should be noted in this regard that the quality assessment of bonding of bimetal layers should be comprehensive. It will provide for an objective and extensive analysis of the impact that the structural effects emerging during the bimetal production in the transition zone have on the products performance reliability. When the bonding strength of bimetal layers is evaluated according to the results of mechanical shear or pull tests, the grain boundary diffusion (or grain boundary wetting if the liquid phase is present) turns out to be a positive factor [9]. However, in light of the above, such a conclusion does not seem entirely legitimate, since under other test conditions, the network of plastic material along the grain boundaries in the transition zone can initiate deformation (pressing through) processes and cause defect formation.

Powder bimetals produced by the infiltration method are characterized by the presence of pores, which serve as reservoirs of liquid lubricant and help reduce the friction coefficient in the tribocoupling. Nevertheless, bimetals on a high-density steel substrate have higher tribological properties as this substrate is stronger [10]. Therefore, effective methods for producing high-density powder bimetals should be developed.

Tin bronzes are among the most common and promising materials used to obtain the bimetal working layer. In 2006, the European Union updated the RoHS regulation in order to ban lead and lead containing substances in the equipment [11]. Therefore, though lead-containing bronzes have an obvious advantage – they can reduce the bimetal friction coefficient by forming a film of structurally free lead in the tribocoupling –

when choosing the working layer material, it should be kept in mind that these bronzes will probably have to be replaced with lead-free ones.

The tribological properties of bronzes can be improved by introducing ultrafine additives of solid particles, which provide inhibition of plastic deformation in the soft copper phase [12–14]. Positive results were obtained when SiC particles were introduced into powder and compact bronzes [15; 16]. During friction, SiC particles are cut off and joined by adhesive bonds with the surface of the counterbody, which results in the formation of a thin film. The hard and durable SiC film formed between the tribocoupling surfaces minimizes the risk of plastic deformation and provides enhanced wear resistance.

When producing a copper–SiC composite by hot isostatic pressing (HIP), SiC particles disintegrate at temperatures above 850 °C, silicon diffuses into the copper matrix, and the resulting carbon, which is practically insoluble in copper, causes the formation of discontinuities and cracks in the zone of interfacial interaction. To prevent structural degradation, SiC particles are coated with molybdenum or titanium nitride [17; 18]. However, the coating is characterized by uneven thickness and ruptures, which results in individual pores on the interfacial areas during subsequent HIP.

The spark plasma sintering technique yields positive results in terms of preventing the structural degradation of SiC particles. However, it requires specialized equipment and causes technological difficulties when the formability characteristics and melting temperatures of the bimetal working layer and substrate materials are drastically different. The contact interfacial interaction is much less probable in case of hot forging (HF) of a composite blank in which SiC particles are coated with titanium nitride [18]. In the cited work, forging took 15 s. In Russian terminology adopted in powder metallurgy, such processes are called pressing, while forging is the name for additional compaction of a porous blank on high-speed mechanical presses or hammers (deformation continues for 50–100 and 2–8 ms, respectively) [19–21].

Hot forging of porous blanks (HFPB) of steel–BrO5Ts5S5 bronze bimetal with non-isothermal heating ensures the fabrication of a material with anti-friction properties, not inferior to cast analogues [22]. However, when a bimetallic blank is subject to non-isothermal heating, bronze can melt impregnating steel substrate pores localized in close proximity to the layers interface. The dimensions of the melting and impregnation zones are often uncontrollable, resulting in instability of the bimetal properties. Other destabilizing factors are liquation processes and

the grain boundary network of the copper-containing phase forming in the transition zone.

The method, which involves joint hot repressing of previously separately cold-pressed and sintered blanks of the working layer and substrates, is promising in terms of improving the mechanical and tribotechnical properties, as well as the quality of bonding of steel–bronze bimetal layers [23]. In this case, the working layer is heated through heat transfer from the side of the substrate warmed up to a higher temperature. The optimal duration of equalizing the assembly “substrate blank – working layer blank” until its hot repressing is determined by the formula obtained by solving heat balance set of equations. This enables to assign an optimal temperature regime for hot repressing characterized by the minimum required contact interaction of the bronze melt with the solid surface of the steel substrate. It has been established that when the bimetals of the “steel–bronze” type are produced by hot forging of separately heated substrate and working layer blanks, the optimal thermal conditions for the formation of the layer fusion zone are achieved when the substrate and working layer are heated to temperatures of 1150 and 520 °C, respectively. In this case, when a bimetal blank is assembled in a mold, thermal equilibrium is ensured at the interface at $t = 970 \div 990$ °C, which is accompanied by the formation of a small amount of liquid phase [24].

The purpose of this paper, which continues the earlier performed research, was to study the impact of technological conditions for producing hot-forged powder steel–bronze bimetal on the structure and features of thermal fatigue failure and tribological properties.

Methods

For structural analysis, thermal fatigue and tribotechnical tests, the bimetal samples with vertical and horizontal layers were obtained (Fig. 1). The atomi-

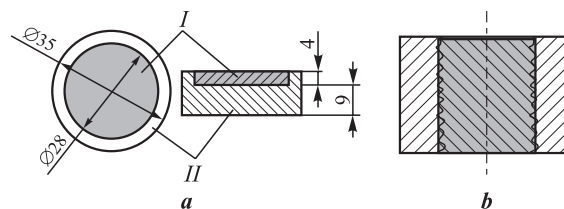


Fig. 1. Scheme of a bimetallic sample with horizontal (a) and vertical (b)

I – working layer, BrO10 bronze; *II* – substrate, PK40 steel

Рис. 1. Схема биметаллического образца с горизонтальным (a) и вертикальным (b) расположением слоев

I – рабочий слой, бронза БрО10; *II* – подложка, сталь ПК40

zed iron powder PZhRV 3.200.28 was used as a base for manufacturing substrate from PK40 steel (PJSC Severstal, Cherepovets). Graphite powder GK-3 (GOST 4404-78) was used as a carbonaceous additive. The working layer was made from BrO10 bronze powder obtained by spraying at Most-Tsvetmet LLC (Bataysk) (see the Table). To improve the tribotechnical characteristics of the working layer, bronze powder was mixed with superfine grinding micropowder F1000 of black silicon carbide 53S made by JSC Volzhsky Abrasive Works (Volzhsky). The particles of the initial micropowder were 1–10 μm in size and 0.5–1.0 μm after grinding.

The planetary ball mill SAND-1 (pilot plant, Yerevan) was used for grinding. The ratio of the mass of the grinding media to that of the crushed powder was 12:1. The grinding media were made of hard alloy. Grinding was performed in acetone, which was poured into the vessel with SiC powder. The content of SiC powder in the charge varied. To ensure a uniform distribution of SiC particles throughout the volume of bronze powder, the charge of the working layer material was also prepared in the planetary ball mill SAND-1, which minimized the likelihood of components segregation [25].

Flow diagrams for obtaining samples are presented in Fig. 2. Static cold pressing (SCP) of the substrate and working layer blanks was performed separately. The blanks porosity after SCP was 22–25 %. The cold-pressed substrate blank was sintered in a dissociated ammonia environment (1150 °C, 1 h). The porous blank of a bronze working layer was sintered at $t = 800$ °C for 1 h (flow diagram 2). Some working layer blanks were not sintered so that a comparative analysis could be conducted (flow diagram 3). Pre-deformation heating

of the blanks was conducted for 10 min. The optimal temperatures of 1150 and 520 °C were chosen for separate heating of the substrate and working layer blanks (flow diagrams 2, 3) [24].

Hot repressing of the porous working layer and substrate blanks was conducted jointly. The working layer blank was installed into the heated substrate blank. After equalizing the temperature in the volume of assembly of the bimetallic sample blank, HF was performed using a pendulum impact tester, the falling parts mass being 100 kg. The equalizing duration was determined using the equation given in [23].

Process flow diagram 1 presented a standard technology for producing hot-forged bimetals. In this case, the sintered bimetallic blank was heated at $t = 950$ °C and subjected to hot repressing.

The bimetal samples after HF were cooled in air. They were cut and the resulting parts were used for structural analysis, thermal fatigue and tribological tests. The quality of the connection of bimetal layers was assessed based on the thermal shock test results. In this case, the sample was heated in an inductor to a temperature of 870 °C and then cooled in water. After that, it was cleaned of scale and inspected for cracks and delaminations in the transition zone. The number of heating–cooling cycles until defects developed was recorded.

Thermal resistance enables to evaluate the resistance of a material to thermal shocks and plastic deformation [26]. Thermal fatigue failure develops under the impact of repeated plastic deformations when thermal stress exceeds the yield point. Thermal resistance is an informative criterion for assessing the degree of adhesive interaction at the interphase boundaries of heterogeneous and bimetallic materials.

Characteristics of the powders used

Характеристики используемых порошков

Material	Content, wt. %	Physical and technological properties			
		Granulometric composition	Apparent density ρ_h , g/cm ³	Flow rate, g/s	Compactibility at pressure 600 MPa, g/cm ³
PZhRV 3.200.28	Fe – base C – 0.03 O – 0.30 Si – 0.04 Mn – 0.12 P – 0.02 S – 0.01	+200 – 0 +160 – 3.7 +45 – 78.8 –45 + 17.5	2.72	32	7.27
BrO10	Cu – 90.130 Sn – 9.750 P – 0.198 O – 0.640	+150 – 5.50 +106 – 54.22 +75 – 21.04 +45 – 14.70 –45 – 4.54	3.30	30	7.68

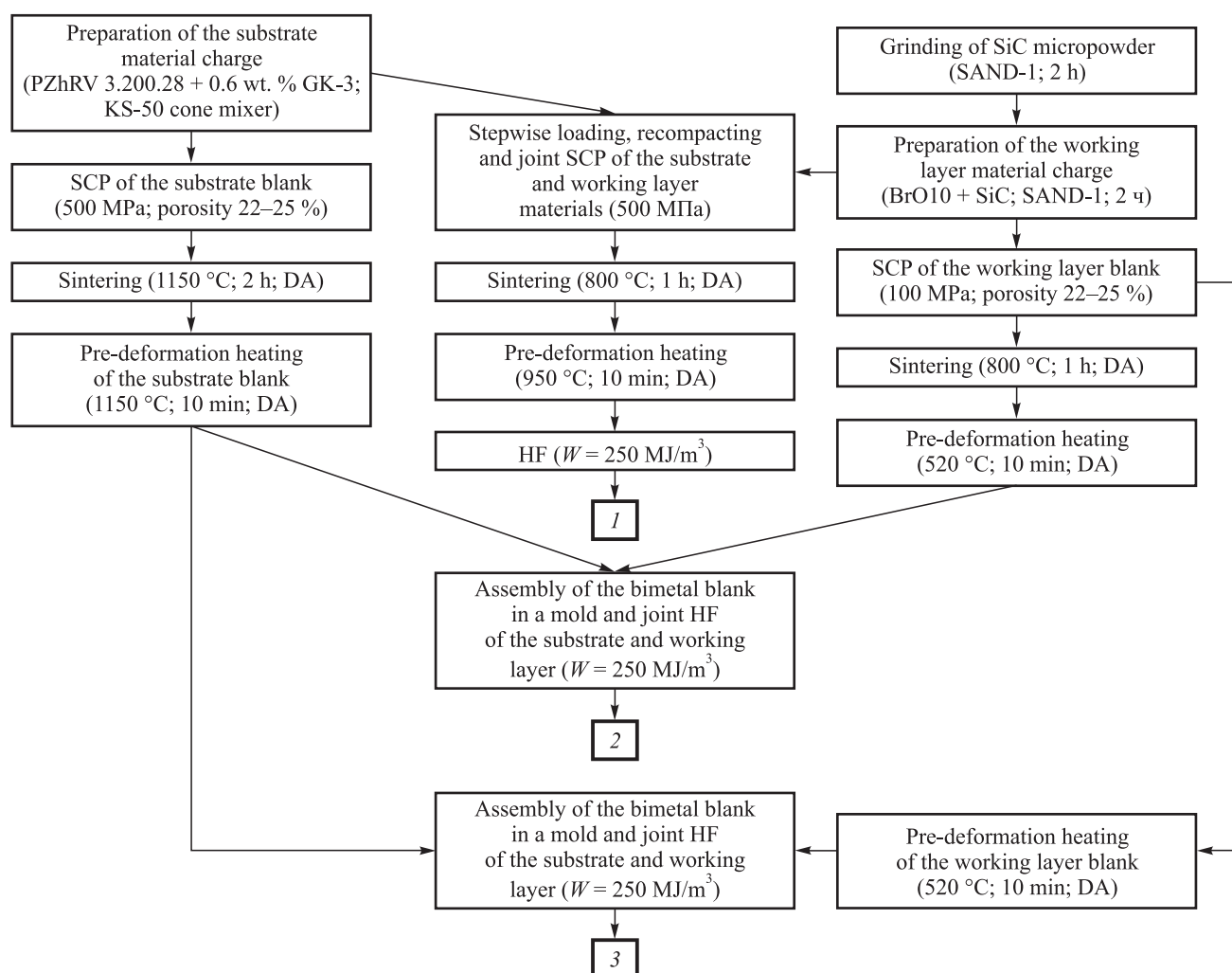


Fig. 2. Flow diagrams for producing hot-forged powder bimetal “PK40 steel–BrO10 bronze”

DA – dissociated ammonia, W – reduced compaction work

Рис. 2. Технологические схемы получения горячештампованного порошкового БМ «сталь ПК40 – бронза БрО10»

DA – диссоциированный аммиак, W – приведенная работа уплотнения

Tribotechnical tests were carried out on the friction machine MI in the dry friction mode according to the “shaft–block” scheme. The counterbodies were made of U8A steel, heat-treated to 50–55 HRC_e. The counterbodies had the following dimensions: outer and inner diameters – 50 and 12 mm, respectively, height – 15 mm, and working surface roughness – $R_a = 0.63 \mu\text{m}$. Before testing, the run-in of the sample was performed at a pressure of 2.5 MPa for 10 min, which ensured complete contact of the friction surfaces. The counterbody rotation frequency was 210 min⁻¹, the sliding speed was 0.55 m/s.

For metallographic studies, we used an AltamiMET-1M optical microscope (Altami LLC, Russia) and a Quanta 200 i 3D scanning microscope-microanalyzer (FEI Company, USA). Unetched and etched sections were studied. Etching was performed in 3 % nital, since it provides sufficient contrast when

the structure of the bimetal transition zone and the substrate material, PK40 steel, is analyzed.

Microhardness was measured using a HVS-1000 digital microhardness tester (L.H. Testing Instruments Co., Ltd, China) according to GOST 9450-76 (0.2 N; 10 s).

Results and discussion

The maximum values of heat resistance were demonstrated by samples with a horizontal arrangement of layers, fabricated by hot repressing of sintered working layer and substrate blanks, assembled in a mold before deformation (flow diagram 2 in Fig. 2; Fig. 3, curve 1). The fracture sites are multiple and are mainly associated with the “steel–bronze” interphase boundaries in the transition zone on the substrate side (Fig. 4, a). This zone is characterized by pores and discontinuities filled with molten bronze upon contact

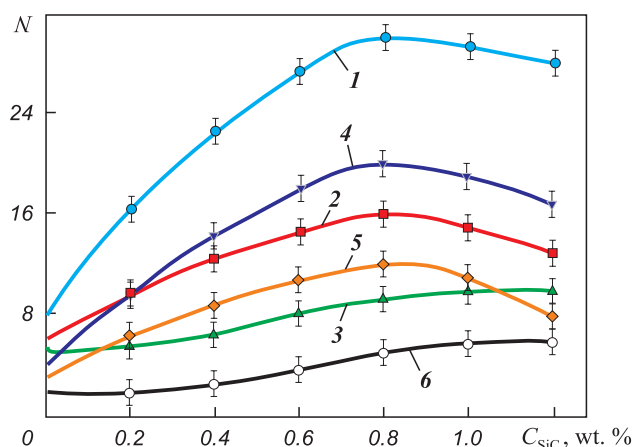


Fig. 3. Impact of the SiC content in the working layer material charge on the bimetal thermal resistance

1–3 – horizontal arrangement of layers, 4–6 – vertical arrangement of layers 2, 5 – process flow diagram 1; 1, 4 – flow diagram 2; 3, 6 – flow diagram 3
N – number of cycles

Рис. 3. Влияние содержания SiC в шихте материала рабочего слоя на термостойкость БМ

1–3 – горизонтальное расположение слоев, 4–6 – вертикальное
2, 5 – технологическая схема 1; 1, 4 – схема 2; 3, 6 – схема 3
N – число циклов

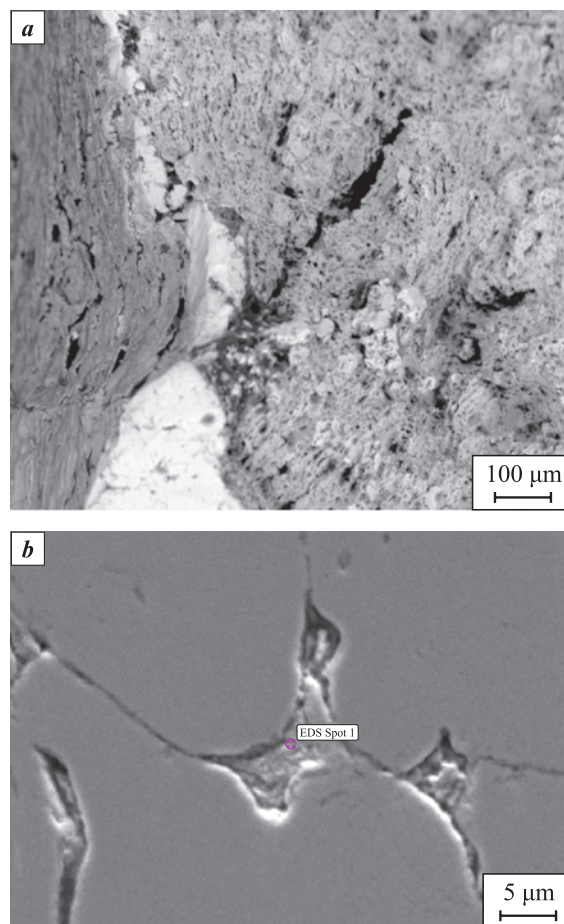
of a substrate blank heated to 1150 °C with a relatively cold (520 °C) working layer blank. The impregnation depth is 0.2–0.5 mm.

During thermal cycling, microcracks also form in the working layer material at the “matrix-SiC” interface (Fig. 4, b). Cracking of agglomerates of SiC particles is observed in the samples containing more than 0.8 wt.% silicon carbide.

The structure of the working layer includes the α phase and the eutectoid $\alpha + \delta$. The substrate structure consists of ferrite perlite. Pearlite is sorbitic, 340–360 HV (Fig. 5). Wetting of the steel substrate grain boundaries with molten bronze is not observed. A ferrite strip (140–160 HV) is adjacent to the interface on the substrate side, with the pearlite zone located below. The formation of a banded structure (ferrite strip – pearlite strip) in the transition zone on the substrate side is attributed to the displacement of carbon forming part of austenite, from the interface during the copper diffusion into steel [2].

The $N(C_{SiC})$ dependence is non-monotonic: an increase in C_{SiC} to 0.8 wt. % results in enhanced thermal stability as dispersed SiC particles strengthen interparticle boundaries of the working layer material. A further growth of C_{SiC} causes a drop in thermal stability as agglomerates of silicon carbide particles are formed.

The thermal stability of the control samples (flow diagram 1) is noticeably lower (Fig. 3, curve 2) compared to the bimetal fabricated according to flow dia-



C	Fe	Si	Total
35.2	7.5	57.3	100.0

Fig. 4. Formation of cracks during thermal-cycle fatigue failure of bimetal and elemental analysis of a selected area of the working layer material

Flow diagram 2, $C_{SiC} = 0.8$ wt. %

a – transition zone; b – working layer, “matrix-SiC” interface

Рис. 4. Формирование трещин при термоциклическом усталостном разрушении БМ и элементный анализ выделенной области материала рабочего слоя

Схема 2, $C_{SiC} = 0,8$ мас. %

a – переходная зона;

b – рабочий слой, граница раздела «матрица-SiC»

gram 2 (Fig. 3, curve 1). This is attributed to unfavorable temperature conditions for sintering and hot deformation of the steel substrate and the bimetal transition zone: sintering at $t = 800$ °C and hot repressing at $t = 950$ °C do not ensure the formation of cohesive bonds between iron powder particles and lead to residual pores in the substrate and at the bimetal layers interface. In this case, the impact of SiC particles on thermal stability is also non-monotonic.

The lowest heat resistance was demonstrated by the samples fabricated according to process flow diagram 3, the implementation of which did not include

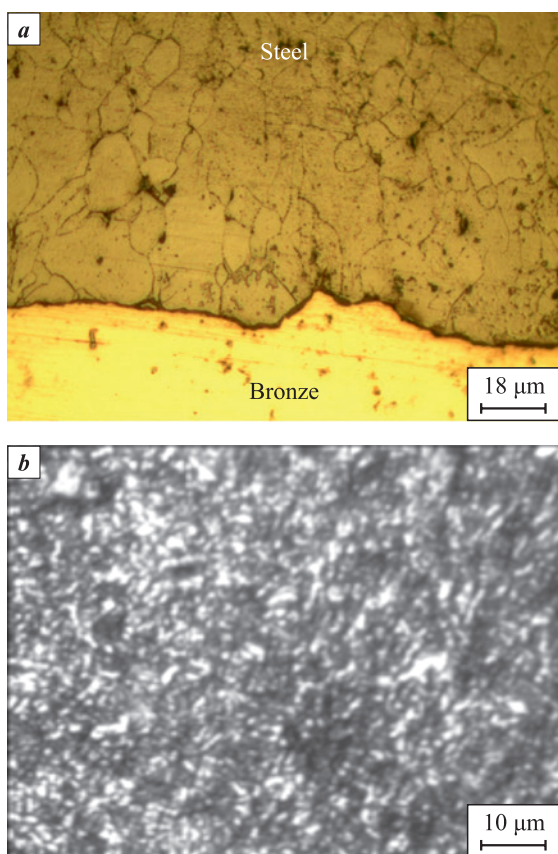


Fig. 5. Microstructure of hot-forged powder bimetal

Flow diagram 2, $C_{SiC} = 0.8$ wt. %
a – transition zone; **b** – substrate, PK40 steel
 Horizontal layer arrangement

Рис. 5. Микроструктура горячештампованного порошкового БМ

Схема 2, $C_{SiC} = 0,8$ мас. %
a – переходная зона; **b** – подложка, сталь ПК40
 Расположение слоев горизонтальное

sintering of cold-pressed working layer blanks (Fig. 3, curve 3). During the tests, cracks formed both at the layers interface and in the working layer material (Fig. 6, *a*).

The samples of this group proved more prone to crack formation due to high probability of hydrogen embrittlement of copper alloys [27]. The oxygen content in the initial BrO10 powder is 0.64 wt. % (see the Table). When the sample is heated during sintering and before hot deformation in a dissociated ammonia environment, copper-containing oxides, localized at interparticle and grain boundaries, are reduced, with the water vapor being formed, which leads to the appearance of bubbles, cracks and delaminations.

During 1 h sintering, the conditions were provided for removing steam from the body of the working layer blank. Delaminations and cracks formed at the sintering stage were eliminated during subsequent hot deformation (Fig. 6, *b*). In contrast, during joint hot repressing of the substrate and the unsintered working layer

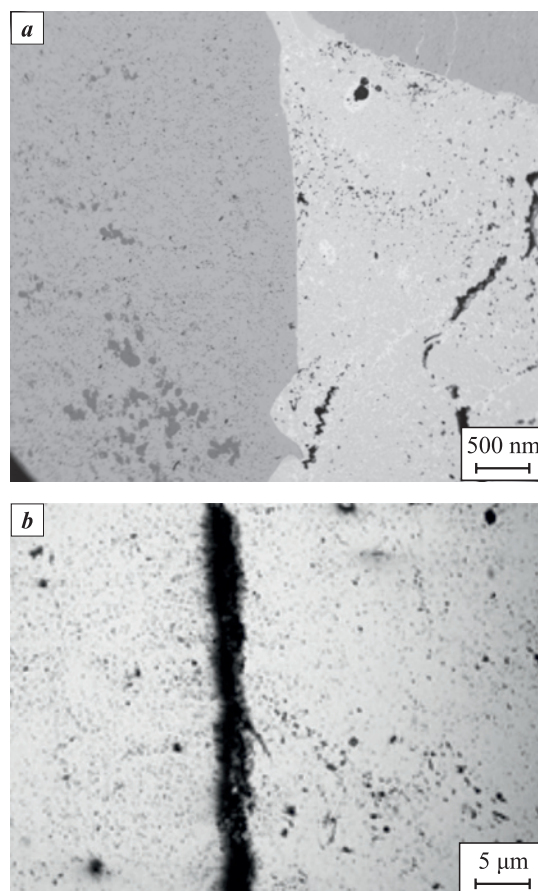


Fig. 6. Microstructure of powder bimetal (flow diagram 3) after thermal fatigue tests (*a*) and in the as-sintered state (*b*)

Horizontal layer arrangement, $C_{SiC} = 0.8$ wt. %

Рис. 6. Микроструктура порошкового БМ (схема 3) после испытаний на термоусталость (*a*) и в состоянии после спекания (*b*)

Расположение слоев горизонтальное, $C_{SiC} = 0,8$ мас. %

blank, these defects formed almost synchronously with the deformation, making their elimination unlikely. The impact of this factor was predominant, outweighing the strengthening effect of SiC additives.

The above-described features of the impact of C_{SiC} on the thermal stability of the samples with horizontal layers are also valid for the samples with vertical layers (Fig. 3, curves 4–6). The difference is that their absolute value of heat resistance is lower, which is attributed to greater magnitude of thermal stresses that develop in the sample material during testing.

Maximum wear resistance was demonstrated by bimetal samples obtained according to flow diagram 2, containing 0.8 wt. % SiC (Fig. 7, curve 1). In this case, the dependence $f(P)$ is non-monotonic: as P increases in the range of 3–5 MPa, the friction coefficient f drops. Apparently, this is attributed to the formation of a solid SiC film on the tribocoupling surfaces (Fig. 7, *a*; curve 4) [16].

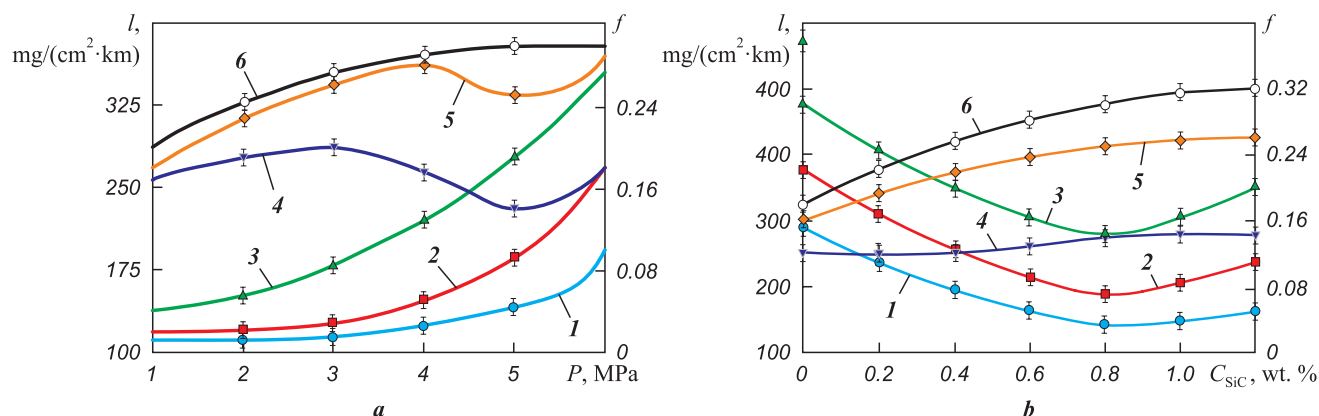


Fig. 7. Dependences of the wear (1–3) and friction coefficient (4–6) of the bimetal working layer on the specific load (a) and SiC content (b) during tests under dry friction conditions
2, 5 – process flow diagram 1; 1, 4 – flow diagram 2; 3, 6 – flow diagram 3
a – $C_{SiC} = 0.8$ wt. %; b – $P = 5$ MPa
Horizontal layer arrangement

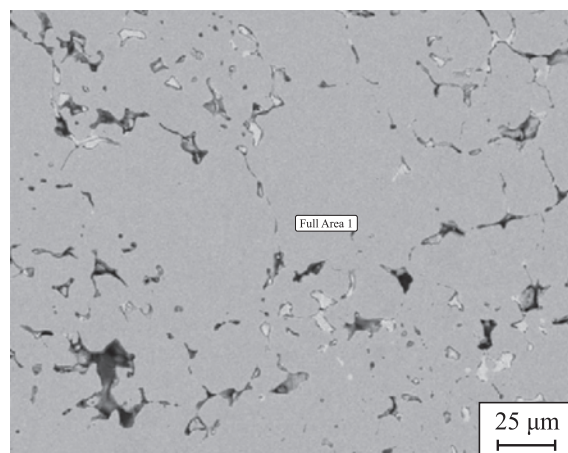
Рис. 7. Зависимости износа (1–3) и коэффициента трения (4–6) материала рабочего слоя БМ от удельной нагрузки (a) и содержания SiC (b) при испытаниях в условиях сухого трения
2, 5 – технологическая схема 1; 1, 4 – схема 2; 3, 6 – схема 3
a – $C_{SiC} = 0,8$ мас. %; b – $P = 5$ МПа
Расположение слоев горизонтальное

The wear resistance of the samples fabricated according to flow diagrams 1 and 3 is noticeably lower. An increased load during testing of samples fabricated according to flow diagram 1 in the range of 4–5 MPa leads, as in the previous case, to a slight drop of the friction coefficient, but its absolute values remain quite high (Fig. 7, a; curve 5). The samples fabricated according to flow diagram 3 are characterized by discontinuities and microcracks localized near the “SiC–bronze” boundaries, the formation mechanism of which is described above (Fig. 8). SiC particles, weakly bonded with the matrix material, flake during friction, which pushes up the wear values and the friction coefficient (Fig. 7, a; curve 3, 6). After testing, deep scratches formed as a result of the abrasive impact of SiC particles are visualized on the samples working surface.

An enhanced abrasive effect caused by an increased content of SiC particles in the working layer material results in the growth of the f values of the samples fabricated according to flow diagram 3 (Fig. 7, b; curve 6). At the same time, the absolute wear values are high, despite their decrease in the range $C_{SiC} = 0 \div 0.8$ wt. % (Fig. 7, b; curve 3). The latter is apparently attributed to dispersion strengthening of interparticle boundaries and inhibition of plastic deformation in the bronze layer during friction [12].

Compared to the studied group of samples, the wear resistance of the control samples (flow diagram 1) is higher, and the f values are lower (Fig. 7, b; curve 2 and 5 respectively). The $f(C_{SiC})$ dependence is mono-

tonic: growing C_{SiC} leads to an increase in f values. In contrast to the samples fabricated according to flow diagram 3, high values of wear and friction coefficient are attributed not to defects in the working layer, but to undercompaction of the substrate and transi-



C	Fe	Si	Total
29.1	9.3	61.6	100.0

Fig. 8. Microstructure of hot-forged powder bimetal and elemental analysis of the material selected area
Flow diagram 3; working layer; $C_{SiC} = 0.8$ wt. %;
horizontal layer arrangement

Рис. 8. Микроструктура горячештампованного порошкового БМ и элементный анализ выделенной области материала
Схема 3; рабочий слой; $C_{SiC} = 0,8$ мас. %;
расположение слоев горизонтальное

tion zone, caused by the relatively low temperature of pre-deformation heating (950 °C). The porosity of the substrate of these samples amounted to 5–7 %. The residual pores in the substrate result in the working layer being “pressed through” during loading in the course of tests. The effect of this factor was predominant, though introduction of SiC particles caused the effect of dispersion strengthening of the bronze layer (Fig. 7, b; curve 2).

The implementation of flow diagram 2 ensured optimal conditions for the structure formation. In this case, the samples had the lowest values of wear and friction coefficient (Fig. 7, b; curves 1 and 4). The dependence of f values on C_{SiC} in the studied concentration range is rather weak. The samples containing 0.8 wt. % SiC demonstrated the greatest wear resistance. The residual porosity of the substrate and working layer materials is 0.5–1.0 wt. %.

Conclusions

1. We proposed the technique for producing hot-forged powder bimetal “PK40 steel–BrO10 bronze”, which includes the following independent procedures: cold pressing of the substrate and working layer blanks, their sintering in a reducing environment, pre-deformation heating of the substrate and working layer at temperatures that ensure their satisfactory formability, assembly of heated substrate and working layer blanks in the mold and subsequent joint hot repressing. The resulting bimetal is characterized by increased values of thermal fatigue and wear resistance in comparison with the control samples manufactured using the traditional technology of hot repressing of the cold-pressed bimetallic blank.

2. The introduction of SiC powder into the working layer material contributes to the bimetal thermal and wear resistance enhancement due to dispersion strengthening of the interparticle boundaries. The optimal content of SiC additive is 0.8 wt. %.

3. Preliminary sintering of the porous working layer blank enables to reduce the oxides that form part of the bronze powder and later to remove the reaction products from the body of the blank, which hinders defect formation during hot deformation.

References / Список литературы

1. Malevskii Yu.B., Nesmikh V.S. Pressure welding of bronze to steel. Moscow: Metallurgiya, 1981. 346 p. (In Russ.).
Малевский Ю.Б., Несмих В.С. Сварка давлением бронзы со сталью. М.: Metallurgiya, 1981. 108 с.
2. Golovatenko S.A., Meandrov L.V. Production of bimetals. Moscow: Metallurgiya, 1966. 304 p. (In Russ.).
3. Головатенко С.А., Меандров Л.В. Производство биметаллов. М.: Metallurgiya, 1966. 304 с.
4. Kurt A., Uygur I., Mutlu E. The effect of allotropic transformation temperature in diffusion-welded low-carbon steel and copper. *Metallorfizika i Noveishie Tekhnologii*. 2006;28(1):39–52. URL: https://www.researchgate.net/publication/290710978_The_effect_of_allotropic_transformation_temperature_in_diffusion-welded_low-carbon_steel_and_copper (accessed: 23.05.2023).
5. Ustinov A.I., Fal'chenko Yu.V., Mel'nichenko T.V., Petrushinets L.V., Lyapina K.V., Shishkin A.E., Guriyenko V.P. Diffusion welding of steel to tin bronze through porous interlayers of nickel and copper. *The Paton Welding Journal*. 2015;2015(9):13–19.
<https://doi.org/10.15407/tpwj2015.09.02>
6. Устинов А.И., Фальченко Ю.В., Мельниченко Т.В., Петрушинец Л.В., Ляпина К.В., Шишкин А.Е., Гуриенко В.П. Диффузионная сварка стали с оловянной бронзой через пористые прослойки никеля и меди. *Автоматическая сварка*. 2015;745(9):15–21. URL: <https://elibrary.ru/item.asp?id=24141303> (дата обращения: 23.05.2023).
7. Wang X., Tang B., Wang L., Wang D., Dong W., Li X. Microstructure, microhardness and tribological properties of bronze-steel bimetallic composite produced by vacuum diffusion welding. *Materials*. 2022;15(4):1588.
<https://doi.org/10.3390/ma15041588>
8. Zou J., Li S., Wei Ya., Liang Sh. Research of the bonded interface of Cu9Al4Fe/1Cr18Ni9Ti stainless steel bimetallic composite. *Vacuum*. 2017;146:266–273.
<https://doi.org/10.1016/j.vacuum.2017.10.005>
9. Galán-Salazar A., Campos M., Torralba J. M., Kjellén L., Mårs O. The base material: A key factor in sinter-brazing. *Metal Powder Report*. 2017;72(5):349–354.
<https://doi.org/10.1016/j.mprp.2016.03.001>
10. D'yachkova L.N., Dmitrovich A.A. Structural changes in powder composite materials based on iron during wear. In: *Powder metallurgy*. Minsk: Belaruskaya navuka, 2009. Iss. 32. P. 142–146. (In Russ.).
Дьячкова Л.Н., Дмитривич А.А. Структурные изменения порошковых композиционных материалов на основе железа в процессе изнашивания. В сб.: *Порошковая металлургия*. Минск: Беларуская навука, 2009. Вып. 32. С. 142–146.
11. Xiong J., Xie Q., Li J., Zhang F., Huang W. Diffusion bonding of stainless steel to copper with tin bronze and gold interlayers. *Journal of Materials Engineering and Performance*. 2012;21(1):33–37.
<https://doi.org/10.1007/s11665-011-9870-y>
12. D'yachkova L.N., Voronetskaya L.Ya., Pinchuk T.I. Tribotechnical properties of two-layer powder and compact-powder materials based on iron and copper. In: *Powder metallurgy*. Minsk: Belaruskaya navuka, 2018. Iss. 41. P. 177–183. (In Russ.).
Дьячкова Л.Н., Воронетская Л.Я., Пинчук Т.И. Триботехнические свойства двухслойных порошковых и компактно-порошковых материалов на основе железа и меди. В сб. *Порошковая металлургия*. Минск: Беларуская навука, 2018. Вып. 41. С. 177–183.
13. Fürtauer S., Li D., Cupid D., Flandorfer H. The Cu–Sn phase diagram. Part I: New experimental results. *Interme-*

- tallics. 2013;34:142–147.
<http://dx.doi.org/10.1016/j.intermet.2012.10.004>
12. D'yachkova L.N. Powder materials based on iron with enhanced mechanical and tribological properties. Minsk: Belaruskaya navuka, 2020. 203 p. (In Russ.).
Дьячкова Л.Н. Порошковые материалы на основе железа с повышенными механическими и триботехническими свойствами. Минск: Беларуская навука, 2020. 203 с.
13. D'yachkova L., Fel'dshtein E.E. On the properties of composites based on sintered bronze with alumina additives. *Composites: Part B*. 2013;45:239–247.
<http://dx.doi.org/10.1016/j.compositesb.2012.07.024>
14. D'yachkova L.N., Fel'dshtein E.E., Vityaz' P.A. Tribological behavior of sintered tin bronze with additions of alumina and nickel oxide. *Journal of Friction and Wear*. 2013;34(1):19–26.
<https://doi.org/10.3103/S1068366613010042>
15. Rozhkova T.V., Paul's V.Yu. Preparation of composite materials based on copper. *Electronic scientific and methodical journal of the Omsk State Agrarian University*. 2019;17(2):00724. (In Russ.).
URL: <http://ejournal.omgau.ru/images/issues/2019/2/00724.pdf> (accessed: 23.05.2023). (In Russ.).
Рожкова Т.В., Паульс В.Ю. Получение композиционных материалов на основе меди. *Электронный научно-методический журнал Омского ГАУ*. 2019;17(2):00724. URL: <http://ejournal.omgau.ru/images/issues/2019/2/00724.pdf> (дата обращения: 23.05.2023).
16. Sharma S.C., Satish B.M., Girish B.M., Somashekar D.R. Wear characteristics of phosphor-bronze/silicon carbide particulate composites. *Journal of Materials Processing Technology*. 2001;118(1):65–68.
[https://doi.org/10.1016/S0924-0136\(01\)00868-8](https://doi.org/10.1016/S0924-0136(01)00868-8)
17. Schubert Th., Brendel A., Schmid K., Koeck Th., Ciupin'ski L., Zielin'ski W., Weißgärber T., Kieback B. Interfacial design of Cu/SiC composites prepared by powder metallurgy for heat sink applications. *Composites: Part A*. 2007;38(12):2398–2403.
<https://doi.org/10.1016/j.compositesa.2007.08.012>
18. Sundberg G., Paul P., Sung Ch., Vasilos Th. Fabrication of CuSiC metal matrix composites. *Journal of Materials Science*. 2006;41:485–504.
<https://doi.org/10.1007/s10853-005-2622-3>
19. Tuchinskii L.I. Solid-phase consolidation of reinforced metals. Kiev: Naukova dumka, 1980. 116 p. (In Russ.).
Тучинский Л.И. Твердофазное уплотнение армированных металлов. Киев: Наукова думка, 1980. 116 с.
20. Dorofeyev Yu.G., Gasanov B.G., Dorofeyev V.Yu., Miroshnikov V.I., Mishchenko V.N. Industrial technology of hot pressing of powder products Moscow: Metallurgiya, 1990. 206 p. (In Russ.).
Дорофеев Ю.Г., Гасанов Б.Г., Дорофеев В.Ю., Мирошников В.И., Мищенко В.Н. Промышленная технология горячего прессования порошковых изделий. М.: Металлургия, 1990. 206 с.
21. Hendrickson A.A., Machmeier P.M., Smith D.W. Impact forging of sintered steel preforms. *Powder Metallurgy*. 2000;43(4):327–344.
<http://dx.doi.org/10.1179/003258900666050>
22. Semchenkov V.P. Development of the technology of hot forging of bimetal “steel-bronze” type with a powder working layer: Abstract of the dissertation of PhD. Novocherkassk: SRSPU (NPI), 2000. (In Russ.).
Семченков В.П. Разработка технологии горячей штамповки биметалла типа «сталь–бронза» с порошковым рабочим слоем: Автореф. дис. ... канд. техн. наук. Новочеркасск: ЮРГТУ (НПИ), 2000.
23. Dorofeyev Yu.G., Dorofeyev V.Yu., Babets A.V., Bessarabov E.N. Obtaining and properties of powder bimetallic materials and products. In: *Powder metallurgy: surface engineering, new powder composite materials. Welding: Materials of the 8th Intern. Symposium (Minsk, April 10–12, 2013)*. Minsk: Belaruskaya navuka, 2013. Pt. 1. P. 182–188. (In Russ.).
Дорофеев Ю.Г., Дорофеев В.Ю., Бабец А.В., Бессарабов Е.Н. Получение и свойства порошковых биметаллических материалов и изделий. В сб.: *Порошковая металлургия: инженерия поверхности, новые порошковые композиционные материалы. Сварка: Материалы 8-го Междунар. симпозиума (г. Минск, 10–12 апреля 2013 г.)*. Минск: Беларуская навука, 2013. Ч. 1. С. 182–188.
24. Dorofeyev Yu.G., Babets A.V., Bessarabov E.N., Dorofeyev V.Yu. Obtaining powder bimetallics of the “steel-bronze” type by hot forging separately heated porous blanks of layer materials. In: *Powder metallurgy: surface engineering, new powder composite materials. Welding: Materials of the 9th Intern. Symposium (Minsk, April 8–10, 2015)*. Minsk: Belaruskaya navuka, 2015. Pt. 1. P. 86–93. (In Russ.).
Дорофеев Ю.Г., Бабец А.В., Бессарабов Е.Н., Дорофеев В.Ю. Получение порошковых биметаллов типа «сталь–бронза» горячей штамповкой раздельно нагретых пористых заготовок материалов слоев. В сб.: *Порошковая металлургия: инженерия поверхности, новые порошковые композиционные материалы. Сварка: Материалы 9-го Междунар. симпозиума (г. Минск, 8–10 апреля 2015 г.)*. Минск: Беларуская навука, 2015. Ч. 1. С. 86–93.
25. Prosviryakov A.S., Aksenov A.A., Samoshina M.E., Kovaleva M.G., Ivanov D.O. Mechanical alloying of Cu–SiC materials prepared with utilization of copper waste chips. *Powder Metallurgy*. 2011;54(3):382–384.
<https://doi.org/10.1179/003258910X12707304454942>
26. Komarov O.S. Improving the technology for producing castings from high-chromium cast iron. Moscow: Novoe znanie, 2014. 152 p. (In Russ.).
Комаров О.С. Совершенствование технологии получения отливок из высокохромистого чугуна. М.: Новое знание, 2014. 152 с.
27. Il'yushchenko A.Ph., Markova L.V., Chekan V.A., Fomikhina I.V., Koleda V.V. Atlas of industrial fractures of various structures made of non-ferrous metals and alloys. Minsk: Belaruskaya navuka, 2022. 364 p. (In Russ.).
Ильющенко А.Ф., Маркова Л.В., Чекан В.А., Фомихина И.В., Коледа В.В. Атлас производственных разрушений различных конструкций из цветных металлов и сплавов. Минск: Беларуская навука, 2022. 364 с.

Information about the Authors



Vladimir Yu. Dorofeyev – Dr. Sci. (Eng.), Professor at the Department of Engineering Technology, Technological Machines and Equipment, Platov South-Russian State Polytechnic University (PSRSPU (NPI))

ORCID: 0000-0001-6743-1727

E-mail: dvyu56.56@mail.ru

Evgeniy N. Bessarabov – Cand. Sci. (Eng.), Associate Professor at the Department of International Logistics Systems and Complexes, PSRSPU (NPI)

ORCID: 0000-0002-6059-9831

E-mail: bess_555en@mail.ru

Anna N. Sviridova – Cand. Sci. (Eng.), Associate Professor at the Department of Automobiles and Transport-Technological Complexes, PSRSPU (NPI)

ORCID: 0000-0002-9851-1073

E-mail: anysviridova@yandex.ru

Inna V. Ivanova – Cand. Sci. (Eng.), Associate Professor at the Department of Engineering Technology, Technological Machines and Equipment, PSRSPU (NPI)

ORCID: 0000-0001-9999-4049

E-mail: ivicivanova@yandex.ru

Lev I. Svistun – Dr. Sci. (Eng.), Professor at the Department of Engineering of Control Systems, Materials and Technologies in Mechanical Engineering, Kuban State Technological University

ORCID: 0009-0001-8552-2582

E-mail: levsvistun45@gmail.com

Roman A. Vodolazhenko – Cand. Sci. (Eng.), Associate Professor at the Department of Mathematics, Synergy University

ORCID: 0000-0002-7638-6021

E-mail: vra35977@gmail.com

Сведения об авторах

Владимир Юрьевич Дорофеев – д.т.н., профессор кафедры «Технология машиностроения, технологические машины и оборудование» Южно-Российского государственного политехнического университета им. М.И. Платова (ЮРГПУ (НПИ))

ORCID: 0000-0001-6743-1727

E-mail: dvyu56.56@mail.ru

Евгений Николаевич Бессарабов – к.т.н., доцент кафедры «Международные логистические системы и комплексы» ЮРГПУ (НПИ)

ORCID: 0000-0002-6059-9831

E-mail: bess_555en@mail.ru

Анна Николаевна Свиридова – к.т.н., доцент кафедры «Автомобили и транспортно-технологические комплексы» ЮРГПУ (НПИ)

ORCID: 0000-0002-9851-1073

E-mail: anysviridova@yandex.ru

Инна Викторовна Иванова – к.т.н., доцент кафедры «Технология машиностроения, технологические машины и оборудование» ЮРГПУ (НПИ)

ORCID: 0000-0001-9999-4049

E-mail: ivicivanova@yandex.ru

Лев Иванович Свистун – д.т.н., профессор кафедры «Инженерия систем управления, материалов и технологий в машиностроении» Кубанского государственного технологического университета

ORCID: 0009-0001-8552-2582

E-mail: levsvistun45@gmail.com

Роман Анатольевич Водолаженко – к.т.н., доцент кафедры математики университета «Синергия»

ORCID: 0000-0002-7638-6021

E-mail: vra35977@gmail.com

Contribution of the Authors



V. Yu. Dorofeyev – scientific supervision, setting the goal and objectives of the study, manuscript writing, formulating conclusions.

E. N. Bessarabov – preparing, conducting and supervising the experiment.

A. N. Sviridova – conducting thermal fatigue tests, analyzing research results.

I. V. Ivanova – conducting tribological tests.

L. I. Svistun – formulating the main concept, editing the text and conclusions.

R. A. Vodolazhenko – studying the structure and composition of test samples.

Вклад авторов

В. Ю. Дорофеев – научное руководство, постановка цели и задачи исследования, подготовка текста, формулировка выводов.

Е. Н. Бессарабов – подготовка и проведение эксперимента, руководство проведением эксперимента.

А. Н. Свиридова – проведение термоусталостных испытаний, анализ результатов исследований.

И. В. Иванова – проведение трибологических испытаний.

Л. И. Свистун – формирование основной концепции, редактирование текста и выводов.

Р. А. Водолаженко – проведение исследований структуры и состава опытных образцов.

Received 18.05.2023

Revised 24.06.2023

Accepted 27.06.2023

Статья поступила 18.05.2023 г.

Доработана 24.06.2023 г.

Принята к публикации 27.06.2023 г.



UDC 669.018.25

<https://doi.org/10.17073/1997-308X-2024-3-28-37>

Research article
Научная статья



Features of the linear intercept method used for measuring the grain size in WC–Co hardmetals

V. A. Pesin, M. V. Vasilyeva[✉], A. S. Osmakov

“Virial” Ltd.

27 Bld. R Engels Prosp., Saint-Petersburg 194156, Russia

✉ VasilyevaMV@virial.ru

Abstract. Several WC–Co hardmetals with varying WC grain size distributions were analyzed to measure the mean grain size using the linear intercept (L) and planimetric (d_j) methods. Additional measurements included the equivalent diameter (d_{eq}) and mean chords (d_{ch}) for all grains, and separately, for grains intersected by the line. The findings show that mean sizes and size distributions of grains intersected by the line differ from those of all grains. This discrepancy is attributed to the linear intercept method’s rule for drawing secants, leading to “shadowing” where finer grains are obscured by coarser ones. The relationship between the mean sizes of all grains and those intersected by the line can be quantified using the “shadow” function S , which depends on the coefficient of variation (c_v) of the WC grain size distribution, as $d^3/d^1 = 1 - S$. Experimental data illustrate that the mean equivalent diameter d_{eq} correlates with the linear intercept method L through equation $d_{eq}/L = 1.4(1 - S)$, and the relationship between the mean grain size d_j and L are described by the equation $d_j/L = 1.4(1 - S)\sqrt{1 + c_v^2}$. The analysis of grain distributions by the equivalent diameters and mean chords showed that they equally describe the alloy grain size distribution. The length distribution of random chords obtained using the linear intercept method differs from the alloy grain size distribution due to the shadow effect, and also because the length distribution of random chords is always broader than the mean grain chord distribution. It is demonstrated that the length distribution of random chords is a convolution of the grain size distribution function and a function related to the grain shape.

Keywords: grain size, grain size distribution, linear intercept method, planimetric method, shadow effect

For citation: Pesin V.A., Vasilyeva M.V., Osmakov A.S. Features of the linear intercept method used for measuring the grain size in WC–Co hardmetals. *Powder Metallurgy and Functional Coatings*. 2024;18(3):28–37.
<https://doi.org/10.17073/1997-308X-2024-3-28-37>

Особенности метода секущих, используемого для определения размера зерна в сплавах WC–Co

В. А. Песин, М. В. Васильева[✉], А. С. Осмаков

ООО «Вириал»

Россия, 194156, г. Санкт-Петербург, пр-т Энгельса, 27Р

✉ VasilyevaMV@virial.ru

Аннотация. На ряде сплавов WC–Co с различной шириной распределения зерен WC по размерам проведены измерения средних размеров зерен методом секущих (L) и планиметрическим методом ($d_{дж}$), а также эквивалентных диаметров ($d_{экв}$) и средних хорд (d_x) на всех зернах и отдельно на зернах, лежащих на секущих. Установлено, что как значения средних размеров, так и распределения по размерам зерен, лежащих на секущих, и всех зерен не совпадают. Это обусловлено правилом проведения секущих в методе секущих и связанным с ним «затенением» мелких зерен крупными. Показано, что отношение средних размеров всех зерен к средним размерам зерен на линиях можно описать с использованием «теневой» функции S , зависящей от коэффициента вариации (c_v) распределения зерен WC по размерам, в виде $d^3/d^1 = 1 - S$. Экспериментальные соотношения между средним эквивалентным диаметром $d_{экв}$ и средним размером зерна по методу секущих L описываются выражением

$d_{\text{экв}}/L = 1,4(1 - S)$, а соотношения между средним размером зерна $d_{\text{дж}}$ и L – выражением $d_{\text{дж}}/L = 1,4(1 - S)\sqrt{1 + c_v^2}$. Анализ распределений зерен по величине эквивалентных диаметров и средних хорд показал, что они в одинаковой степени описывают распределение зерен сплава по размерам. Распределение случайных хорд по длине, получаемое в методе секущих, не соответствует распределению зерен сплава по размерам из-за теневого эффекта и из-за того, что распределение длин случайных хорд всегда шире распределения средних хорд зерен. Показано, что распределение длин случайных хорд является сверткой функции распределения зерен по размерам и функцией, связанной с формой зерен.

Ключевые слова: размер зерна, распределение зерен по размерам, метод секущих, планиметрический метод, теневой эффект

Для цитирования: Песин В.А., Васильева М.В., Осмаков А.С. Особенности метода секущих, используемого для определения размера зерна в сплавах WC–Co. *Известия вузов. Порошковая металлургия и функциональные покрытия*. 2024;18(3):28–37. <https://doi.org/10.17073/1997-308X-2024-3-28-37>

Introduction

The core parameters of the microstructure of metals and alloys, which determine their mechanical and physical properties, are the grain size and material grain size distribution [1–6]. The grain size measuring methods use different characteristics of the grain to determine its size, which impedes the comparability of findings presented by different authors.

Historically, the linear intercept method [7] was the first one for estimating grain sizes in metals and alloys, including hardmetals. To this day, it is the most widely used technique despite the development of the image analysis methods. According to the linear intercept method, a series of parallel lines (secants) are drawn on the image of the alloy microstructure and the lengths of intercepts (random chords) intersecting each grain that happens to be on one of these lines are measured. It should be noted that the same grain cannot be intersected several times. The mean alloy grain size is taken to be the arithmetic mean of the lengths of these chords, hereinafter referred to as L . Some authors use the distribution of random chord lengths as the grain size distribution [4; 8–12].

The second most popular method for estimating grain sizes is the Jefferies planimetric method [13], in which the mean grain area is determined by dividing the cross-section area of the sample (image) by the number of grains contained in it. Then this area is converted into the diameter of a circle of the same area, dubbed in the literature as the equivalent circle diameter and referred to in this paper as d_j . For two-phase alloys, the cross-section area of the sample is recalculated in proportion to the volumetric content of the analyzed phase. The computer methods of image analysis enabled to measure various dimensional characteristics of individual grains, including their area. Therefore, the mean grain area is now determined by simply averaging the areas of individual grains. This method is used in various model calculations [14–16]. In a number of works, the circle equivalent diame-

ter (d_{eq}) calculated based on the area of an individual grain or a mean chord (d_{ch}) [19] is taken as the size of an individual grain [6; 17; 18]. As the individual grain sizes are determined, their size distribution can be obtained, which provides more complete information about the grain composition of the material.

A number of papers compared grain sizes obtained by various methods. For spherical grains, the relationship between d_{eq} and d_{ch} was defined [9]. In [15], the values of L and d_j were independently determined by measurement for a number of WC–Co hardmetals. The d_j/L ratio varied from 1.10 to 1.40, the mean value being 1.15. In the same paper, as well as in [14; 16], the value of this ratio was determined on model structures. The crystals of various shapes were used to make arbitrary cross sections, on which random chords were drawn. Then the areas of these sections and the lengths of all chords were averaged, and the mean values were used to determine d_j , L and d_j/L . The resulting d_j/L values stood at 1.74 [15] and 1.35–1.75 [16].

These results differ significantly from the experimental data. The authors themselves [15] point out this discrepancy, but do not offer any explanation. A possible reason for this difference may be that the mean size of a random chord determined in the computer model for all grains may not coincide with the L value measured by the linear intercept method. According to the linear intercept method, the lines cannot intersect the grains twice (ISO 4499 2(2020)). To meet this requirement, in micrographs, coarse grains can “shadow” fine ones and the latter are not taken into account when the mean value is found. Therefore, the mean size of random chords determined for all grains may be smaller than the mean size of random chords on the lines, and the modeling will yield an overestimated value of the d_j/L ratio. This phenomenon of fine grains being “shadowed” will hereinafter be called a “shadow effect.” The shadow effect and its impact on the grain size measurements by the linear intercept method have not been addressed in the literature so far. As some researchers substitute the alloy grain size distribution for the distribu-

tion of random chords intercepted by secants, we will dwell on the relationship between these distributions.

The objective of this study is to measure the shadow effect; to determine whether the shadow effect depends on the nature of the WC grain size distributions; to assess the impact of the shadow effect on the mean WC grain size measured by the linear intercept method; to find correlation between the WC grain size distributions and the size distribution of random chords in the linear intercept method.

Measurement objects and methods

We compared the dimensional characteristics measured for all grains on the hardmetals cross sections and for the grains intersected by the line. The equivalent diameter d_{eq} , which is related to d_j , and the mean grain chord d_{ch} related to L were chosen as the dimensional characteristics of individual grains.

For the research, we selected 7 samples produced by Virial LTD (St. Petersburg), representing WC–Co hardmetals with 10 wt. % Co. The samples included alloys with narrow, wide and bimodal grain size distributions.

To identify the boundaries of the carbide phase grains, the samples were etched with Murakami solution. The microstructure of the samples was studied using a MIRA 3 scanning electron microscope (SEM) (Tescan, Czech Republic). We used the Fiji image processing software (USA) [20] and VideoTest – Structure 5.2 (Russia) to analyze SEM micrographs.

The built-in functions of these software packages enabled to measure the following grain dimensional characteristics:

1. Mean size of the intercept (random chord) L :

$$L = \frac{1}{n} \sum l_i,$$

where l_i is a random chord of the i^{th} grain intersected by the line.

Hereinafter, we will distinguish between two types of sizes: with the index “a” – the size taking into account all the grains in the micrograph; with the index “l” – the size taking into account only the grains intersected by the line.

2. Equivalent diameter $d_j^{a,l}$ (Jefferies method):

$$d_j^{a,l} = \sqrt{\frac{4}{\pi} \bar{A}},$$

where $\bar{A} = \sum \frac{A_i^{a,l}}{n}$, $A_i^{a,l}$ is the area of the i^{th} grain.

3. Mean equivalent diameter $d_{eq}^{a,l}$:

$$d_{eq}^{a,l} = \frac{1}{n} \sum d_{eq,i}^{a,l},$$

where $d_{eq,i}^{a,l} = \sqrt{\frac{4}{\pi} A_i^{a,l}}$ – is the equivalent diameter of an individual grain.

4. Mean chord $d_{ch}^{a,l}$:

$$d_{ch}^{a,l} = \frac{1}{n} \sum d_{ch,i}^{a,l},$$

where $d_{ch,i}^{a,l}$ (i stands for the grain number) is the mean grain chord determined as the mean value of all chords crossing the grain parallel to secants.

The total number of grains in micrographs for each alloy amounted to about 2000–3000 and the number of grains intersected by the line exceeded 1000. For each mean grain size, the standard deviation and variation coefficient (c_v) were determined.

Experimental results

Table 1 features the experimental results of measurements of the corresponding mean grain sizes with variation coefficients (c_v) of all the hardmetals under study.

Table 1 shows that in all cases the mean sizes of the grains intersected by the line are larger than the mean sizes of all measured grains of a given hardmetal. This manifestation of the shadow effect is attributed to the reduced share of the fine fraction and, accordingly, the increased share of the coarse fraction in the grain size distribution. Fig. 1, *a* shows a fragment of one of the images processed in Fiji for sample 2 – the shadow effect is clearly seen there. Fig. 1, *b* demonstrates changes in grain distributions by the equivalent diameter for sample 3 with a relatively narrow distribution due to the shadow effect. Similar results were obtained for the mean chord of individual grains. Thus, when the mean grain size is determined by the linear intercept method observing the standard requirement, the changed values of initial mean sizes and the entire grain size distribution are obtained.

To measure the shadow effect, we considered the ratio of the mean sizes of all grains to the mean sizes of the grains intersected by the lines d_{eq}^a/d_{eq}^l and d_{ch}^a/d_{ch}^l , as well as their dependence on the variation coefficients c_v . The experimental results are presented in Fig. 2. Since the monodisperse composi-

Table 1. Dimensional parameters measured for the WC–Co hardmetals under study
Таблица 1. Измеренные размерные параметры для исследуемых твердых сплавов WC–Co

Sample No.	d_{eq}^a/c_v	d_{eq}^l/c_v	L/c_v	d_{ch}^a/c_v	d_{ch}^l/c_v	d_J^a	d_J^l
	$\mu\text{m}/\text{rel. units}$					μm	
1	1.02/0.42	1.21/0.40	0.83/0.65	0.74/0.43	0.85/0.42	1.11	1.31
2	1.14/0.64	1.58/0.63	1.08/0.87	0.83/0.65	1.11/0.67	1.35	1.87
3	2.42/0.49	2.90/0.47	2.14/0.71	1.74/0.52	2.05/0.50	2.70	3.20
4	2.45/0.52	3.02/0.50	2.19/0.74	1.77/0.54	2.16/0.52	2.76	3.38
5	2.41/0.46	2.81/0.43	1.98/0.66	1.72/0.48	1.96/0.45	2.66	3.06
6	1.01/0.50	1.25/0.49	0.83/0.71	0.71/0.49	0.86/0.49	1.13	1.39
7	1.23/0.89	2.31/0.82	1.66/1.09	0.90/0.90	1.62/0.84	1.65	2.95

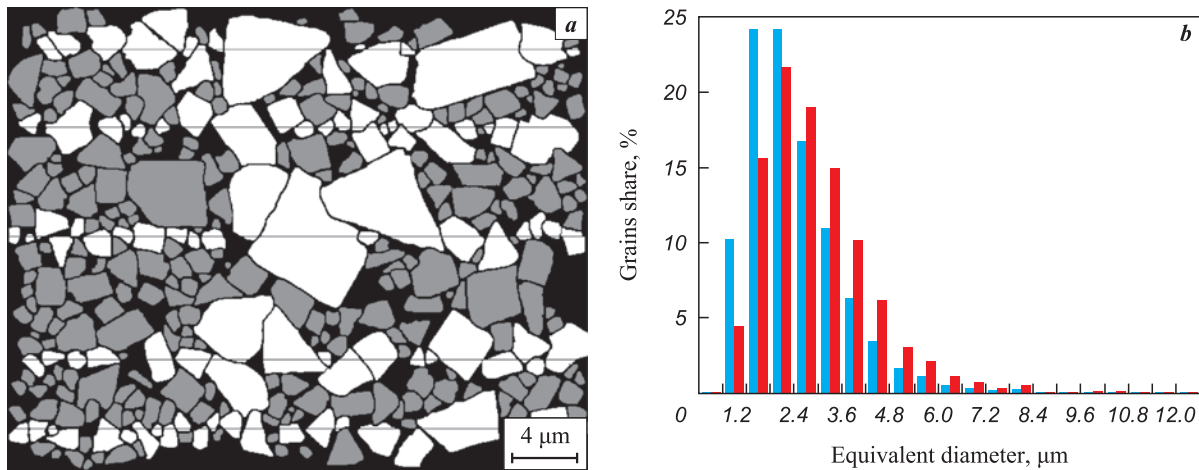


Fig. 1. Demonstration of the shadow effect using the example of a fragment of an image processed in “Fiji” for sample 2 (see Table 1) (a) and the equivalent grain diameter distribution for sample 3 with a relatively narrow distribution due to the shadow effect (b)

■ – experimental data for all grains; ■ – experimental data for the grains intersected by the lines

Рис. 1. Демонстрация теневого эффекта на примере фрагмента одного из обработанных в «Fiji» снимков для образца 2 (см. табл. 1) (a) и распределение зерен по величине эквивалентного диаметра для образца 3 с относительно узким распределением за счет теневого эффекта (b)

■ – экспериментальные данные для всех зерен; ■ – экспериментальные данные для зерен на секущих

tion does not provide for the shadow effect, the trend line was drawn through the point (0; 1). As can be seen from Fig. 2, the experimental data are well described by the equation

$$d^a/d^l = 1 - 0.08c_v - 0.60c_v^2 + 0.13c_v^3, \quad (1)$$

or

$$d^a/d^l = 1 - S, \quad (2)$$

where the shadow function

$$S = 0.08c_v + 0.60c_v^2 - 0.13c_v^3. \quad (3)$$

It is intuitively assumed that, with a sufficiently large number of grains intersected by the lines, the mean size

of such random chords (L) will be equal to the value of the mean chord for all grains (d_{ch}^a). The modeling procedure in [14–16] was based on this assumption, and it is valid in the absence of the shadow effect. However, due to the shadow effect, the size L should coincide with the mean chord value for the grains intersected by the line d_{ch}^l . Indeed, the ratio for all hardmetals was $L/d_{ch}^l = 1.00 \pm 0.03$. Accordingly, taking into account (2), we obtain

$$L = \frac{d_{ch}^a}{1 - S}. \quad (4)$$

When determining the dependence of d_{eq}^a/L on the shadow function S , the ratio between the mean values of d_{eq}^a and d_{ch}^a should be defined. The value

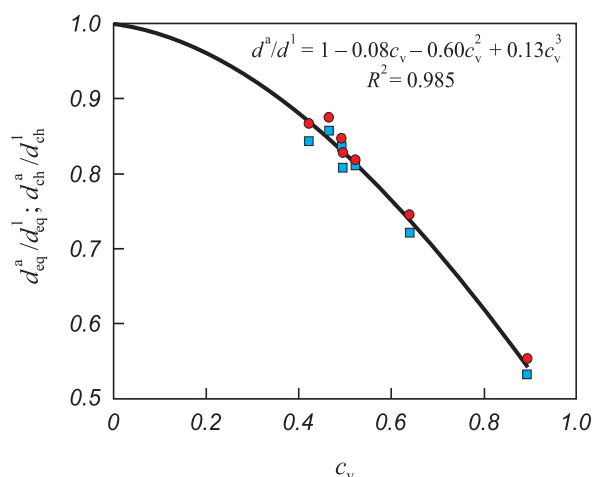


Fig. 2. Plots of d_{eq}^a/d_{eq}^l and d_{ch}^a/d_{ch}^l as function of c_v

Solid line – calculation based on the equation (1)

■ – experimental data for d_{eq}^a/d_{eq}^l

● – experimental data for d_{ch}^a/d_{ch}^l

Рис. 2. Зависимости d_{eq}^a/d_{eq}^l и d_{ch}^a/d_{ch}^l от c_v

Сплошная линия – расчет на основании уравнения (1)

■ – экспериментальные данные для d_{eq}^a/d_{eq}^l

● – экспериментальные данные для d_{ch}^a/d_{ch}^l

of the ratio $d_{eq}^{a,l}/d_{ch}^{a,l}$ does not depend on the type of alloy grain size distribution and is determined by the grain shape only. Hereinafter, this ratio will be called the shape coefficient K_s . For round grains, the diameter/mean chord ratio is $4/\pi \approx 1.27$. Taking into account averaging over orientations, for rectangular grains, the shape coefficient $K_s \approx 1.36$, for trapezoidal ones – $K_s \approx 1.39$, for triangular ones – $K_s = 1.60 \div 1.70$ depending on the triangle angles. For all the hardmetals under study, no matter what grains were taken for averaging (all grains or the ones intersected by the line), the ratio $d_{eq}^{a,l}/d_{ch}^{a,l} = 1.41 \pm 0.03$ was obtained. Therefore, taking into account the variety of cross-sectional grain shapes of WC–Co hardmetals, the value $K_s \approx 1.4$ seems quite realistic. Hereinafter, we will assume that

$$d_{eq}^{a,l} = 1.4d_{ch}^{a,l}. \quad (5)$$

Based on (4) and (5), we get the following function:

Table 2. Measured dimensional parameters ($\mu\text{m}/\text{rel. units}$) for narrow intervals d_{eq}^l for sample 3

Таблица 2. Измеренные размерные параметры (мкм/отн.ед.) для узких интервалов d_{eq}^l для образца 3

d_{eq}^a/c_v	d_{ch}^l/c_v	L/c_v
1.5/0.04	1.05/0.21	1.03/0.44
2.5/0.02	1.78/0.19	1.77/0.45
3.1/0.02	2.21/0.15	2.16/0.43

$$d_{eq}^a/L = 1.4(1 - S). \quad (6)$$

To expand the analyzed range of changes in the width of grain size distributions in the micrographs of sample 3, we selected the grains with individual sizes d_{eq}^l in three narrow intervals: 1.5 ± 0.06 , 2.5 ± 0.06 and $3.1 \pm 0.06 \mu\text{m}$ (analogue of the δ function) and measured the corresponding values of d_{ch}^l and L . Table 2 presents the results obtained for these narrow intervals.

Fig. 3 shows the experimental values of d_{eq}^a/L and $1.4d_{ch}^l/d_{ch}^l$ for the hardmetals under study depending on the width of the WC grain size distribution, as well as the calculated curve according to the equation (6). As can be seen from Fig. 3, the equation (6) presents a comprehensive description of the experimental data.

The relationship between the mean sizes d_J and d_{eq} can be derived from the equation

$$\sigma^2 = \sum \frac{(d_{eq,i} - d_{eq})^2}{n}, \text{ where } \sigma \text{ is the standard deviation}$$

for d_{eq} . Since $\sum \frac{d_{eq,i}^2}{n} = d_J^2$, we obtain $\sigma^2 = d_J^2 - d_{eq}^2$, or

$$d_J^{a,l} = d_{eq}^{a,l} \sqrt{1 + c_v^2}. \quad (7)$$

In this case, (6) and (7) yield the following equation:

$$d_J^a/L = 1.4(1 - S) \sqrt{1 + c_v^2}. \quad (8)$$

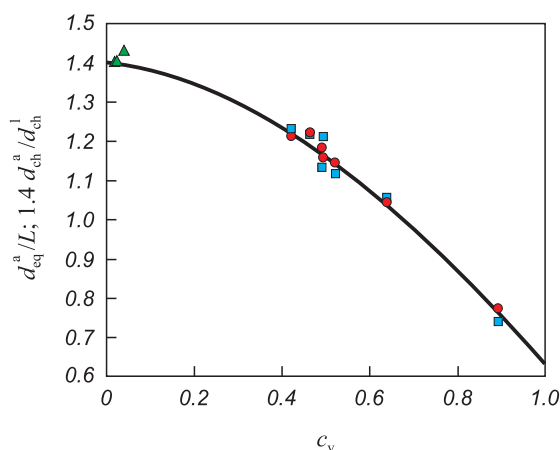


Fig. 3. Plots of d_{eq}^a/L and $1.4d_{ch}^l/d_{ch}^l$ as function of c_v

Solid line – calculation based on the equation (6)

■ – experimental data for d_{eq}^a/L

● – experimental data for $1.4d_{ch}^l/d_{ch}^l$

▲ – experimental data for d_{eq}^l/d_{ch}^l (narrow ranges)

Рис. 3. Зависимости d_{eq}^a/L и $1.4d_{ch}^l/d_{ch}^l$ от c_v

Сплошная линия – расчет на основании уравнения (6)

■ – экспериментальные данные для d_{eq}^a/L

● – экспериментальные данные для $1.4d_{ch}^l/d_{ch}^l$

▲ – экспериментальные данные для d_{eq}^l/d_{ch}^l (узкие диапазоны)

For hardmetals with a different predominant grain shape, equation (8) can be written in a more general form:

$$d_j^a/L = K_s(1-S)\sqrt{1+c_v^2}. \quad (9)$$

Fig. 4 shows the experimental values d_j^a/L and $1.4\sqrt{1+c_v^2}d_{ch}^a/d_{ch}^l$ for the hardmetals under study, as function of the width of the WC grain size distribution, as well as the calculated curve according to the equation (8).

As can be seen from Fig. 4, the equation (8) presents a satisfactory description of the experiment.

In [14–16], the computer modeling did not take the shadow effect into account and it was assumed that $L \approx d_{ch}^a$. In this case, the equation (8) becomes

$$(d_j^a/L)_{\text{model}} = 1.4\sqrt{1+c_v^2}. \quad (10)$$

Fig. 4 also shows the observed dependence of the d_j^a/d_{ch}^a ratio on c_v . It can be seen that the experimental values of d_j^a/d_{ch}^a and d_j^l/d_{ch}^l are close to the calculation results [15; 16].

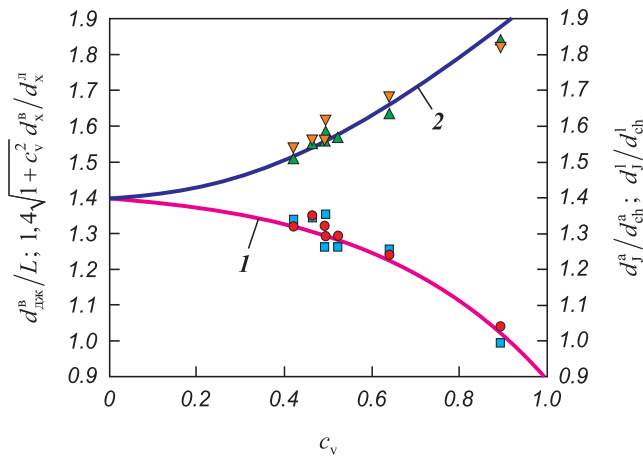


Fig. 4. Plots of d_j^a/L , $1.4\sqrt{1+c_v^2}d_{ch}^a/d_{ch}^l$, $d_j^{a,l}/d_{ch}^{a,l}$ as function of c_v

- 1 – calculation based on the equation (8)
- 2 – calculation based on the equation (10)
- – experimental data for d_j^a/L
- – experimental data for $1.4\sqrt{1+c_v^2}d_{ch}^a/d_{ch}^l$
- ▲ – experimental data for d_j^a/d_{ch}^a
- ▼ – experimental data for d_j^l/d_{ch}^l

Рис. 4. Зависимости $d_{дж}^a/L$, $1,4\sqrt{1+c_v^2}d_{х}^a/d_{х}^l$, $d_{дж}^{a,l}/d_{х}^{a,l}$ от c_v

- 1 – расчет на основании уравнения (8)
- 2 – расчет на основании уравнения (10)
- – экспериментальные данные для $d_{дж}^a/L$
- – экспериментальные данные для $1,4\sqrt{1+c_v^2}d_{х}^a/d_{х}^l$
- ▲ – экспериментальные данные для $d_{дж}^a/d_{х}^a$
- ▼ – экспериментальные данные для $d_{дж}^l/d_{х}^l$

In addition to the mean grain size, an important parameter of the microstructure is the WC grain size distribution. As can be seen from Table 1, the variation coefficients of the alloy grain distributions by the equivalent diameters and by mean chords are quite close (difference within 2–3 %). The grain distribution by the mean chord is slightly wider due to the grain shape. In addition, the grain distribution by the mean chords d_{ch}^a was compared to that by the value of $d_{eq}^a/1.4$ (normalization by the factor of 1.4 enables to superimpose the distributions on each other). Superposition showed that they coincide within the margin of error. Thus, the alloy grain size distribution by the values of d_{eq}^a and d_{ch}^a can equally characterize the alloy grain composition.

As noted above, the size distribution of random chords in the linear intercept method is often used as a characteristic of the alloy grain composition. However, it is necessary to take into account that, firstly, the distribution of random chords in the linear intercept method applies only to grains intersected by the lines, the distribution of which differs from that of all alloy grains due to the shadow effect. Secondly, even if the grains are of the same size and shape (δ -function), the random chords lengths are distributed in a certain way, the width of this distribution is not zero and is determined by the grain shape. For example, if the material consists of round grains of the same diameter d , the mean grain chords are also equal and, respectively, have a δ distribution. In this case, the size distribution density of random chords will be as follows $f(y) = \frac{y}{d}\sqrt{d^2-y^2}$, $y < d$, where d is the circle diameter [21] with the distribution width of $\sigma = 0.223d$. For grains of other shapes, taking possible orientations into account, the distribution function is more complex [22; 23]. Hereinafter, we will call such distribution functions the grain shape functions. Therefore, from a mathematical point of view, the random chord length distribution under the linear intercept method is a convolution of the size distribution function for the grains intersected by the lines and the grain shape function. In many areas of physics, a similar situation can be observed. When random chords distribution is analyzed, it is most logical to use the distribution of mean chords of the grains intersected by the lines as a function of the grain size distribution, while the distribution of random chords for a narrow interval in the distribution of mean chords of the alloy under study can be taken as a shape function. As an illustration, for sample 3 grains intersected by the line, the distributions of mean chords, random chords, and the computed distribution of random chords obtained

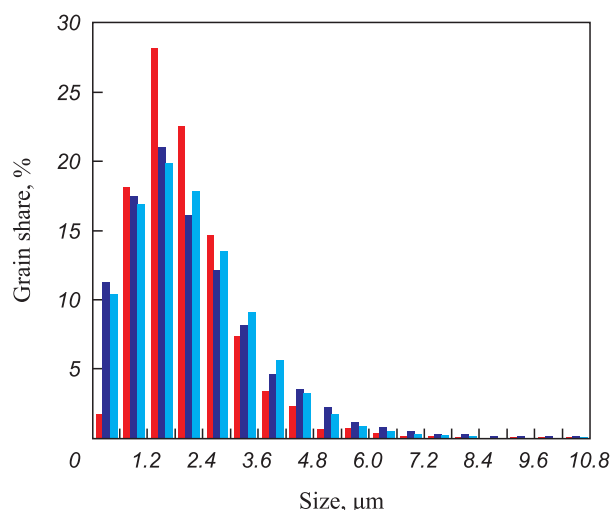


Fig. 5. Grain size distribution by the mean chords (■), random chords (■) and the convolution result (■) for sample 3

Рис. 5. Распределение зерен по величине средних хорд (■), случайных хорд (■) и результат свертки (■) для образца 3

by convolution were constructed. The results are shown in Fig. 5.

The comparison of the distribution functions of mean and random chords shows that with equal mean values, the distribution width of random chords is significantly higher (the variation coefficients of the distributions differ 1.4–1.5 times). At the same time, the distribution of random chords, within the margin of error, coincides with the computed distribution obtained by convolution. This means that even for the alloys with relatively narrow grain distributions, when the shadow effect is small, the distribution of random chords will not coincide with the alloy grain size distribution. According to Tikhonov [24], restoring the real function of alloy grain size distribution from the distribution of random chords is a complex task and should be viewed as an incorrect-posed problem.

Discussion of results

The discrepancies between the experimental and computed values of the d_j/L ratio in WC–Co hardmetals revealed in [14–16] indicated a number of problems associated with the linear intercept method. Although this method is widely used, numerous methodological works and a number of international standards are devoted to it, when it comes to WC–Co hardmetals, there is no clear understanding what size is being measured.

The linear intercept method, like the planimetric technique, was originally developed to estimate the mean grain size of polycrystalline metals and

alloys, which, as a rule, have rather narrow grain size distributions. Standard WC–Co hardmetals are characterized by a wider WC grain size distribution. This is probably the reason why, with almost similar measurement procedures, the standard for metals and alloys ASTM E112-13 (2021) and the standard for hardmetals ISO 4499 2 (2020) describe different correlations between the linear intercept and planimetric methods.

The ASTM standard indicates the ratio $L = \sqrt{\frac{\pi A}{4}}$, which is considered accurate for round grains and approximate for equiaxed grains of other shapes, which gives the equation $d_j^a/L \approx 1.273$, or $4/\pi$. As previously noted, this value is equal to the ratio of the circle diameter to its mean chord.

The ISO standard, with reference to [15], indicates the ratio $L = \sqrt{A}$, which gives the equation $d_j^a/L \approx 1.128$, or $\sqrt{4/\pi}$. In [15], the experimental values of the ratio d_j^a/L for different alloys varied from 1.10 to 1.40, the mean value being 1.15. Therefore, despite the wide scatter in results, the authors assumed the ratio d_j^a/L to be equal to 1.13 and indicated it in the standard. We believe that the spread in the d_j^a/L value obtained in [15], in addition to the measuring inaccuracy, is attributed to the fact that the alloys probably had different width of the WC grain size distribution, and simple averaging of the d_j^a/L measurement results for different alloys resulted in an error.

The dependence of the mean WC grain size determined by the linear intercept method on the width of the WC grain size distribution revealed in this work and explained by the shadow function S enables to eliminate this error. In addition, the opportunity is afforded, within a single approach, to harmonize the results of the linear intercept and planimetric methods in ASTM E112-13 (2021) and ISO 4499 2 (2020) standards. The ratio d_j^a/L depending on the grain shape and the width of the grain size distribution is given by the equation (9). For round and equiaxed grains, the shape coefficient K_s is approximately equal to 1.27, and for relatively narrow distributions ($c_v < 0.3$) the result from (9) corresponds to ASTM. For hardmetals, due to the variety of shapes of WC grains, the coefficient K_s is approximately equal to 1.4, and the width of the WC grain distribution can vary over a fairly wide range. Therefore, the value of the ratio d_j^a/L , according to (9), can vary from 1.0 to 1.4 depending on c_v . This spread of d_j^a/L values is fully consistent with the experimental results [15]. It confirms that simple averaging of d_j^a/L values for alloys with different c_v values is a mistake and so is the introduction of this mean value (1.128) into ISO 4499 2(2020) standard. Expressing dependence of d_j^a/L on c_v using

the equation (8), c_v varying from 0 to 1.0, we obtain an integral mean value of 1.244.

Thus, when the linear intercept method is used to determine the mean WC grain size in hardmetals, the mean size value obtained is even more arbitrary than the researchers, including the authors, earlier assumed. Therefore, this value must be used with caution when establishing a relationship between WC grain size and the physical properties of alloys. It is also important to keep in mind that the distribution of random chords by length in the linear intercept method is not the same as the alloy grain size distribution.

Conclusions

1. For a number of WC–Co hardmetals, having compared the dimensional characteristics of WC grains measured for all grains and for the ones intersected by the line, we proved that the condition for drawing these lines in the linear intercept method (ISO 4499 2) results in shadowing of finer grains by course ones and distortion of the WC grain size distribution (shadow effect).

2. It has been established that the shadow effect grows with the increasing variation coefficient (c_v) of the WC grain size distribution. The relationship between the mean sizes of all grains and the grains intersected by the line can be described using the shadow function S

$$d^a/d^l = 1 - S,$$

where $S = 0.08c_v + 0.60c_v^2 - 0.13c_v^3$.

3. For the hardmetals under study, the relationship between the mean equivalent diameter and the mean chord of WC grains was obtained by measurement:

$$d_{eq} \approx 1.4d_{ch}.$$

4. It is demonstrated that the relationship between the mean equivalent diameter, the Jefferies diameter and the mean grain size in the linear intercept method is not a constant value, it depends on the size of the shadow effect:

$$d_{eq}^a = 1.4L(1 - S),$$

$$d_j^a = 1.4L(1 - S)\sqrt{1 + c_v^2}.$$

5. Without taking the alloy grain size distribution into account, the linear intercept method can only give a conditional estimate of the mean size and these limitations of the method should be kept in mind.

6. The length distribution of random chords in the linear intercept method is not a characteristic of the WC grain size distribution.

References / Список литературы

1. Lee H.C., Gurland J. Hardness and deformation of cemented tungsten carbide. *Materials Science and Engineering: A*. 1978;33:125–133.
[https://doi.org/10.1016/0025-5416\(78\)90163-5](https://doi.org/10.1016/0025-5416(78)90163-5)
2. Roebuck B. Extrapolating hardness-structure property maps in WC/Co. *International Journal of Refractory Metals and Hard Materials*. 2006;24(1–2):101–108.
<https://doi.org/10.1016/j.ijrmhm.2005.04.021>
3. Vornberger A., Pötschke J., Gestrich T., Herrmann M., Michaelis A. Influence of microstructure on hardness and thermal conductivity of hardmetals. *International Journal of Refractory Metals and Hard Materials*. 2020;88: 105170. <https://doi.org/10.1016/j.ijrmhm.2019.105170>
4. Engqvist H., Uhrenius B. Determination of the average grain size of cemented carbides. *International Journal of Refractory Metals and Hard Materials*. 2003;21:31–35.
[https://doi.org/10.1016/S0263-4368\(03\)00005-2](https://doi.org/10.1016/S0263-4368(03)00005-2)
5. Pesin V.A., Osmakov A.S., Boykov S.Yu. Properties of WC–Co hardmetals as a function of their composition and microstructural parameters. *Powder Metallurgy and Functional Coatings*. 2022;16(3):37–44.
<https://doi.org/10.17073/1997-308X-2022-3-37-44>
Песин В.А., Осмаков А.С., Бойков С.Ю. Зависимость свойств твердых сплавов WC–Co от их состава и характеристик микроструктуры. *Известия вузов. Порошковая металлургия и функциональные покрытия*. 2022;16(3):37–44.
<https://doi.org/10.17073/1997-308X-2022-3-37-44>
6. Vasilyeva M.V., Pesin V.A., Osmakov A.S., Shamshurin A.I. Research of the depending of the hardness of WC–Co hardmetals on the nature of the distribution of WC grains by size. *Zavodskaya laboratoriya. Diagnostika materialov*. 2023;89(2(I)):45–49. (In Russ.).
<https://doi.org/10.26896/1028-6861-2023-89-2-I-45-49>
Васильева М.В., Песин В.А., Осмаков А.С., Шамшурин А.И. Исследование зависимости твердости сплавов WC–Co от характера распределения зерен WC по размерам. *Заводская лаборатория. Диагностика материалов*. 2023;89(2(I)):45–49.
<https://doi.org/10.26896/1028-6861-2023-89-2-I-45-49>
7. Heyn E. Short reports from the metallurgical and metallographical laboratory of the Royal Mechanical and Technical Testing Institute of Charlottenburg. *Metallographist*. 1903;5:37–64.
8. Bennet E.G., Roebuck B. The metallographic measurement of hardmetal grain size. *National Physical Laboratory*. 2000;(22):1–52.
9. Arkhangelskiy S.I., Levin D.M. Statistical analysis of the parameters and grain size distribution functions of single-phase polycrystalline materials. *Zavodskaya laboratoriya. Diagnostika materialov*. 2020;86(4):39–45. (In Russ.).
<https://doi.org/10.26896/1028-6861-2020-86-4-39-45>

- Архангельский С.И., Левин Д.М. Статистический анализ параметров и функций распределения по размерам зерен однофазных поликристаллических материалов. *Заводская лаборатория. Диагностика материалов*. 2020;86(4):39–45.
<https://doi.org/10.26896/1028-6861-2020-86-4-39-45>
10. Li D., Liu Y., Ye J., Chen X., Wang L. The enhancement of the microstructure and mechanical performances of ultrafine WC–Co cemented carbides by optimizing Cr₂(C,N) addition and WC particle sizes. *International Journal of Refractory Metals and Hard Materials*. 2021;97(1):105518.
<https://doi.org/10.1016/j.ijrmhm.2021.105518>
 11. Megret A., Vitry V., Delaunoy F. High-energy ball milling of WC–10Co: Effect of the milling medium and speed on the mechanical properties. *International Journal of Refractory Metals and Hard Materials*. 2021;104:105774.
<https://doi.org/10.1016/j.ijrmhm.2021.105774>
 12. Chen X., Liu Y., Ye J., Wang L., Li D. Effect of rapid cooling on microstructure and properties of nanocrystalline WC–9%Co–Cr₃C₂–VC cemented carbide. *International Journal of Refractory Metals and Hard Materials*. 2022;109:105961.
<https://doi.org/10.1016/j.ijrmhm.2022.105961>
 13. Jefferies Z., Kline A.H., Zimmer E.B. The determination of the average grain size in metals. *Transactions AIME*. 1916;54:594–607.
 14. Roebuck B. Measuring WC grain size distribution. *Metal Powder Report*. 1999;54(4):20–24.
[https://doi.org/10.1016/S0026-0657\(99\)80421-4](https://doi.org/10.1016/S0026-0657(99)80421-4)
 15. Roebuck B., Phatak C., Birks-Agnew I. A comparison of the linear intercept and equivalent circle methods for grain size measurement in WC/Co hardmetals. *NPL Report. MATC(A)*. 2004;149:1–34.
 16. Zeferino L.H., Buriti A.C., Monteiro S.N., da Silva A.G.P. Determination of the WC grain size in hardmetals using stereology – A critical analysis. *International Journal of Refractory Metals and Hard Materials*. 2008;26(4):367–371.
<https://doi.org/10.1016/J.IJRMHM.2007.08.011>
 17. Lu Z., Du J., Sun Y., Su G., Zhang C., Kong X. Effect of ultrafine WC contents on the microstructures, mechanical properties and wear resistances of regenerated coarse grained WC–10Co cemented carbides. *International Journal of Refractory Metals and Hard Materials*. 2021;97:105516.
<https://doi.org/10.1016/J.IJRMHM.2021.105516>
 18. Müller D., Konyashin I., Farag S., Ries B., Zaitsev A., Loginov P. WC coarsening in cemented carbides during sintering. Part I: The influence of WC grain size and grain size distribution. *International Journal of Refractory Metals and Hard Materials*. 2022;102:105714.
<https://doi.org/10.1016/j.ijrmhm.2021.105714>
 19. Pötschke J., Säuberlich T., Vornberger A., Meese-Marktscheffel J.A. Solid state sintered nanoscaled hardmetals and their properties. *International Journal of Refractory Metals and Hard Materials*. 2018;72:45–50.
<https://doi.org/10.1016/j.ijrmhm.2017.12.008>
 20. Tarrago J.M., Coureaux D., Torres Y., Wu F., Al-Dawery I.A., Llanes L. Implementation of an effective time-saving two-stage methodology for microstructural characterization of cemented carbides. *International Journal of Refractory Metals and Hard Materials*. 2016;55:80–86.
<https://doi.org/10.1016/J.IJRMHM.2015.10.006>
 21. Arkhangelskiy S.I., Borodikhin V.M. Connection between distributions of diameters of spherical particles and chords of their random sections. *Sibirskii zhurnal industrial'noi matematiki*. 2002;5(3):27–34. (In Russ.).
Архангельский С.И., Бородин В.М. Связь между распределениями диаметров сферических частиц и хорд их случайных сечений. *Сибирский журнал индустриальной математики*. 2002;5(3):27–34.
 22. Agaronyan N.G., Oganyan V.K. Chord length distribution functions for polygons. *Izvestiya NAN Armenii. Matematika*. 2005;40(4):42–57. (In Russ.).
Агаронян Н.Г., Оганян В.К. Функции распределения длины хорды для многоугольников. *Известия НАН Армении. Математика*. 2005;40(4):42–57.
 23. Arutyunyan G.S. Chord length distribution function for a regular hexagon. *Uchenye Zapiski EGU*. 2007;(1):17–24. (In Russ.).
Арутюнян Г.С. Функция распределения длины хорды для правильного шестиугольника. *Ученые записки ЕГУ*. 2007;(1):17–24.
 24. Tikhonov A.N., Arsenin V.Ya. Methods for solving ill-posed problems. Moscow: Nauka, 1986. 288 p. (In Russ.).
Тихонов А.Н., Арсенин В.Я. Методы решения некорректных задач. М.: Наука, 1986. 288с.

Information about the Authors

Vadim A. Pesin – Leading Expert at the testing laboratory No. 1, “Virial” Ltd.

 **ORCID:** 0000-0002-1250-173X

 **E-mail:** PesinVA@virial.ru

Mariya V. Vasilyeva – Engineer at the testing laboratory No. 1, “Virial” Ltd.

 **ORCID:** 0000-0002-4632-8816

 **E-mail:** VasilyevaMV@virial.ru


Andrey S. Osmakov – Cand. Sci. (Eng.), Head of the testing laboratory No. 1, “Virial” Ltd.

 **ORCID:** 0000-0002-8712-908X

 **E-mail:** OsmakovAS@virial.ru


Сведения об авторах

Вадим Абрамович Песин – вед. специалист испытательной лаборатории № 1, ООО «Вириал»

 **ORCID:** 0000-0002-1250-173X


 **E-mail:** PesinVA@virial.ru

Мария Владимировна Васильева – инженер испытательной лаборатории № 1, ООО «Вириал»

 **ORCID:** 0000-0002-4632-8816

 **E-mail:** VasilyevaMV@virial.ru

Андрей Сергеевич Осмаков – к.т.н., начальник испытательной лаборатории № 1, ООО «Вириал»

 **ORCID:** 0000-0002-8712-908X

 **E-mail:** OsmakovAS@virial.ru

Contribution of the Authors**Вклад авторов**

V. A. Pesin – formulating the main concept of the article, determining the purpose of the work, making calculations, writing the article.

M. V. Vasilyeva – making measurements and calculations, writing the article.

A. S. Osmakov – defining the tasks of the work, amending the manuscript, participating in the analysis and discussion of the results.

В. А. Песин – формирование основной концепции статьи, определение цели работы, проведение расчетов, написание статьи.

М. В. Васильева – проведение измерений и расчетов, написание статьи.

А. С. Осмаков – определение задачи работы, корректировка текста статьи, участие в анализе и обсуждении результатов.

Received 18.01.2023

Revised 07.04.2023

Accepted 11.04.2023

Статья поступила 18.01.2023 г.

Доработана 07.04.2023 г.

Принята к публикации 11.04.2023 г.



UDC 621-033.6 : 669.018.9; 621-033.6 : 666.1/.7; 621-033.6 : 666.1

<https://doi.org/10.17073/1997-308X-2024-3-38-48>

Research article

Научная статья



Self-propagating high-temperature synthesis and spark plasma sintering of high-entropy (Hf,Ta,Nb)(C,N) carbonitride

V. S. Suvorova[✉], A. A. Nepapushev, D. S. Suvorov,

K. V. Kuskov, D. O. Moskovskikh

National University of Science and Technology “MISIS”

4 Bld 1 Leninskiy Prosp., Moscow 119049, Russia

✉ buynevich.vs@misys.ru

Abstract. In this research, we combined mechanical activation (MA), self-propagating high-temperature synthesis (SHS), and spark plasma sintering (SPS) methods to obtain a dense high-entropy (Hf,Ta,Nb)(C,N) carbonitride and studied its properties. To implement the SHS process, a mixture of initial metals and carbon was subjected to pre-treatment in a planetary mill in the low-energy mode, in which the jar rotation speed reached 350 rpm. We studied the evolution of microstructure and phase composition during the MA process. It has been established that after 60 min of treatment, Hf/Ta/Nb/C layered composite particles consisting of Hf, Ta, Nb and C submicron layers, with an average size of about 15 μm , were formed. However, according to the X-ray diffraction analysis, the components in the jar did not interact. SHS of Hf/Ta/Nb/C reactive mixtures was performed in a nitrogen atmosphere ($P = 0.8 \text{ MPa}$); after synthesis, two isomorphous (Hf,Ta,Nb)(C,N) phases of the $Fm-3m$ (225) space group with lattice parameters of $a = 0.4476 \text{ nm}$ (71 wt. %) and $a = 0.4469 \text{ nm}$ (22 wt. %) were revealed in the powder. After SHS, the average size of agglomerates was 10 μm and their morphology resembled that of composite particles after MA. The agglomerates formed during SHS consisted of pores and round-shaped particles ranging in size from 0.5 to 2 μm , which was caused by the melting of metal components in the combustion zone and rapid crystallization of product grains from the melt, followed by subsequent recrystallization. Spark plasma sintering at a temperature of 2000 $^{\circ}\text{C}$, a pressure of 50 MPa and a holding time of 20 min enabled to obtain a single-phase high-entropy $(\text{Hf}_{0.33}\text{Ta}_{0.33}\text{Nb}_{0.33})\text{C}_{0.5}\text{N}_{0.3}$ material with a lattice parameter of 0.4482 nm characterized by a high relative density of 98 %, a hardness of $21.5 \pm 0.4 \text{ GPa}$, a Young's modulus of $458 \pm 10 \text{ GPa}$, and a fracture toughness value of $3.7 \pm 0.3 \text{ MPa}\cdot\text{m}^{1/2}$.

Keywords: high-entropy ceramics, high-entropy carbonitride, mechanical activation, self-propagating high-temperature synthesis, ceramics, spark plasma sintering

Acknowledgements: This work was supported by the Russian Science Foundation grant No. 19-79-10280П.

For citation: Suvorova V.S., Nepapushev A.A., Suvorov D.S., Kuskov K.V., Moskovskikh D.O. Self-propagating high-temperature synthesis and spark plasma sintering of high-entropy (Hf,Ta,Nb)(C,N) carbonitride. *Powder Metallurgy and Functional Coatings*. 2024;18(3):38–48. <https://doi.org/10.17073/1997-308X-2024-3-38-48>

Самораспространяющийся высокотемпературный синтез и искровое плазменное спекание высокоэнтروпийного карбонитрида (Hf,Ta,Nb)(C,N)

В. С. Суворова[✉], А. А. Непапшев, Д. С. Суворов,
К. В. Кусков, Д. О. Московских

Национальный исследовательский технологический университет «МИСИС»
Россия, 119049, г. Москва, Ленинский пр-т, 4, стр. 1

✉ buynevich.vs@misys.ru

Аннотация. В работе комбинацией методов механического активирования (МА), самораспространяющегося высокотемпературного синтеза (СВС) и искрового плазменного спекания (ИПС) получен плотный высокоэнтропийный карбонитрид (Hf,Ta,Nb)(C,N) и исследованы его свойства. Для реализации процесса СВС смесь исходных металлов с углеродом подвергали предварительной обработке в планетарной мельнице в низкоэнергетическом режиме, при котором скорость вращения барабанов составляла 350 об/мин. Была исследована эволюция микроструктуры и фазового состава в процессе МА. Установлено, что после обработки в течение 60 мин происходит формирование слоистых композиционных частиц Hf/Ta/Nb/C, имеющих средний размер порядка 15 мкм и состоящих из субмикронных слоев Hf, Ta, Nb и C. При этом, согласно данным рентгенофазового анализа, взаимодействия компонентов в барабане не происходило. СВС реакционных смесей Hf/Ta/Nb/C проводили в атмосфере азота ($P = 0,8$ МПа), после синтеза в порошке были обнаружены две изоморфные фазы (Hf,Ta,Nb)(C,N) пространственной группы $Fm-3m$ (225) с различными параметрами решетки: $a = 0,4476$ нм (71 мас. %) и $a = 0,4469$ нм (22 мас. %). Морфология частиц после СВС повторяла морфологию композиционных частиц после МА, средний размер агломератов составлял 10 мкм. Сформировавшиеся в процессе СВС агломераты состояли из частиц округлой формы размером от 0,5 до 2 мкм и пор, что обусловлено плавлением металлических компонентов в зоне горения, быстрой кристаллизацией зерен продукта из расплава и их последующей рекристаллизацией. Процесс ИПС при температуре 2000 °С, давлении прессования 50 МПа и времени выдержки 20 мин позволил получить однофазный высокоэнтропийный материал $(\text{Hf}_{0,33}\text{Ta}_{0,33}\text{Nb}_{0,33})\text{C}_{0,5}\text{N}_{0,5}$ с параметром решетки 0,4482 нм, который характеризовался высокой относительной плотностью 98 %, твердостью $21,5 \pm 0,4$ ГПа, модулем Юнга 458 ± 10 ГПа и значением трещиностойкости $3,7 \pm 0,3$ МПа·м^{1/2}.

Ключевые слова: высокоэнтропийная керамика, высокоэнтропийный карбонитрид, механическое активирование, самораспространяющийся высокотемпературный синтез, керамика, искровое плазменное спекание

Благодарности: Работа выполнена при финансовой поддержке гранта РФФИ № 19-79-10280П.

Для цитирования: Суворова В.С., Непапшев А.А., Суворов Д.С., Кусков К.В., Московских Д.О. Самораспространяющийся высокотемпературный синтез и искровое плазменное спекание высокоэнтропийного карбонитрида (Hf,Ta,Nb)(C,N). *Известия вузов. Порошковая металлургия и функциональные покрытия*. 2024;18(3):38–48.
<https://doi.org/10.17073/1997-308X-2024-3-38-48>

Introduction

The development of pioneer industries poses a challenge for researchers to find new materials with high mechanical properties that can withstand high temperatures. In recent years, scientists have focused on high-entropy ceramics (HECs) with a configurational entropy of mixing $S_{\text{mix}} \geq 1/61R$ [1]. Unlike high-entropy alloys [2], HECs contain cations or anions sublattices [3], which gives this class of materials a wide structural diversity and controllable properties.

Among HECs, the compounds based on transition metals, IVB (Ti, Zr, Hf) and VB (V, Nb, Ta) groups of the periodic table, which have higher properties in comparison, for example, with binary carbides and nitrides, are most suitable for high-temperature appli-

cations. For example, the authors of [4] used spark plasma sintering (SPS) of a mixture of TaC, ZrC and NbC powders to synthesize single-phase (Ta,Zr,Nb)C carbide with high flexural strength at elevated temperatures (1600–2000 °C). In [5], high-entropy (HfTaZrTi)C and (HfTaZrNb)C carbides revealed a significantly enhanced hardness (36.1 ± 1.6 GPa) compared to HfC (31.5 ± 1.3 GPa) and (Hf,Ta)C (32.9 ± 1.8 GPa).

High-entropy carbonitride ceramics is also of importance for fundamental research and practical applications. A number of studies have shown that carbide sublattice nitrogen doping contributes to improving properties, including mechanical ones, as strong $Me-(C,N)$ covalent bonds and the $C \equiv N$ triple bond [6–8] are formed. The study [9] demonstrated

that the introduction of an additional metal component into the initial Ti–Zr–Hf–C–N system helps to increase the configuration entropy and, as a consequence, to enhance mechanical properties. As a result, extremely high fracture toughness ($8.4 \text{ MPa}\cdot\text{m}^{1/2}$) was reached in a five-component carbonitride $(\text{Ti}_{0.2}\text{Zr}_{0.2}\text{Hf}_{0.2}\text{Nb}_{0.2}\text{Ta}_{0.2})(\text{C}_{0.5}\text{N}_{0.5})$.

Previously, the authors of this paper obtained a double carbonitride in the Ta–Hf–C–N system, which demonstrated excellent mechanical properties and oxidation resistance [10; 11]. The introduction of an additional metal component Nb in the equiatomic ratio is expected to improve the mechanical properties of tantalum-hafnium carbonitride $(\text{Ta}_{0.5}\text{Hf}_{0.5})(\text{C},\text{N})$.

Dense high-entropy carbonitrides are commonly prepared by sintering a mixture of transition metal carbides and nitrides [12–14]. However, this method requires elevated temperatures and long exposures to complete the diffusion processes. The self-propagating high-temperature synthesis (SHS) method enables to significantly reduce the time for obtaining powder of complex multicomponent compounds. The subsequent spark plasma sintering pushes down energy costs for the fabrication of dense ceramics.

In this regard, the objective of this study was to obtain high-density $(\text{Hf},\text{Ta},\text{Nb})(\text{C},\text{N})$ carbonitride by combining the methods of mechanical activation (MA), self-propagating high-temperature synthesis and spark plasma sintering, and to investigate the mechanical properties of the resulting material.

Materials and methods

The precursors were hafnium powders GFM-1 (98.8 %, $\leq 180 \mu\text{m}$), tantalum TaP-1 (99.9 %, from 40 to 60 μm), niobium NbP-1a (99.9 %, from 40 to 63 μm) and carbon black P804T (99.5 %, $\leq 0.2 \mu\text{m}$). Before SHS, the Hf + Ta + Nb + C powder mixture was subjected to MA in a high-energy planetary ball mill “Activator-2S” (CJSC Activator, Russia) in an atmosphere of high purity argon (99.998 %): the ratio of the balls to powder mass was 20:1 (360 g : 18 g), gas pressure inside the cylinders stood at 0.6 MPa, and rotation speed was 350 rpm. To study the evolution of the phase composition and microstructure, the powder was removed from the jar after MA conducted for 5, 30, 45 and 60 min.

SHS was performed in the constant pressure reactor in a nitrogen atmosphere (grade 1, 99.999 %). The reactor chamber was pre-evacuated, then nitrogen was pumped until P reached 0.8 MPa. The self-sustaining exothermic reaction was initiated by briefly applying voltage to the tungsten coil connected to the power source.

SHS powders were consolidated by spark plasma sintering using a Labox 650 unit (SinterLand, Japan) in an argon atmosphere at a temperature of 2000 °C, pressure of 50 MPa, and a holding time of 20 min. The temperature was raised to the given value at a rate of 100 °C/min.

The samples microstructure, as well as their elemental composition, was studied using a JEOL JSM7600F scanning electron microscope (SEM) (JEOL Ltd., Japan) equipped with an X-MAX 80 mm² X-ray microanalysis system (Oxford Instruments, UK), at an accelerating voltage of 15 kV. The sizes of particles after MA and SHS were analyzed on a Bettersizer ST analyzer (Bettersize Instruments LTD, China) with wet dispersion.

The phase composition was studied using the X-ray diffraction analysis (XRD) on a Dron-4-07 diffractometer (JSC Research Center Burevestnik, Russia) with CuK_α radiation in the step scanning mode (scanning step 0.1°), the angles ranging from 20 to 80° with 2 s exposure. The ICDD PDF databases were used to analyze the resulting spectra. The Rietveld method was applied to calculate the lattice parameters and to conduct the quantitative phase analysis.

A TC-600 (Leco, USA) instrument estimated the amount of nitrogen and oxygen in the compounds by IR adsorption (for oxygen) and thermal conductivity (for nitrogen) analysis during the reduction melting of the samples in a resistance furnace in a helium flow. A CS-600 (Leco) instrument was used to measure the carbon content. For this purpose, the samples were subjected to oxidative melting in an induction furnace and the amount of CO_2 released was measured by IR absorption. The mass content of iron was determined by atomic emission spectral analysis on an iCAP 6000 echelle spectrometer (Thermo Fisher, USA).

The configurational entropy of mixing S_{mix} of a covalently bound compound was calculated using the formula [15]:

$$S_{\text{mix}} = -R \left[\left(\sum_{i=1}^N x_i \ln x_i \right)_{\text{cationic}} + \left(\sum_{j=1}^N x_j \ln x_j \right)_{\text{anionic}} \right],$$

where R is the universal gas constant, x_i and x_j are the mole fractions of cationic and anionic elements, respectively.

The relative density of samples after SPS was calculated as the ratio of hydrostatic to pycnometric density. The hydrostatic density of the samples was determined by hydrostatic weighing under GOST 20018-74 [16]. Pycnometric density was mea-

sured using a Ultrapycnometer 1000 helium pycnometer (Quantachrome Instruments, USA).

A Micro-Hardness Tester (CSM Instruments, Switzerland) was used to measure Young's modulus (E) at a 100 mN applied load.

We used a Durascan 70 hardness testing machine (Struers ApS, Denmark) to estimate hardness (HV) by the Vickers method, GOST 2999-75 [17]. A load of 30 N was applied for 10 s. At least 10 measurements were taken with each sample. We used the Anstis equation to assess the fracture toughness (K_{Ic}) [18].

Results and discussion

Before conducting SHS, the powder mixture consisting of Hf, Ta, Nb and C was subjected to mechanical activation to enhance its reactivity by reducing the particle size, accumulating defects and forming layered composite particles throughout the entire volume of the powder. The large contact area between the components of the mixture in composite particles facilitates and significantly accelerates the diffusion interaction between them during the SHS process [19].

Fig. 1 shows X -ray diffraction patterns of the Hf + Ta + Nb + C reaction mixture after mechanical activations (MA) of different durations in a planetary ball mill. After the 5 min MA, the X -ray diffraction pattern features peaks of individual elements: Nb and Ta of $Im-3m$ (229) space group, as well as hexagonal Hf ($P6_3/mmc$ (194)). Peaks of carbon black (C) are not identified due to its X -ray amorphism.

As the MA duration increases, the peaks widen and their intensity significantly decreases as the components crystal lattices deform during mechanical processing. After the 60 min MA, the phase composition remains unchanged, the X -ray diffraction pattern still shows diffraction peaks of the mixture metal components, while the reaction products, which lead to a drop in the accumulated energy and, consequently, reduced reactivity of the mixture, are not formed.

The evolution of the structure of the Hf + Ta + Nb + C reaction mixture during MA was studied using scanning electron microscopy (SEM) and X -ray microanalysis (XRMA) (Fig. 2). The non-activated powder mixture mostly consists of polygonal Hf, Ta and Nb particles ranging in size from 10 to 160 μm , as well as carbon black C agglomerates (Fig. 2, *a*). At the start of mechanical activation in the low-energy mode (from 0 to 30 min, Fig. 2, *b, c*), the mixture particles are crushed and flattened, new surfaces without oxide films or other impurities are formed, the contact area between Hf, Ta, Nb and C increases. The flattened particles interact with each other with their atomically

pure surfaces; as a result, after $\tau_{MA} = 30$ min, the first layered composite particles are formed (Fig. 2, *c*). With longer mechanical activation (Fig. 2, *d, e*), the content of particles of initial components in the reaction mixture drops, the composite particles crush into smaller ones and the thickness of the Hf, Ta, Nb and C layers decreases. After $\tau_{MA} = 60$ min (Fig. 2, *e*), the Hf/Ta/Nb/C layered composite particles are formed throughout the entire volume of the reaction mixture. The size of composite particles varies from 1 to 40 μm , the average size is 13 μm . Although mechanical activation was carried out in steel jars with steel grinding balls for 60 min, the content of iron and chromium does not exceed 0.5 and 0.05 wt. %, respectively, which is attributed to the use of low-energy mode (350 rpm) and the presence of a "lubricant" in the form of carbon black, which prevents grinding [20].

Thus, mechanical activation for 60 min in the low-energy mode contributes to the formation of Hf/Ta/Nb/C layered composite particles throughout the entire volume of the powder, however, reaction products inside the jars, which reduce the mixture reactivity, are not formed.

Fig. 3 shows an X -ray diffraction pattern of the powder after treatment in the mill for 60 min and subsequent

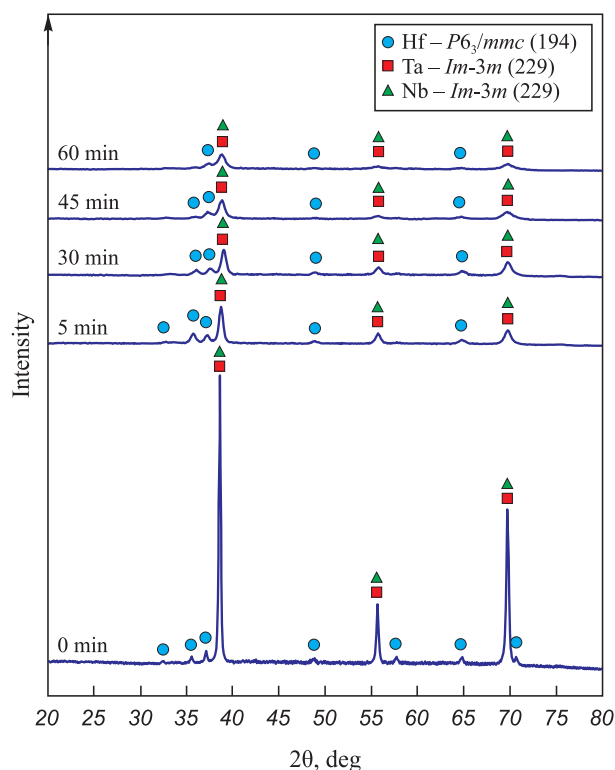


Fig. 1. The X -ray diffraction patterns of the Hf + Ta + Nb + C reactive mixture after MA of different durations

Рис. 1. Дифрактограммы реакционной смеси Hf + Ta + Nb + C после различного времени МА

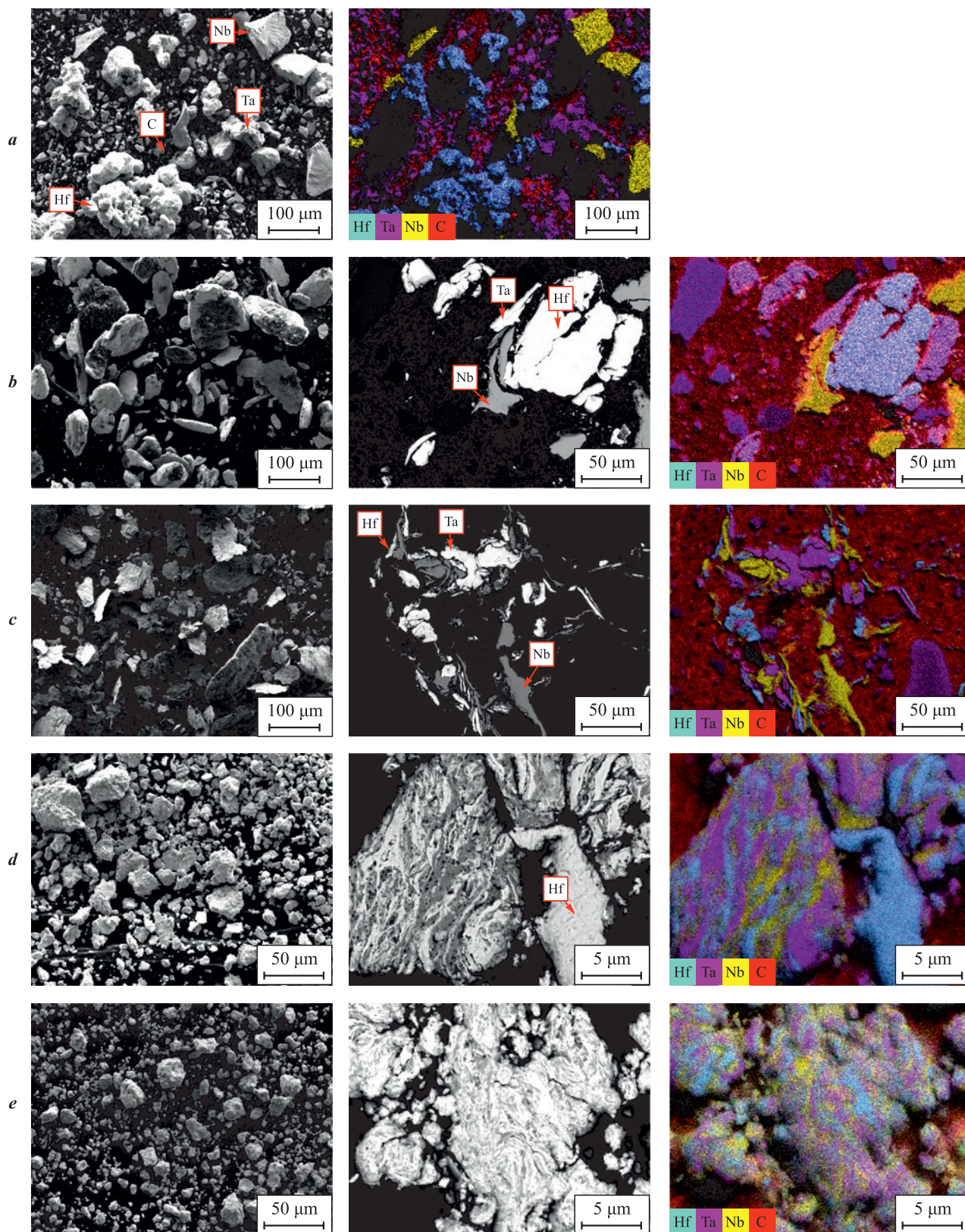


Fig. 2. The morphology, cross-section microstructures and element distribution maps of the Hf + Ta + Nb + C reactive mixture after MA of different durations

τ_{MA} , min: *a* – 0, *b* – 5, *c* – 30, *d* – 45, *e* – 60

Рис. 2. Морфология, микроstructures поперечных сечений и карты распределения элементов реакционной смеси Hf + Ta + Nb + C после различного времени МА

τ_{MA} , мин: *a* – 0, *b* – 5, *c* – 30, *d* – 45, *e* – 60

SHS in a nitrogen atmosphere ($P = 0.8$ MPa). We can see that after synthesis, the phase composition fundamentally changes compared to the powder after MA; the X -ray diffraction pattern features widened and asymmetric peaks due to the formation of two isomorphous phases (Hf,Ta,Nb)(C,N) of the $Fm-3m$ (225) space group with different lattice parameters – 0.4476 nm (71 wt. %) and 0.4469 nm (22 wt. %).

During filtration combustion of layered composite particles in nitrogen, the first step involves the formation of the nonstoichiometric carbide [19], which propagates at a very high speed, therefore, interaction with nitrogen occurs in the aftercombustion zone only [21]. High cooling rates lead to uneven nitriding throughout the sample volume, resulting in the formation of phases with different N contents [26]. The X -ray diffraction pattern also reveals low-intensity peaks of orthorhombic and monoclinic HfO_2 – based on the calculations by the Rietveld method, their content in the powder after SHS is 4 and 3 wt. %, respectively.

After SHS, the morphology of the product agglomerates (Fig. 4, *a*) predictably repeats the morphology of the composite particles after MA (Fig. 2, *e*), the average size of the agglomerates being ~ 30 μm . The extensive contact surfaces between the reagents in layered composite particles contributed to a signifi-

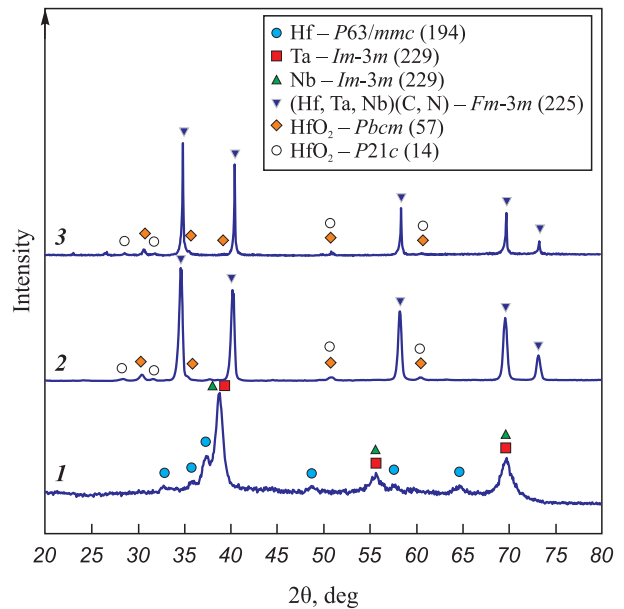


Fig. 3. X -ray diffraction patterns of the reaction mixture after 60 min MA (1), (Hf,Ta,Nb)(C,N) after SHS (2) and SPS (3)

Рис. 3. Дифрактограммы реакционной смеси после МА в течение 60 мин (1), (Hf,Ta,Nb)(C,N) после CBC (2) и ИПС (3)

cant acceleration of the diffusion interaction between them during the combustion process, as a result the morphology of the particles remained practically unchanged [22; 23].

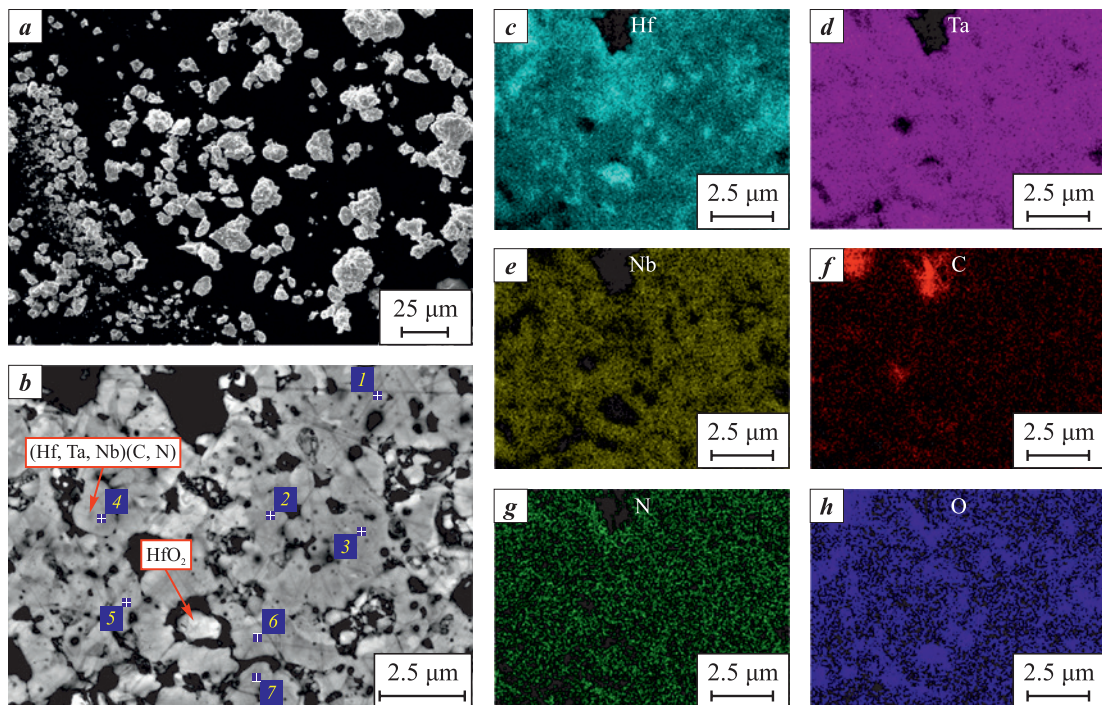


Fig. 4. Morphology of the (Hf,Ta,Nb)(C,N) agglomerates after SHS (*a*), cross-section microstructure (*b*), maps of the elements distribution in the agglomerate (*c-h*)

Рис. 4. Морфология агломератов (Hf,Ta,Nb)(C,N) после CBC (*a*), микроструктура поперечного сечения (*b*), карты распределения элементов в агломерате (*c-h*)

Table 1. X-ray microanalysis of the (Hf,Ta,Nb)(C,N) cross-section after SHS (at. %)

Таблица 1. Микрорентгеноспектральный анализ поперечного сечения (Hf,Ta,Nb)(C,N) после СВС (ат. %)

Spectrum number	Hf	Ta	Nb	C	N	O	Σ
1	14.8	14.3	14.3	40.2	12.9	3.5	100.0
2	13.1	13.9	13.5	52.5	1.9	5.1	100.0
3	14.8	14.4	15.1	47.9	3.2	4.6	100.0
4	13.7	14.9	14.6	48.9	4.1	3.8	100.0
5	13.7	13.8	13.9	48.3	4.6	5.7	100.0
6	12.5	12.9	13.1	51.8	5.2	4.5	100.0
7	14.8	14.5	14.9	43.7	6.9	5.2	100.0

When examining the cross section of the agglomerate (Fig. 4, *b*), we can see pores and rounded particles ranging in size from 0.5 to 2 μm . According to EDS (Fig. 4, *c–g*, Table 1), in the product (Hf,Ta,Nb)(C,N) (gray areas), the elements Hf, Ta, Nb and C are uniformly distributed, the nitrogen content in the particles fluctuating from 2 to 13 at. %. In addition to the main phase, HfO_2 inclusions (light gray areas in Fig. 4, *b, c, h*) are observed in the agglomerates.

As with the Hf–C–N [24], Ta–Hf–C–N [11] and Hf–Zr–C–N systems, the rounded particles are formed [25; 26] due to melting of the mixture metal components in the reaction zone, rapid crystallization of product grains from the melt and their subsequent recrystallization [27; 28]. The agglomerates structure after SHS is porous as gas releases during the combustion process.

Spark plasma sintering was performed in the mode previously tested on the Ta–Hf–C–N system [10; 11]. The X-ray diffraction pattern of sintered (Hf,Ta,Nb)(C,N) carbonitride is shown in Fig. 3. When exposed to high temperature, the carbonitride peaks became narrower and more symmetrical, suggesting homogenization of the chemical composition, ordering of the crystal structure and an increased size of crystallites after sintering; the lattice parameter value after SPS was 0.4482 nm. Compared to the powder after SHS, the content of orthorhombic and monoclinic HfO_2 increased to 7 and 5 wt. %.

A typical microstructure of (Hf,Ta,Nb)(C,N) carbonitride after SPS, as well as an elements distribution map are shown in Fig. 5. The particle size of the main phase (Hf,Ta,Nb)(C,N) (gray areas) varies from 2 to 15 μm . According to EDS (Fig. 5, *b–f*), the elements Hf, Ta, Nb, C and N are uniformly distributed. However, the structure of the bulk material features HfO_2 inclusions (light areas, Fig. 5, *a, b, g*) along the boundaries of the main phase, which confirms the X-ray diffraction data. The pycnometric density of the bulk carbonitride amounted to $11.06 \pm 0.05 \text{ g/cm}^3$, the hydrostatic density was $10.8 \pm 0.2 \text{ g/cm}^3$, which, in turn, corres-

ponds to 98 % of the relative density and is consistent with the microstructural analysis data.

Based on the results of chemical analysis, it can be concluded that the carbon content in the (Hf,Ta,Nb)(C,N)

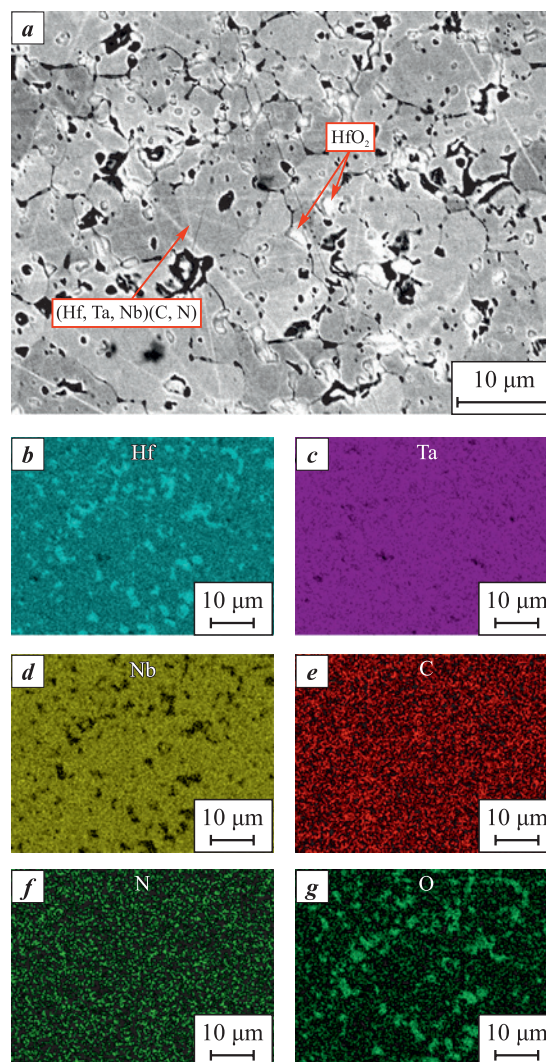


Fig. 5. (Hf,Ta,Nb)(C,N) microstructure (*a*) and elements distribution map after SPS (*b–g*)

Рис. 5. Микроструктура (Hf,Ta,Nb)(C,N) (*a*) и карты распределения элементов после ИПС (*b–g*)

Table 2. The mechanical properties of high-entropy (Hf,Ta,Nb)(C,N) carbonitride and similar materials

Таблица 2. Механические свойства высокоэнтروпийного карбонитрида (Hf,Ta,Nb)(C,N) и аналогичных материалов

Sample	ρ , %	HV , GPa	E , GPa	K_{Ic} , MPa·m ^{1/2}
(Hf,Ta,Nb)(C,N)	98.0 ± 0.5	21.5 ± 0.4	458 ± 10	3.7 ± 0.3
(Ta _{0.5} Hf _{0.5})C _{0.51} N _{0.4} [11]	98.0	18.7 ± 0.1	516	–
(Ti,V,Nb,Ta)(C _{0.7} N _{0.3}) [31]	95.6	19.1	437.5	2.0
(Hf _{0.2} Zr _{0.2} Ta _{0.2} Nb _{0.2} Ti _{0.2})(N _{0.5} C _{0.5}) [32]	95.9	19.5 ± 0.3	429 ± 10	2.8 ± 0.3
(Ti _{0.33} Zr _{0.33} Hf _{0.33})(C _{0.5} N _{0.5}) [9]	–	~16.0	~460	5.7
(Ti _{0.25} Zr _{0.25} Hf _{0.25} Nb _{0.25})(C _{0.5} N _{0.5}) [9]	–	~18.0	~450 ± 140	6.9
(Ti _{0.2} Zr _{0.2} Hf _{0.2} Nb _{0.2} Ta _{0.2})(C _{0.5} N _{0.5}) [9]	–	~21.0	~460	8.4
(NbTaZr)C [33]	99.5	20.24 ± 0.87	505	3.07
(Zr _{0.25} Nb _{0.25} Ti _{0.25} V _{0.25})C [34]	95.1	19.1 ± 0.5	460.4 ± 19.3	4.7 ± 0.5
(Hf _{0.2} Zr _{0.2} Ta _{0.2} Nb _{0.2} Ti _{0.2})C [35]	93.0	15.0	479	–

sample corresponds to the amount of carbon in the initial reaction mixture and amounts to 3.8 ± 0.2 wt. %, while nitrogen and oxygen content are 2.3 ± 0.1 and 0.8 ± 0.2 wt. %, respectively. The chemical formula of bulk carbonitride can be written as follows: (Hf_{0.33}Ta_{0.33}Nb_{0.33})C_{0.5}N_{0.3}. For the resulting compound, the configuration entropy of mixing (S_{mix}) was 1.8, which meets the criteria for high-entropy materials $S_{mix} \geq 1.61R$ [29; 30].

Microhardness, Young's modulus and fracture toughness were studied on sintered samples. The mechanical properties of high-entropy (Hf,Ta,Nb)(C,N) carbonitride and similar materials are presented in Table 2. High-entropy (Hf,Ta,Nb)(C,N) carbonitride is characterized by higher hardness compared to (Ta_{0.5}Hf_{0.5})C_{0.51}N_{0.4} tantalum-hafnium carbonitride obtained in a similar way [11]. Considering that (Hf,Ta,Nb)(C,N) and (Ta_{0.5}Hf_{0.5})C_{0.51}N_{0.4} have almost the same grain size (2–15 μ m and 6–10 μ m, respectively), it can be assumed that the introduction of Nb into the composition of (Ta_{0.5}Hf_{0.5})C_{0.51}N_{0.4} tantalum-hafnium carbonitride contributed to increased hardness caused by enhanced configurational entropy of mixing. The similar effect was demonstrated in [9], where the hardness and fracture toughness increase with enhancing configurational entropy of mixing. Compared to other multicomponent carbonitrides [9; 31; 32] and carbides [33–35], (Hf,Ta,Nb)(C,N) demonstrated higher hardness (21.5 ± 0.4 GPa), as well as a comparable value of fracture toughness (3.7 ± 0.3 MPa·m^{1/2}).

Conclusions

1. We studied the impact of MA duration on the structure and phase composition of the Hf + Ta + Nb + C reaction mixture. It has been demonstrated that mechanical treatment in the low-energy mode for 60 min con-

tributes to the formation of layered composite particles with an average size of 13 μ m throughout the entire powder volume.

2. The powder after SHS included two isomorphic phases (Hf,Ta,Nb)(C,N) with lattice parameters of 0.4476 nm and 0.4469 nm *Fm-3m* (225) space group.

3. A dense high-entropy (Hf_{0.33}Ta_{0.33}Nb_{0.33})C_{0.5}N_{0.3} carbonitride with a relative density of 98 %, hardness of 21.5 ± 0.4 GPa, Young's modulus of 458 ± 10 GPa and fracture toughness of 3.7 ± 0.3 MPa·m^{1/2} was fabricated from the synthesized powder using the spark plasma sintering method.

References / Список литературы

- Xiang H., Xing Y., Dai F.Z., Wang H., Su L., Miao L., Zhang G., Wang Y., Qi X., Yao L., Wang H., Zhao B., Li J., Zhou Y. High-entropy ceramics: Present status, challenges, and a look forward. *Journal of Advanced Ceramics*. 2021;10(3):385–441.
<https://doi.org/10.1007/s40145-021-0477-y>
- Dewangan S.K., Mangish A., Kumar S., Sharma A., Ahn B., Kumar V. A review on high-temperature applicability: A milestone for high entropy alloys. *Engineering Science and Technology, an International Journal*. 2022;35:101211.
<https://doi.org/10.1016/j.jestch.2022.101211>
- Akrami S., Edalati P., Fuji M., Edalati K. High-entropy ceramics: Review of principles, production and applications. *Materials Science and Engineering: R: Reports*. 2021;146:100644.
<https://doi.org/10.1016/j.mser.2021.100644>
- Demirskyi D., Borodianska H., Suzuki T.S., Sakka Y., Yoshimi K., Vasylykiv O. High-temperature flexural strength performance of ternary high-entropy carbide consolidated via spark plasma sintering of TaC, ZrC and NbC. *Scripta Materialia*. 2019;164:12–16.
<https://doi.org/10.1016/j.scriptamat.2019.01.024>


5. Castle E., Csanádi T., Grasso S., Dusza J., Reece M. Processing and properties of high-entropy ultra-high temperature carbides. *Scientific Reports*. 2018;8:8609. <https://doi.org/10.1038/s41598-018-26827-1>
6. Hong Q.J., Van De Walle A. Prediction of the material with highest known melting point from ab initio molecular dynamics calculations. *Physical Review B*. 2015;92(2):020104. <https://doi.org/10.1103/PhysRevB.92.020104>
7. Zhang X., Li X., Zuo J., Luo R., Wang J., Qian Y., Li M., Xu J. Characterization of thermophysical and mechanical properties of hafnium carbonitride fabricated by hot pressing sintering. *Journal of Materials Research and Technology*. 2023;23:4432–4443. <https://doi.org/10.1016/j.jmrt.2023.02.099>
8. Peng Z., Sun W., Xiong X., Xu Y., Zhou Z., Zhan Z., Zhang H., Zeng Y. Novel nitrogen-doped hafnium carbides for advanced ablation resistance up to 3273 K. *Corrosion Science*. 2021;189:109623. <https://doi.org/10.1016/j.corsci.2021.109623>
9. Zhang P., Liu X., Cai A., Du Q., Yuan X., Wang H., Wu Y., Jiang S., Lu Z. High-entropy carbide-nitrides with enhanced toughness and sinterability. *Science China Materials*. 2021;64(8):2037–2044. <https://doi.org/10.1007/s40843-020-1610-9>
10. Suvorova V.S., Nepapushev A.A., Moskovskikh D.O., Kuskov K.V. Fabrication and oxidation resistance of the non-stoichiometric tantalum-hafnium carbonitride. *Powder Metallurgy and Functional Coatings*. 2022;(3):45–54. <https://doi.org/10.17073/1997-308X-2022-3-45-54>
 Суворова В.С., Непapushev А.А., Московских Д.О., Кусков К.В. Получение нестехиометрического тантала-гафниевого карбонитрида и исследование его окислительной стойкости. *Известия вузов. Порошковая металлургия и функциональные покрытия*. 2022;(3):45–54. <https://doi.org/10.17073/1997-308X-2022-3-45-54>
11. Buinevich V.S., Nepapushev A.A., Moskovskikh D.O., Kuskov K.V., Yudin S.N., Mukasyan A.S. Ultra-high-temperature tantalum-hafnium carbonitride ceramics fabricated by combustion synthesis and spark plasma sintering. *Ceramics International*. 2021;47(21):30043–30050. <https://doi.org/10.1016/j.ceramint.2021.07.180>
12. Dippo O.F., Mesgarzadeh N., Harrington T.J., Schrader G.D., Vecchio K.S. Bulk high-entropy nitrides and carbonitrides. *Scientific Reports*. 2020;10(1):21288. <https://doi.org/10.1038/s41598-020-78175-8>
13. Wang Y., Csanádi T., Zhang H., Dusza J., Reece M.J. Synthesis, microstructure, and mechanical properties of novel high entropy carbonitrides. *Acta Materialia*. 2022;231:117887. <https://doi.org/10.1016/j.actamat.2022.117887>
14. Peng Z., Sun W., Xiong X., Zhang H., Guo F., Li J. Novel refractory high-entropy ceramics: Transition metal carbonitrides with superior ablation resistance. *Corrosion Science*. 2021;184:109359. <https://doi.org/10.1016/j.corsci.2021.109359>
15. Peng C., Tang H., He Y., Lu X., Jia P., Liu G., Zhao Y., Wang M. A novel non-stoichiometric medium-entropy carbide stabilized by anion vacancies. *Journal of Materials Science & Technology*. 2020;51:161–166. <https://doi.org/10.1016/j.jmst.2020.02.049>
16. GOST 20018-74 (ST SEV 1253-78, ISO 3369-75). Sintered hard alloys: Density determination method (with changes No. 1, 2, 3). Moscow: Gosstandart SSSR, 1991. 11 p. (In Russ.).
 ГОСТ 20018-74 (СТ СЭВ 1253-78, ИСО 3369-75). Сплавы твердые спеченные: Метод определения плотности (с изменениями № 1, 2, 3). М.: Госстандарт СССР, 1991. 11 с.
17. GOST 2999-75. Metals and alloys: Vickers hardness measurement method (with changes No. 1, 2). Moscow: Management of standardization and certification of raw materials and materials, 1986. (In Russ.).
 ГОСТ 2999-75. Металлы и сплавы: Метод измерения твердости по Виккерсу (переизд. с изм. 1, 2). М.: Управление стандартизации и сертификации сырья и материалов, 1986.
18. Anstis G.R., Chantikul P., Lawn B.R., Marshall D.B. A critical evaluation of indentation techniques for measuring fracture toughness: I, direct crack measurements. *Journal of the American Ceramic Society*. 1981;64(9):533–538. <https://doi.org/10.1111/j.1151-2916.1981.tb10320.x>
19. Suvorova V.S. Fabrication of ultra-high-temperature ceramics based on hafnium carbonitride by self-propagating high-temperature synthesis: Diss. Cand. Sci. (Eng.). Moscow: MISIS, 2022. (In Russ.).
 Суворова В.С. Получение тугоплавких керамик на основе карбонитрида гафния методом самораспространяющегося высокотемпературного синтеза: Дис. ... канд. техн. наук. М.: МИСИС, 2022.
20. Liu G., Li J., Chen K. Combustion synthesis: Handbook of combustion: Online: Wiley-VCH Verlag GmbH & Co, 2015. 62 p. <https://doi.org/10.1002/9783527628148.hoc094>
21. Eslamlou-Grami M., Munir Z.A. The mechanism of combustion synthesis of titanium carbonitride. *Journal of Materials Research*. 1994;9(2):431–435. <https://doi.org/10.1557/JMR.1994.0431>
22. Mukasyan A.S., Rogachev A.S. Combustion synthesis: Mechanically induced nanostructured materials. *Journal of Materials Science*. 2017;52:11826–11833. <https://doi.org/10.1007/s10853-017-1075-9>
23. Mukasyan A.S., Lin Y.C., Rogachev A.S., Moskovskikh D.O. Direct combustion synthesis of silicon carbide nanopowder from the elements. *Journal of the American Ceramic Society*. 2013;96(1):111–117. <https://doi.org/10.1111/jace.12107>
24. Buinevich V.S., Nepapushev A.A., Moskovskikh D.O., Trusov G.V., Kuskov K.V., Vadchenko S.G., Rogachev A.S., Mukasyan A.S. Fabrication of ultra-high-temperature nonstoichiometric hafnium carbonitride via combustion synthesis and spark plasma sintering. *Ceramics International*. 2020; 46(10):16068–16073. <https://doi.org/10.1016/j.ceramint.2020.03.158>
25. Khadyrova I., Suvorova V., Nepapushev A., Suvorov D., Kuskov K., Moskovskikh D. Hafnium-zirconium carbonitride (Hf,Zr)(C,N) by one step mechanically induced self-sustaining reaction: Powder synthesis and spark plasma

- sintering. *Ceramics*. 2023;6(2):1129–1138.
<https://doi.org/10.3390/ceramics6020067>
26. Suvorova V., Khadyrova I., Nepapushev A., Kuskov K., Suvorov D., Moskovskikh D. Fabrication and investigation of novel hafnium-zirconium carbonitride ultra-high temperature ceramics. *Ceramics International*. 2023;49(14):23809–23816.
<https://doi.org/10.1016/j.ceramint.2023.04.222>
 27. Merzhanov A.G., Rogachev A.S. Structural macrokinetics of SHS processes. *Pure and Applied Chemistry*. 1992; 64(7):941–953. <https://doi.org/10.1351/pac199264070941>
 28. Deevi S.C. Structure of the combustion wave in the combustion synthesis of titanium carbides. *Journal of Materials Science*. 1991;26(10):2662–2670.
<https://doi.org/10.1007/BF00545552>
 29. Pikalova E.Y., Kalinina E.G., Pikalova N.S., Filonova E.A. High-entropy materials in SOFC technology: Theoretical foundations for their creation, features of synthesis, and recent achievements. *Materials*. 2022;15(24):8783.
<https://doi.org/10.3390/ma15248783>
 30. Golgovici F., Tudose A.E., Diniasi D., Nartit R., Fulger M., Demetrescu I. Aspects of applied chemistry related to future goals of safety and efficiency in materials development for nuclear energy. *Molecules*. 2023;28(2):874.
<https://doi.org/10.3390/molecules28020874>
 31. Han X.Q., Lin N., Li A.Q., Li J.Q., Wu Z.G., Wang Z.Y., He Y.H., Kang X.Y., Ma C. Microstructure and characterization of (Ti,V,Nb,Ta)(C,N) high-entropy ceramic. *Ceramics International*. 2021;47(24):35105–35110.
<https://doi.org/10.1016/j.ceramint.2021.09.053>
 32. Wen T., Ye B., Nguyen M.C., Ma M., Chu Y. Thermophysical and mechanical properties of novel high-entropy metal nitride-carbides. *Journal of the American Ceramic Society*. 2020;103(11):6475–6489.
<https://doi.org/10.1111/jace.17333>
 33. Li Z., Wang Z., Wu Z., Xu B., Zhao S., Zhang W., Lin N. Phase, microstructure and related mechanical properties of a series of (NbTaZr)C-based high entropy ceramics. *Ceramics International*. 2021;47(10):14341–14347.
<https://doi.org/10.1016/j.ceramint.2021.02.013>
 34. Ye B., Wen T., Nguyen M.C., Hao L., Wang C.Z., Chu Y. First-principles study, fabrication and characterization of (Zr_{0.25}Nb_{0.25}Ti_{0.25}V_{0.25})C high-entropy ceramics. *Acta Materialia*. 2019;170:15–23.
<https://doi.org/10.1016/j.actamat.2019.03.021>
 35. Yan X., Constantin L., Lu Y., Silvain J.F., Nastasi M., Cui B. (Hf_{0.2}Zr_{0.2}Ta_{0.2}Nb_{0.2}Ti_{0.2})C high-entropy ceramics with low thermal conductivity. *Journal of the American Ceramic Society*. 2018;101(10):4486–4491.
<https://doi.org/10.1111/jace.15779>

Information about the Authors




Veronika S. Suvorova – Cand. Sci. (Eng.), Researcher at the Research Center of Engineering Ceramic Nanomaterials at the National University of Science and Technology “MISIS” (NUST MISIS)

 **ORCID:** 0000-0002-0335-9153

 **E-mail:** buynevich.vs@misys.ru

Andrey A. Nepapushev – Cand. Sci. (Eng.), Researcher at the Research Center of Engineering Ceramic Nanomaterials, NUST MISIS

 **ORCID:** 0000-0001-9017-9937

 **E-mail:** anepapushev@gmail.com

Dmitry S. Suvorov – Engineer at the Department of Functional Nanosystems and High Temperature Materials, NUST MISIS

 **ORCID:** 0000-0002-0358-9987

 **E-mail:** suvorov.ds@misys.ru

Kirill V. Kuskov – Leading Expert at the Research Center of Engineering Ceramic Nanomaterials, NUST MISIS

 **ORCID:** 0000-0002-9387-0237

 **E-mail:** kkuskov@misys.ru


Dmitry O. Moskovskikh – Cand. Sci. (Eng.), Director of the Research Center of Engineering Ceramic Nanomaterials, NUST MISIS

 **ORCID:** 0000-0001-5168-4885

 **E-mail:** mos@misys.ru

Сведения об авторах

Вероника Сергеевна Суворова – к.т.н., науч. сотрудник НИЦ «Конструкционные керамические наноматериалы» Национального исследовательского технологического университета «МИСИС» (НИТУ МИСИС)

 **ORCID:** 0000-0002-0335-9153

 **E-mail:** buynevich.vs@misys.ru

Андрей Александрович Непанушев – к.т.н., ст. науч. сотрудник НИЦ «Конструкционные керамические наноматериалы» НИТУ МИСИС

 **ORCID:** 0000-0001-9017-9937

 **E-mail:** anepapushev@gmail.com

Дмитрий Сергеевич Суворов – инженер кафедры функциональных наносистем и высокотемпературных материалов НИТУ МИСИС

 **ORCID:** 0000-0002-0358-9987

 **E-mail:** suvorov.ds@misys.ru

Кирилл Васильевич Кусков – вед. эксперт НИЦ «Конструкционные керамические наноматериалы» НИТУ МИСИС

 **ORCID:** 0000-0002-9387-0237

 **E-mail:** kkuskov@misys.ru

Дмитрий Олегович Московских – к.т.н., директор НИЦ «Конструкционные керамические наноматериалы» НИТУ МИСИС

 **ORCID:** 0000-0001-5168-4885

 **E-mail:** mos@misys.ru

Contribution of the Authors



V. S. Suvorova – determining the objective of the study, conducting experiments, writing the article.

A. A. Nepapushev – determining the objective of the study, writing the article.

Вклад авторов

В. С. Суворова – формулировка цели исследования, проведение экспериментов, написание статьи.

А. А. Непанушев – формулировка цели исследования, написание статьи.

D. S. Suvorov – conducting X-ray diffraction analysis, analyzing the particle size after mechanical activation and self-propagating high-temperature synthesis, participating in the discussion of the results.

K. V. Kuskov – studying the structure and elemental composition by SEM, participating in the discussion of the results.

D. O. Moskovskikh – studying the chemical composition of the samples, participating in the discussion of the results.

Д. С. Суворов – проведение рентгенофазового анализа, анализ размера частиц после механического активирования и самораспространяющегося высокотемпературного синтеза, участие в обсуждении результатов.

К. В. Кусков – исследование структуры и элементного состава образцов методом сканирующей электронной микроскопии, участие в обсуждении результатов.

Д. О. Московских – исследование химического состава образцов, участие в обсуждении результатов.

Received 28.09.2023

Revised 08.12.2023

Accepted 12.12.2023

Статья поступила 28.09.2023 г.

Доработана 08.12.2023 г.

Принята к публикации 12.12.2023 г.



UDC 533.72; 533.59

<https://doi.org/10.17073/1997-308X-2024-3-49-61>Research article
Научная статья

Physical and mathematical model of the silicon vapor transport during high-temperature silicification of a porous carbon media

M. V. Ageeva^{1, 2}, V. A. Demin^{1, 3}✉, T. V. Demina^{1, 2}¹ Perm State National Research University

15 Bukirev Str., Perm 614068, Russia

² Institute of Continuous Media Mechanics, Ural Branch, Russian Academy of Sciences

1 Korolev Str., Perm 614013, Russia

³ Perm National Research Polytechnic University

29 Komsomolskiy Prosp., Perm 614990, Russia

✉ demin@psu.ru

Abstract. A new physical and mathematical model of silicon vapor transport under medium vacuum conditions has been developed, which makes it possible to explain the anomalously intense mass transfer of silicon during high-temperature silicification of a porous carbon material. A formula has been derived showing how the product must be supercooled in order for the condensation process to occur in its pores. The resulting modified diffusion equation makes it possible to determine quantitatively the flow of gaseous silicon into the sample, which is highly demanded in the implementation of the porous fiber carbidization technology and the subsequent complete saturation of the product pores with unreacted silicon. We introduce and quantify a new parameter, showing the contribution of convective transport to the overall mass transfer of silicon through an external gas medium, the role of which is played by argon. An exact analytical solution of the equation for silicon transfer in a one-dimensional formulation has been found for a layer of porous medium with a flat surface. The solution has the form of a logarithmic profile and allows us to calculate the flow of gaseous silicon at the entrance to the product. The proposed approach is demonstrated on the example of two-dimensional calculations performed by the finite difference method, however, the proposed model is easily generalized to the case of three-dimensional calculations with complex geometry, which always has to be dealt with in a real technological process. Calculations in a two-dimensional formulation have performed for two model systems: when the melt mirror and the product are parallel or perpendicular to each other. The dynamics of silicon vapor propagation in the retort has been studied. It is shown that in the conditions under consideration, gaseous silicon, after the onset of vaporization, fills the entire space of the retort in a characteristic time of less than 1 s.

Keywords: functional coatings, high-temperature silicification, numerical simulation

For citation: Ageeva M.V., Demin V.A., Demina T.V. Physical and mathematical model of the silicon vapor transport during high-temperature silicification of a porous carbon media. *Powder Metallurgy and Functional Coatings*. 2024;18(3):49–61. <https://doi.org/10.17073/1997-308X-2024-3-49-61>

Физико-математическая модель доставки паров кремния в ходе высокотемпературного силицирования пористых углеродных материалов

М. В. Агеева^{1, 2}, В. А. Демин^{1, 3}, Т. В. Демина^{1, 2}

¹ Пермский государственный национальный исследовательский университет
Россия, 614068, г. Пермь, ул. Букирева, 15

² Институт механики сплошных сред Уральского отделения РАН
Россия, 614013, г. Пермь, ул. Королева, 1

³ Пермский национальный исследовательский политехнический университет
Россия, 614990, г. Пермь, Комсомольский пр-т, 29

✉ demin@psu.ru

Аннотация. Разработана новая физико-математическая модель транспорта паров кремния в условиях среднего вакуума, позволяющая объяснить аномально интенсивный массоперенос кремния в ходе высокотемпературного силицирования пористого углеродного материала. Выведена формула, показывающая, как изделие должно быть переохлаждено, чтобы в его порах шел процесс конденсации. Получено модифицированное уравнение диффузии для количественного определения распределения концентрации газообразного кремния в реторте, что крайне востребовано при реализации технологии карбидизации углеродного волокна и последующего полного насыщения пор силицируемого изделия непрореагировавшим кремнием. Введен и количественно оценен новый параметр, показывающий вклад конвективного транспорта в общий массоперенос кремния через среду стороннего газа, роль которого играет аргон. Найдено точное аналитическое решение этого уравнения в одномерной постановке для слоя пористой среды с плоской поверхностью. Решение имеет вид логарифмического профиля и позволяет вычислить поток газообразного кремния на входе в изделие. Иллюстрация работоспособности предлагаемого подхода, более приближенная к действительности, производится путем двумерных расчетов, выполненных методом конечных разностей. В то же время предлагаемая модель легко обобщается на случай трехмерных вычислений со сложной геометрией, с чем всегда приходится иметь дело в реальном технологическом процессе. Расчеты в двумерной постановке выполнены для двух модельных систем, когда зеркало расплава и изделие параллельны или перпендикулярны друг другу. Исследована динамика распространения паров кремния в реторте. Показано, что в рассматриваемых условиях газообразный кремний после начала парообразования заполняет все пространство реторты за характерное время менее 1 с.

Ключевые слова: функциональные покрытия, высокотемпературное силицирование, численное моделирование.

Для цитирования: Агеева М.В., Демин В.А., Демина Т.В. Физико-математическая модель доставки паров кремния в ходе высокотемпературного силицирования пористых углеродных материалов. *Известия вузов. Порошковая металлургия и функциональные покрытия*. 2024;18(3):49–61. <https://doi.org/10.17073/1997-308X-2024-3-49-61>

Introduction

Currently, composite materials (CM) occupy a serious niche in all industries and are used both for manufacturing individual products and as coatings with special properties. CM unique properties account for their active use. In particular, CMs obtained by high temperature silicification of a porous carbon frame have high antioxidant properties, low density and, with the proper technique used, a high degree of tightness [1; 2]. Technologically, high temperature silicification is conducted under medium vacuum conditions in the inert carrier gas (argon) [3].

The attempts were earlier made to develop a complete physical and mathematical model for the vapor-phase silicification method, which included a quantitative description of the process of filling pores inside the sample and, in addition, solving the adjoint

problem of silicon vapor transfer from the melt mirror to the product [4–6]. However, the authors of these works faced an unbridgeable gap between the calculation results and experimental data at the stage of numerical simulation of the diffusion transport of silicon vapor in the working space of the retort. The physical and mathematical model underlying the description of the process was based on the assumption that the main transfer mechanism is diffusion, and the concentration of silicon vapor on the melt mirror at a given operating temperature cannot exceed that of the saturated vapor. According to the diffusion equation solution, even if silicon is fully consumed on the surface of the sample, the vapor mass flow proves insufficient to completely siliconize the product within a reasonable time. The authors of [4–6] predicted that for silicon vapor to overcome the diffusion barrier in the form of an atmosphere of residual gas during silicification,

the crucibles with the melt should be put as close to the product as possible, while in reality this factor is not decisive, and often some areas of a largesized product remain “dry”, despite the fact that the crucibles with molten silicon are located as close to the sample surface as possible.

Moreover, the experience shows that porous carbon matrices can be saturated with silicon, and various variants of this technique have long been commercially implemented in many manufacturing procedures. Thus, it is still very important to quantitatively determine the mass flow of silicon vapor through the blank surface for monitoring the manufacturing procedure when functional coatings are formed or the process of deep impregnation of a porous material is controlled.

All currently known modern techniques for producing high temperature CMs are continuously improved [7–9] and, due to their increasing complexity, require more advanced approaches at different implementation stages, including the construction of new physical and mathematical models to describe the processes occurring. Applied to real production conditions, the process of gaseous silicon transfer from the melt mirror to the product surface during high temperature silicification of a carbon porous material must be described by an elaborate system of partial differential equations, and its adequate simulation requires tracking of many complicating factors, including convective mass transfer [10]. At the same time, the technique is essentially three-dimensional and requires a highly detailed computational grid due to numerous crucibles with melt in the retort and their complex arrangement in the working space of the furnace [7]. At the moment, the fullfledged 3D numerical simulation of this process is impossible. As a result, the available models for describing the gaseous silicon transfer in the hearth of an industrial furnace during high temperature silicification are limited to elemental approaches. As this process is conducted in the medium vacuum and at extremely high temperatures above the silicon melting point ($T > 1683$ K), diffusion was believed to play a decisive role in ensuring the transfer of gaseous silicon from the melt to the product, and it was the only value taken into account in physical analysis-mathematical models [4–6].

The use of real values of the diffusion coefficient in the transfer equation does not ensure silicon supply in the amount required for full-fledged silicification of the product that can be experimentally observed. We face a paradoxical situation, since the facts speak for themselves: the experiments show that under certain conditions, a product can still be saturated with the required amount of silicon, but the existing theory denies this possibility. This means that we do not fully

understand all physical conditions required for the successful implementation of the silicification process.

Thus, the objective of this work is to explain the experimentally observed abnormally strong transfer of gaseous silicon from the melt mirror to the product surface. The goal of the theoretical study is to construct a more advanced physical and mathematical model of the silicon vapor transfer in the working space of the retort. This model should be tested on the example of specific formulations to prove that it is more plausible compared to its purely diffusion analogue.

Analysis of basic equations

The equation of classical diffusion in a three-dimensional formulation [11], which is conventionally used to calculate the distribution of silicon vapor in a retort, looks as follows

$$\frac{\partial C}{\partial t} = D \left(\frac{\partial^2 C}{\partial x^2} + \frac{\partial^2 C}{\partial y^2} + \frac{\partial^2 C}{\partial z^2} \right),$$

where D is the diffusion coefficient (assumed to be a constant) and C is the mass concentration. This is a wellknown second-order partial parabolic differential equation. In the stationary case ($\partial/\partial t = 0$), the problem is simplified and reduced to Laplace’s equation $\Delta C = 0$.

To begin with, without getting into specifics of the manufacturing method, it makes sense, following the study [10], to consider the process as a simple model, when the product surfaces and the melt are two parallel planes located at a distance L from each other (Fig. 1). Hereinafter we will neglect the effect of gravity. Suppose the concentration of saturated silicon vapor $C(L) = C_s$ is specified on the melt mirror, while on the left boundary, as gaseous silicon is completely absorbed by the porous medium, the condition $C(0) = 0$ is maintained.

In a one-dimensional formulation, Laplace’s equation with these boundary conditions leads to the only nontrivial solution in the form of a linear dependence

$$C(x) = \frac{C_s}{L} x,$$

which is schematically shown in Fig. 1. The characteristic distance L between the melt mirror and the product is about $0.5 \div 1.5$ m.

According to the experimental data, the saturated vapor pressure for silicon at temperatures not much higher than the silicon melting point is very low and is equal in order of magnitude to $p_s = 10$ Pa [12; 13]. The volumetric concentration for gaseous silicon in the saturated state is calculated based on the saturated

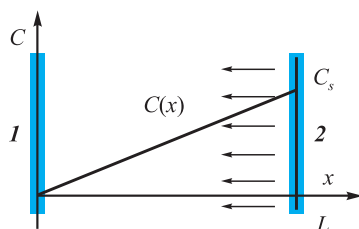


Fig. 1. Geometry of the problem

1 – product, 2 – surface of the melt
 C_s – concentration of saturation

Рис. 1. Геометрия задачи

1 – изделие, 2 – поверхность расплава
 C_s – концентрация насыщения

vapor pressure using the gas equation. At an operating temperature is 1800 K, it gives a value of the order of $n_s \sim 4 \cdot 10^{20} \text{ m}^{-3}$. Let us compare the theoretically predicted silicon flux density with the experimentally observed value. The silicon transfer is determined by diffusion only, however, in this case the silicon flux density is determined by Fick's equation:

$$\bar{j}_{\text{Si}} = -\rho D \nabla C = -D \nabla \rho_{\text{Si}}, \quad (1)$$

where ρ is gas density and C is mass concentration. We will assess the diffusion coefficient of silicon atoms for medium vacuum conditions in an argon atmosphere using the wellknown formula of the molecular kinetic theory [14]:

$$D = \frac{3}{8} \frac{kT}{\sigma_{12} p} \sqrt{\frac{\pi kT}{2\mu_{12}}} = \frac{3}{8} \frac{(kT)^{3/2}}{d_{\text{Si}}^2 p \sqrt{\pi m_0}}. \quad (2)$$

Where σ_{12} is a crosssection for scattering for two particles, μ_{12} is a reduced mass, and k is the Boltzmann constant. For two particles with approximately equal mass and size, we have $\sigma_{12} = \pi d^2$, $\mu_{12} = m_0/2$. The mass of one silicon atom is equal to $m_0 = 4.7 \cdot 10^{-26} \text{ kg}$. From the tabulated data we take the diameter of a silicon atom $d_{\text{Si}} = 2.3 \cdot 10^{-10} \text{ m}$. We thus obtain $D = 0.7 \text{ m}^2/\text{s}$. Such an unusually large value of the diffusion coefficient is attributed to two factors: the environment under the medium vacuum conditions is extremely rarified and the temperature is high.

Taking into account that the density of silicon on the melt mirror is $\rho_{\text{Si}} = p_{\text{Si}} \mu_{\text{Si}} / (RT) = 1.87 \cdot 10^{-5} \text{ kg/m}^3$, the formula (1) predicts a very low silicon flux density: $j_{\text{Si}} = 2.62 \cdot 10^{-5} \text{ kg/(m}^2 \cdot \text{s)}$. The industrial engineers specializing in silicification of carbon products claim that this is clearly not enough to completely block the pores within reasonable time, given the material porosity. However, in practice, if certain conditions experimentally determined by industrial engineers are met, products of various shapes are still successfully saturated

with silicon. Thus, we can confidently state that all failures during the manufacturing procedure are determined by completely different factors, namely the temperature distribution throughout the product [15]. It is obvious that silicon vapor can transit from a gaseous state to a liquid or solid state only if the product temperature is lower than that of vapor [16–18]. After equalizing the temperature, in theory the process of silicification should stop due to condensation in the porous material. In this case, the surrounding gas and the product come into thermodynamic equilibrium. For a general understanding, let us calculate how much the product should be supercooled so that silicon is condensed on it. The boundary between two phases (vapor and liquid) is determined by the so-called Clapeyron–Clausius equation [19], which, as is known, is derived from the condition of continuity of the thermodynamic potential:

$$\frac{dP}{dT} = \frac{q}{T(v_1 - v_2)}, \quad v_1 = \frac{V_1}{m_1}, \quad v_2 = \frac{V_2}{m_2}. \quad (3)$$

Where q is specific heat of the phase transition; P is gas pressure; T is temperature; v_1 , v_2 is specific volumes of vapor and liquid, respectively, m^3/kg . It should be noted that for vapor and liquid the expression $v_1 \gg v_2$ is valid; so, the equation (3) can be simplified to

$$\frac{dT}{dP} = \frac{vT}{q}. \quad (4)$$

In the approximation under consideration, the index corresponding to the vapor specific volume is not required and it is omitted in further calculations. The phase transition curve is shown schematically in Fig. 2.

We will assume that the actual conditions for silicon vapors during silicification are not far from the saturation state and correspond to temperature T_1 . The transition to a supersaturated state at the same pressure obviously requires lower product temperature. Suppose the assumed saturated vapor pressure at temperature T_1 is equal to P_1 . Since in reality the vapor is not saturated, its real pressure is ϕP_1 , where ϕ is relative vapor humidity. In practice, with decreasing temperature, the vapor pressure automatically drops to the value P_2 .

The gas volume and mass remain the same, so we get an isochoric process described by the equation

$$\frac{P_2}{T_2} = \frac{\phi P_1}{T_1}.$$

In Fig. 2, the isochoric process is indicated by arrows, and the final state is characterized by the threshold pressure and temperature corresponding

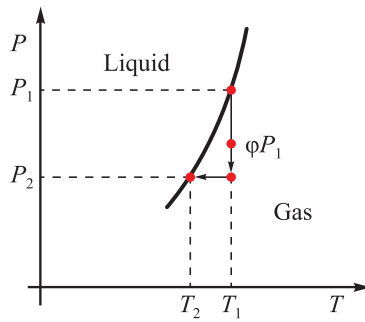


Fig. 2. P – T diagram of phase states

Рис. 2. Фазовые состояния на диаграмме P – T

to the condensation point. Hence, we get the pressure in the final state: $P_2 = \varphi P_1 T_2 / T_1$.

On the other hand, at each point on the phase diagram, the gas state is described by the Mendeleev–Clapeyron equation, from which the specific volume can be derived from the vapor pressure and temperature:

$$\frac{PV}{T} = \frac{Rm}{\mu}, \quad \frac{Pv}{T} = \frac{R}{\mu}, \quad v = \frac{RT}{\mu P}, \quad (5)$$

where V is overall volume, μ molar mass, R is universal gas constant, and v is volume per unit mass. For the sake of clarity, we replace the derivative in the Clapeyron–Clausius equation (4) with finite differences, at the same time eliminating the specific volume using the equation (5):

$$\frac{T_2 - T_1}{P_2 - P_1} = \frac{vT_1}{q}, \quad \frac{T_2 - T_1}{P_2 - P_1} = \frac{RT_1^2}{q\mu P_1}. \quad (6)$$

It should be noted that, from a mathematical point of view, the derivative in the equation (6) represents the so-called onesided difference in point 1. Next, we substitute the expression for pressure P_2 during the isoprocess in the equation (6) and derive the required temperature difference. The initial pressure P_1 reduces in the resultant expression, and, at first glance, it seems strange that nothing depends on it. However, unambiguous complete information about the initial state of silicon vapor is still contained in this equation, since in addition to temperature it includes vapor relative humidity. Simple arithmetic operations enable to express the final temperature difference:

$$T_2 - T_1 = \frac{RT_1^2(\varphi - 1)}{\mu q - RT_1 \varphi}. \quad (7)$$

The formula (7) shows that the temperature difference is negative, therefore, the product temperature should be lowered compared to the gas temperature. As an example, let us estimate the temperature

difference for realistic parameter values: $\varphi = 0.8$, $q = 13.8 \cdot 10^6$ J/kg, $\mu = 28 \cdot 10^{-3}$ kg/mol, $T_1 = 1790$ K. The selected temperature T_1 exceeds the silicon melting point by 102 K. It stays within the operating temperature range of the retort. The resulting equation is $T_2 - T_1 = -15$ K.

In other words, according to the calculations, the required temperature difference is small, but, the analysis of the thermophysical situation under industrial conditions reveals that this temperature factor is not controlled at all and this requirement is unlikely to be met in the fullscale manufacturing process. The estimates show that higher temperatures in the upper area of the working space inside the retort have an especially negative impact. This explains why, when largesized products are siliconized, their upper part is often less saturated with silicon than the lower part. The reason is that at the base of the product the temperature is much lower most of the time than in the upper area. All physical factors affecting uniform temperature distribution up and down the retort contribute to enhancing this stratification. The convection, the vacuum pumps located near the bottom, low thermal insulation at the base of the working space, side heaters positioned quite high from the base – all these factors result in a specific thermal stratification with a temperature gradient mostly directed upward vertically. Therefore, the temperature difference required by the formula (7) between silicon vapor and the product, can only occur near the lower boundary of the working space, if at all.

However, let us return to the truly pressing issue of supplying silicon vapor to the product, since it is clear that it must be solved regardless of the problem related to heat distribution in the retort during silicification.

New physical and mathematical model of silicon vapor transfer

We will assume that under the conditions under consideration, there is an additional convective transport mechanism, along with the diffusive one. A more general equation for the transport of an impurity as a continuous medium, taking this factor into account [11], is written as follows

$$\frac{\partial C}{\partial t} + (\vec{V} \nabla) C = D \Delta C, \quad (8)$$

where \vec{V} is macroscopic (mass) speed of a physically small element of gas.

The main problem related to the use of the equation (8) is its closure. Within the framework of continuum mechanics, fluid dynamics are generally deter-

mined by the Navier–Stokes equation [11]. In the case of three-dimensional calculations, these are three non-linear partial differential equations for three velocity components $v_i(x, y, z, t)$, where $i = 1, 3$. These equations include two more unknown quantities – pressure and variable density, which also has to be determined during the problem solution. As a result, two more equations are added to the system: conservation of mass in differential form and the equation of state. Thus, the resulting system of equations becomes extremely lengthy and difficult to solve.

Currently, direct numerical simulation of the processes under consideration in a full three-dimensional formulation is very difficult, even when high-performance supercomputers are used. The challenge is to formulate the problem in a simplified way so that two conditions are simultaneously met – on the one hand, all the physical factors relevant for an adequate description of these processes should be taken into account, and on the other hand, models should not be unnecessarily complex so that the problem could be calculated within a reasonable time and would not require excessive computing power.

Following the approach implemented in [10], we will consider the Navier–Stokes equation in its full formulation and evaluate the contribution of each term, assuming that gaseous silicon moves through the argon parent fluid as through a porous medium. In the hydrodynamics of porous media [20], it is important to distinguish between pore velocity \vec{v} and filtration velocity \vec{v} . The filtration rate is determined through the total fluid flow rate and is connected with the pore velocity by the relation $\vec{v} = \phi \vec{v}$. Where ϕ is porosity of the material. For determining pore velocity in the medium, we use the initial motion equation [20]:

$$\rho_f \left(\frac{\partial \vec{v}}{\partial t} + (\vec{v} \nabla) \vec{v} \right) = -\nabla p - \frac{\eta}{\kappa} \vec{v}.$$

Where ρ_f is density of the fluid moving through a porous medium, η is dynamic viscosity, κ is permeability and p pressure field. This equation assumes linear dependence of friction on the filtration rate. For simplicity, gravity is not taken into account. Coming over to the filtration rate, we get

$$\rho_f \left(\phi^{-1} \frac{\partial \vec{v}}{\partial t} + \phi^{-2} (\vec{v} \nabla) \vec{v} \right) = -\nabla p - \frac{\eta}{\kappa} \vec{v}. \quad (9)$$

Now we can evaluate the terms related to speed on the left and right sides of this equation. The least trivial parameter in this equation is permeability κ . In our case, this is the permeability of argon gas with respect to the flow of silicon atoms. Regarding the mobile atoms of the carrier medium (argon), we can

only talk about the model nature of this gas as a porous material with some effective permeability. We will keep in mind the model according to which gaseous silicon, as a kind of fluid, is filtered through a carrier medium as excessive amounts of silicon vapor emerge on the melt mirror and are absorbed at the opposite boundary. Due to the extreme rarefaction of the carrier medium, permeability κ is expected to be abnormally high. At the same time, the porosity is close to unity, since argon atoms, as scattering centers, occupy an extremely small volume.

Suppose the medium is a system of small solid spherical centers washed by a hydrodynamic flow. The interatomic distance in argon is equal in order of magnitude to the freepath length of

$$l = \frac{kT}{\sqrt{2} \pi d^2 p} = \frac{1.38 \cdot 10^{-23} \cdot 1800}{\sqrt{2} \pi (1.4 \cdot 10^{-10})^2 \cdot 100} = 5.6 \cdot 10^{-3} \text{ m}.$$

The argon atom diameter is $d = 1.4 \cdot 10^{-10}$ m. According to the manufacturing procedure, argon partial pressure is on the order of 100 Pa. The resulting equation for permeability is $\kappa \sim l^2 = 3.1 \cdot 10^{-5} \text{ m}^2$.

However, this assessment gives a slightly underestimated permeability value, since it is valid in the case of dense packing of obstacles. For a more accurate estimate, we will use the wellknown Kozeny–Karman formula [20]. This formula is widely used in the theory of porous media and is derived from the most general geometric considerations. As a result, we get

$$\kappa = \frac{\phi^3 d^2}{(1 - \phi)^2} = 5 \cdot 10^{-4} \text{ m}^2.$$

Where ϕ is porosity of the carrier medium (argon) and d is characteristic size of the streamlined obstacle (in our case, these are argon atoms).

Another important parameter is the macroscopic velocity of the gas element (filtration rate). We will assume that during evaporation, silicon atoms separate from the melt surface with a rootmean-square velocity, which amounts to ~ 1250 m/s at $T = 1800$ K. Averaging over all possible directions, we obtain the value of the velocity projection onto the normal (filtration speed) $v \sim 310$ m/s. Now let us assess the value of each term in the equation (9), taking into account that the porosity of such a medium is close to unity and that stationary motion is considered ($\partial/\partial t = 0$):

$$\begin{aligned} \left| \rho_f \phi^{-2} (\vec{v} \nabla) \vec{v} \right| &\sim \rho_f \frac{v^2}{L} = 2 \cdot 10^{-5} \frac{310^2}{0.5} = 3.8, \\ \left| \rho_f \phi^{-1} \frac{\partial \vec{v}}{\partial t} \right| &= 0, \quad \left| \frac{\eta \vec{v}}{\kappa} \right| = \frac{3.5 \cdot 10^{-4} \cdot 310}{5 \cdot 10^{-4}} = 217. \end{aligned}$$

These estimates show that the viscosity term is dominant in this equation. Namely: both the inertia term and the term that expresses nonstationarity of processes are negligible compared to the viscosity term:

$$\left| \frac{\eta \bar{v}}{\kappa} \right| \gg \left| \rho_f \phi^{-2} (\bar{v} \nabla) \bar{v} \right|.$$

Therefore, we derive the formula for speed in the form of the wellknown Darcy's law [20] from the equation (9):

$$\bar{v} = -\frac{\kappa}{\eta} \nabla p_{\text{Si}}. \quad (10)$$

Due to evaporation on the melt mirror and absorption on the product, we get an average silicon vapor density gradient. The gas pressure is generally proportional to density, which generates a silicon pressure gradient and it can act as an additional driving force along with diffusion. According to the gas equation, the silicon partial pressure is equal to $p_{\text{Si}} = n_{\text{Si}} kT$, where $n_{\text{Si}} = N_{\text{Si}}/V$ is the number of silicon atoms per unit volume. Let us express n_{Si} in terms of the mass concentration C . By definition, by mass concentration we mean

$$C = \frac{m_{\text{Si}}}{m_a + m_{\text{Si}}} = \frac{\rho_{\text{Si}}}{\rho_a + \rho_{\text{Si}}},$$

then the silicon density is expressed in terms of relative mass concentration as follows:

$$\rho_{\text{Si}} = \frac{C}{1-C} \rho_a. \quad (11)$$

Let us write the equation for the silicon partial pressure in terms of the silicon density and substitute the formula (11) in it:

$$p_{\text{Si}} = \frac{RT}{\mu_{\text{Si}}} \frac{C}{1-C} \rho_a. \quad (12)$$

Next, let us substitute this result into the Darcy's law (10), neglecting the spatial inhomogeneities of argon density and temperature in the retort. Let us also take into account the fact that the silicon concentration never actually reaches unity. Argon or residual air is always present in the retort, and their concentration is approximately an order of magnitude higher than that of silicon vapor. Eventually, we expand the factor $C/(1-C)$ into a series in small C and limit our final formula to the first non-vanishing term. The Darcy's law (10) takes the form

$$\bar{v} = -\frac{\kappa}{\eta} \nabla p_{\text{Si}} = -\frac{\kappa}{\eta} \frac{RT \rho_a}{\mu_{\text{Si}}} \nabla C. \quad (13)$$

However, the equation (8) includes the average mass velocity

$$\bar{V} = \frac{\rho_a \bar{v}_a + \rho_{\text{Si}} \bar{v}_{\text{Si}}}{\rho_a + \rho_{\text{Si}}} = \frac{\rho_{\text{Si}} \bar{v}_{\text{Si}}}{\rho_a + \rho_{\text{Si}}} \approx \frac{\rho_{\text{Si}} \bar{v}_{\text{Si}}}{\rho_a}.$$

We substitute (13) into this formula, exclude the velocity from the extended impurity transfer equation (8) and end up with the equation

$$\frac{\partial C}{\partial t} - \frac{\kappa RT \rho_{\text{Si}}}{\eta \mu_{\text{Si}}} (\nabla C)^2 = D \Delta C. \quad (14)$$

Now this is a more complex partial differential equation with a nonlinearity like the square of the concentration gradient, but for one variable $C(x, y, z, t)$. It should be noted that similar diffusion equations with nonlinearities, quadratic function of the concentration gradient, are found in various fields of physics, but are derived differently. Thus, the studies [21; 22] showed that a nonlinear term of this type changes the material (lithium niobate) transport diffusion properties quite significantly and enables to explain some of the observed effects associated with the medium under consideration being saturated with hydrogen. In the general case, the equation (14) enables to solve non-stationary problems of concentration distribution in a three-dimensional formulation.

Analytical solution

First of all, it makes sense to analyze the equation (14) for the stationary solution. Given that $\partial/\partial t = 0$, the equation (14) is reduced to the form

$$-(\nabla C) = \psi \Delta C, \quad \psi = \frac{\eta \mu_{\text{Si}} D}{\kappa RT \rho_{\text{Si}}}, \quad (15)$$

where ψ is a new dimensionless parameter. Let us estimate the value of the introduced parameter, which loosely determines the relationship between diffusive and convective mechanisms. Let us take the value of dynamic viscosity from [10]. In the work mentioned above, this parameter was assessed in relation to the silicification process under consideration, based on the wellknown formulas of molecular kinetic theory [14]:

$$\eta = \frac{\frac{1}{3} \left(\frac{2}{\pi} \right)^{3/2} (m_0 kT)^{1/2}}{d_{\text{Ar}}^2} = 3.5 \cdot 10^{-4} \text{ m}^2/\text{s}.$$

Assessment of the parameter ψ for the permeability value $\kappa = 5 \cdot 10^{-4} \text{ m}^2$ results in $\psi = 0.048$. This means that, under the conditions under consideration, convec-

tive transport significantly contributes to silicon vapor transport.

In the one-dimensional formulation with regard to the geometry of the problem presented in Fig. 1, the equation (15) has an exact solution. Namely, let us formulate the boundary value problem for the unknown function $C(x)$ in the form of an ordinary second-order differential equation and two boundary conditions:

$$-\left(\frac{dC}{dx}\right) = \psi \frac{d^2C}{dx^2}; \quad C(0) = 0, \quad C(L) = C_s.$$

By substituting a variable, the order of the equation is reduced, and then the elementary equation is integrated [23]. As a result, taking into account the abovementioned homogeneous boundary conditions, we obtain the logarithmic dependence

$$C(x) = \psi \ln \left\{ \frac{x}{L} \left[\exp \left(\frac{C_s}{\psi} \right) - 1 \right] + 1 \right\}. \quad (16)$$

For completeness, we can calculate the derivative of this solution on the left boundary. With this derivative value, the silicon vapor flux density is an order of magnitude higher than in the case of purely diffusive transfer: $j_{Si} = 3.0 \cdot 10^{-4} \text{ kg/(m}^2 \cdot \text{s)}$. Let us present as an example a dependency graph $C(x)$ for $L = 1.6 \text{ m}$. Now the solution is a convex function. Fig. 3 (curve 4) shows that the largest derivative is right on the left boundary of the range of definition, i.e. on the product surface. The flux density is proportional to the magnitude of the derivative. Thus, to explain the high rate of high temperature saturation of carbon material in the medium vacuum observed in experiments, we should take into account the independent convective transport of silicon vapor in addition to diffusive transport. Moreover, silicon vapor now fills almost the entire working space of the retort. It is only in a thin boundary layer near the product itself that the concentration of silicon vapor tends to zero due to the assumed complete absorption. It is well consistent with the data of the fullscale experiment in the sense that silicon condensation can be intensive within the retort in places much removed from the crucibles.

One-dimensional non-stationary solution

Let us now make calculations to solve a non-stationary problem. The one-dimensional solution will be our primary interest.

The equation (14) is nonlinear, so the easiest way to obtain its non-stationary solution is numerical, using the finite difference method [24]. Sampling

schemes of first-order accuracy were used to approximate derivatives in both time and space. First order accuracy for spatial derivatives with “backward differences” was used to ensure the stability of the difference scheme. The program code was implemented in the FORTRAN-90 language. The number of nodes along the spatial coordinate was taken to be $N = 85$.

The dynamics of the concentration front presented for different sampling times in Fig. 3 shows that the solution quite quickly reaches a steady stationary profile in the form of the previously described convex function (the graphs were obtained for $L = 1.6 \text{ m}$). The calculation results show that it takes $\sim 2 \text{ s}$ to reach the stationary profile. At first, silicon vapor is only observed at the melt mirror (curve 1 in Fig. 3). Then, very quickly, silicon fills the entire space inside the retort (Fig. 3, curve 2, 3). At the moment of defining (Fig. 3, curve 4), the largest derivative is on the left boundary of the range of definition, i.e. on the product surface. The numerical solution of the generalized equation of silicon vapor diffusion during silicification of a porous carbon material obtained in the course of this study shows that gaseous silicon quickly occupies almost the entire volume of the furnace working

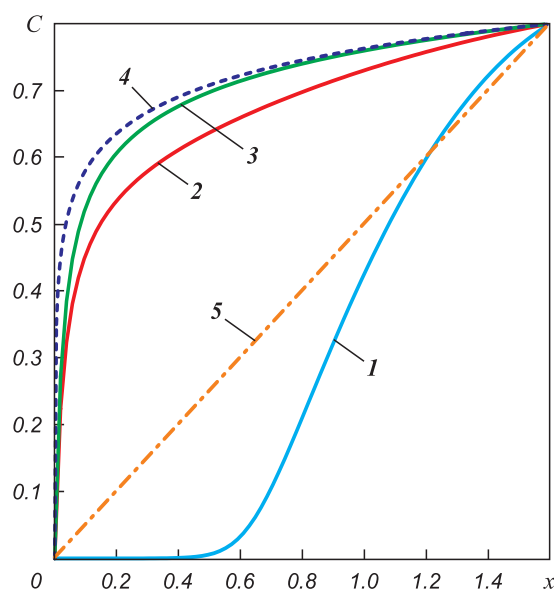


Fig. 3. Evolution of concentration profile for different moments of time

$t, \text{ s: } 1 - 0.04; 2 - 0.4; 3 - 2.0$

4 – tabulation of the formula (16) as the result of the solution of stationary non-linear equation
5 – stationary solution of classical diffusion equation

Рис. 3. Эволюция профиля концентрации в разные моменты времени

$t, \text{ с: } 1 - 0.04; 2 - 0.4; 3 - 2.0$

4 – результат табуляции формулы (16) решения стационарного нелинейного уравнения переноса
5 – стационарное решение классического уравнения диффузии

space. In other words, contrary to longheld belief based on the findings of previous theoretical works [4–6], there is no need to bring crucibles with molten silicon as close to the product surface as possible.

Calculations in two-dimensional formulation

The next most difficult stage is to conduct numerical simulation in a two-dimensional formulation. These calculations were also performed using the finite difference method. The classic explicit scheme was implemented [24]. During the calculations, a spatially uniform rectangular grid was used with a breakdown of 85:41 (85 nodes on the x coordinate between the melt mirror and the sample, 41 nodes on the y coordinate along the product surface). The larger number of nodes along the x axis is twice as large because the boundary layer has to be resolved near the product at the final stage of defining. The height of the sample is $H = 0.4$ m, the distance from the melt to the product is $L = 0.6$ m. The condition of impermeability was set for the upper and lower faces. As for the one-dimensional formulation, sampling schemes of first-order accuracy were used to approximate the time and space derivatives. To ensure the stability of the difference scheme, the derivatives with respect to the “flux” had first order accuracy and were calculated as “backward differences”. Now the silicon vapor transfer is described by the following non-stationary equation:

$$\frac{\partial C}{\partial t} - D_c \left[\left(\frac{\partial C}{\partial x} \right)^2 + \left(\frac{\partial C}{\partial y} \right)^2 \right] = D \left(\frac{\partial^2 C}{\partial x^2} + \frac{\partial^2 C}{\partial y^2} \right). \quad (17)$$

This equation includes two dimensional modifiers. Implicitly one of them is the convective transport parameter:

$$D_c = \frac{\kappa R T \rho_{\text{Si}}}{\eta \mu_{\text{Si}}}, \quad (18)$$

the second is the diffusion coefficient D ; their dimensions are the same, m^2/s . The first parameter describes the convective transport mechanism, while the second one is purely diffusive. Now (17) is a two-dimensional non-stationary partial differential equation with the same nonlinearity like the square of the concentration gradient. Calculations were performed for $L = 0.6$ m (array length), $H = 0.4$ m (sample height), $D_c = 57.1 \text{ m}^2/\text{s}$ (convective parameter), $D = 0.7 \text{ m}^2/\text{s}$ (diffusion coefficient). Initially, there are no silicon vapors in the space inside the retort. The constant concentration value corresponding to saturation is set on the right boundary and the condition of complete absorption is defined on the left boundary.

Results and discussion

The dynamics of the concentration front presented for different sampling times in Fig. 4 and 5 shows that the solution quite quickly reaches a steady stationary profile in the form of a convex surface, as in the one-dimensional case. At the initial stage lasting for milliseconds, silicon vapors are present on the right near the melt mirror only (Fig. 4). Further, the retort space fills with vapor and the concentration profile steepens. It should be noted that the concentration front remains flat all the time as it moves towards the product surface.

The calculations show that it takes ~ 0.5 s to reach the stationary profile. The largest derivative at the final stage of defining (Fig. 5) is still on the left boundary of the range of definition, i.e. on the product surface. It should be kept in mind that the flux density is proportional to the derivative value in this point. Thus, taking into account the independent convective transport of silicon vapor in addition to diffusive transport, we confirm the rather high rate of high temperature saturation of carbon material observed in experiments in the medium vacuum, which contradicts the value of the silicon flux from the classical diffusion equation.

Thus, it should be emphasized once again that a large sized product can not be sufficiently saturated

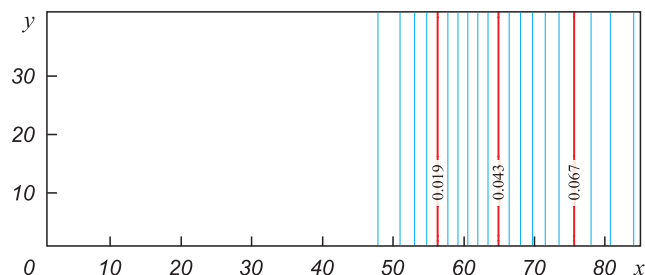


Fig. 4. Isolines of silicon vapour concentration at initial stage for $t = 0.004$ s

Рис. 4. Изолинии концентрации паров кремния на начальном этапе при $t = 0,004$ с

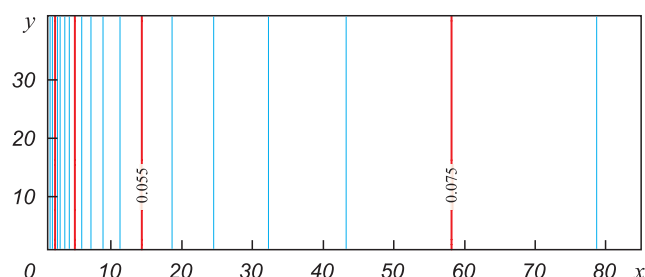


Fig. 5. Isolines of silicon vapour concentration at steady stage for $t = 1.0$ s

Рис. 5. Поле изолиний концентрации кремния на момент установления при $t = 1,0$ с

with silicon during the experiment only due to improper thermophysical mode of the entire process determined by the design features of the furnace.

These negative factors were earlier discussed in [15]. It was demonstrated that complete silicification of a product within a reasonable time is quite possible. In other words, the primary chemical reaction of carbon fiber carbonization and further condensation of silicon vapor in the pores of the material require a technique with more strict temperature control on the product surface rather than rearrangement of crucibles. If the sample surface is parallel to the melt mirror, as was assumed in the original formulation, the streamlines of silicon macroscopic motions are straight trajectories perpendicular to these surfaces. In this case, the wavefront of silicon vapor is stable, flat at any specific time and moves from the melt to the product so that the condition of homogeneity along the y coordinate can be used. However, in practice, in the gravity field, the surface of the melt mirror is always horizontal, since the silicon melt is in crucibles. At the same time, the product is placed vertically in the retort at some distance from the crucibles (there can be several of those). As a result, it is important to understand whether the nature of the silicon vapor distribution in the retort will change with more complex mutual arrangements of the source of silicon vapor and the absorbing surface.

Let us now analyze a more realistic configuration in the form of a rectangular retort shown in Fig. 6, with a silicon absorbing left vertical boundary 1 and a horizontal melt mirror 2 located at a distance of $2L/3$ from the sample. The melt surface itself has a size of $L/3$. The condition of impermeability is set for all other areas of the retort.

The calculation was performed on a 121:41 grid. The height of the sample was $H = 0.4$ m, the length of the range of definition was $L = 1.2$ m. At this proportion, the size of the melt mirror is $\Delta = 0.4$ m.

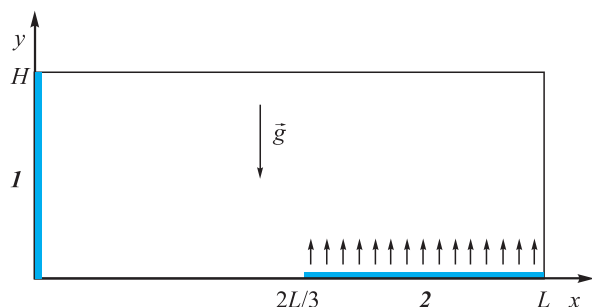


Fig. 6. Configuration for horizontal linear source of silicon vapour

Рис. 6. Конфигурация с горизонтальным линейным источником паров кремния

The results of the numerical simulation of the system in this configuration are presented in Fig. 7, 8 for two points in time: at the defining stage (at $t = 0.005$ s) and in the final state, close to stationary ($t = 0.1$ s). It can be seen that a stationary distribution is established in the system almost as quickly as in the previous configuration (within about 1 s). The calculations also show that silicon still occupies almost the entire working space inside the retort, with the exception of a relatively thin boundary layer near the absorbing surface area. Fig. 7, 8 show that silicon vapors propagate with almost the same intensity in all directions from the melt mirror. Silicon atoms need almost the same time to reach the product surface as in the previous case, when the surfaces were parallel to each other.

The calculation results show that the rarefied gas (argon), through which silicon vapors from the melt mirror penetrate to the sample, is not in itself the main restraining factor limiting the silicon mass transfer. In any case, different mutual arrangements of the silicon vapor source and the absorbing surface do not considerably change the time for reaching the stationary state.

A much more serious modifier in the problem is the relationship of the areas of the evaporating and absorbing surfaces. Let us now reduce the linear size of the surface on which evaporation takes place

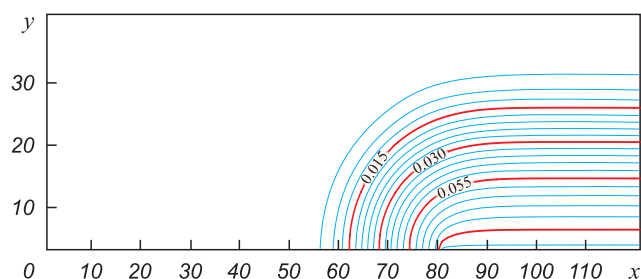


Fig. 7. The field of silicon concentration at initial stage $t = 0.005$ s for second configuration

Рис. 7. Поле концентрации кремния на начальном этапе для второй конфигурации при $t = 0,005$ с

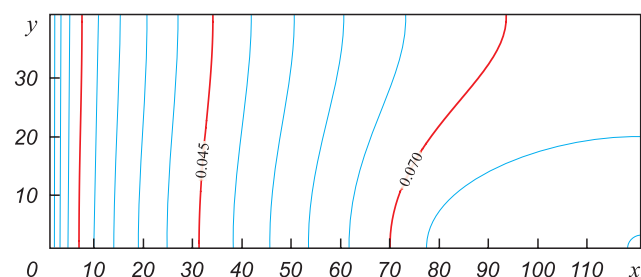


Fig. 8. The field of silicon concentration at stationary stage $t = 0.1$ s for second configuration

Рис. 8. Поле концентрации кремния на момент установления для второй конфигурации при $t = 0,1$ с

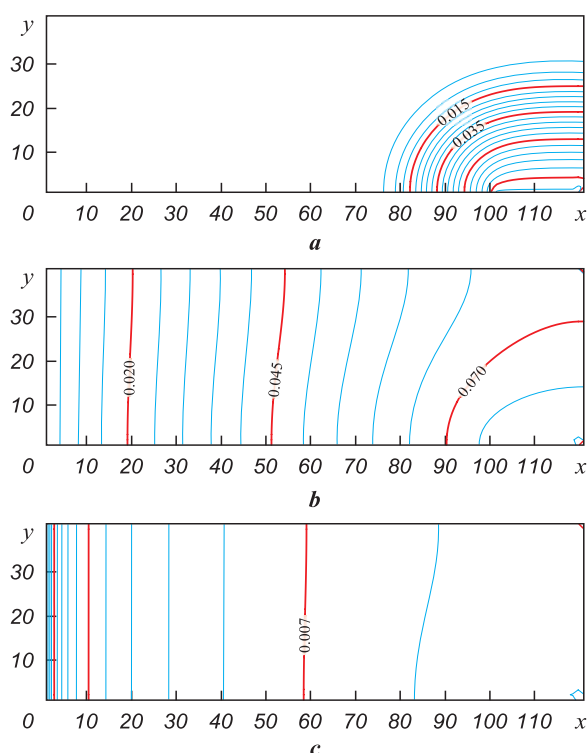


Fig. 9. The field of silicon concentration for horizontal source of the vapour at $\Delta = 0.2$ m

a – initial stage, $t = 0.005$ s
b – intermediate stage, $t = 0.1$ s
c – stationary stage, $t = 1.0$ s

Рис. 9. Поле концентрации кремния в случае горизонтального источника паров при $\Delta = 0,2$ м

a – начальный этап, $t = 0,005$ с
b – промежуточный этап, $t = 0,1$ с
c – момент установления, $t = 1,0$ с

to $\Delta = 0.2$ m, leaving unchanged the product height $H = 0.4$ m and the retort length $L = 1.2$ m. All other parameters will remain the same. Isolines and two-dimensional surfaces of the concentration field for this situation are presented in Fig. 9, *a*, *b*.

Fig. 9, *a* shows the initial moment of time, when the vapors have not yet spread to the entire volume. However, Fig. 9, *b* demonstrates that with smaller sizes of the melt mirror (twice the difference compared to the previous case) at $t = 0.1$ s, the stationary state is not reached yet.

Calculations show that the concentration profile now requires approximately twice as much time to set the stationary mode as in the previous case. The concentration field for the melt mirror at $t = 1.0$ s is shown in Fig. 9, *c*. Further on, the concentration field practically ceases to change over time. This result is physically understandable, since filling the space inside the retort with silicon vapor requires a certain time, and it is directly related to the amount of silicon evaporating per time unit from the source surface. As the melt

mirror length decreases, this time expectedly increases in proportion to it.

Conclusion

The analytical and numerical solutions of the generalized equation of silicon vapor diffusion during silicification of a porous carbon material obtained in the course of this study show that gaseous silicon quickly occupies almost the entire volume of the furnace working space. In other words, contrary to longheld belief based on the findings of previous theoretical works, there is no need to bring crucibles with molten silicon as close to the product surface as possible.

The results obtained from the two-dimensional formulation confirm the similar data received in the one-dimensional case. They show that the resistance of foreign gases to the silicon diffusion flow should certainly be present in the real production environment, but classical diffusion is not the only transfer mechanism. Generalization of the model taking into account additional convective transfer enables to solve the paradox of anomalously intense saturation of porous carbon material with silicon vapor in the experiment, in contradiction to earlier theoretical predictions.

References / Список литературы

1. Chawla Krishan K. Composite materials. Science and engineering. N.Y.: Springer, 2012. 542 p.
2. Shang J. Durability testing of composite aerospace materials based on a new polymer carbon fiber-reinforced epoxy resin. *Fluid Dynamics & Material Processing*. 2023;19(9): 2315–2327. <https://doi.org/10.32604/fdmp.2023.026742>
3. Shikunov S.L., Kurlov V.N. SiC-based composite materials obtained by siliconizing carbon matrices. *Journal of Technical Physics*. 2017;62(12):1869–1876. <https://doi.org/10.1134/S1063784127120222>
4. Garshin A.P., Kulik V.I., Matveev S.A., Nilov A.S. Modern technologies for the production of fiber-reinforced composite materials with a ceramic refractory matrix. *Novye Ogneupory (New Refractories)*. 2017;(4):20–35. (In Russ.).
 Гаршин А.П., Кулик В.И., Матвеев С.А., Нилов А.С. Современные технологии получения волокнисто-армированных композиционных материалов с керамической огнеупорной матрицей. *Новые огнеупоры*. 2017;(4):20–35.
5. Kulik V.I., Kulik A.V., Ramm M.S., Demin S.E. Development of a model and numerical study of the processes for production composites with a SiC matrix by vapour-phase silicization. In: *Proc. of the IV Intern. Conf. "Functional nanomaterials and high-purity substances"* (Suzdal, 1–5 Oct. 2012). Moscow: Institute of Metallurgy and Materials Science, 2012. P. 240–242. (In Russ.).
 Кулик В.И., Кулик А.В., Рамм М.С., Демин С.Е. Разработка модели и численное исследование процессов

- получения композитов с SiC матрицей методом паровозного силицирования. В сб. *матер. IV Междунар. конф. «Функциональные наноматериалы и высокочистые вещества»* (Суздаль, 1–5 октября 2012 г.). М.: ИМЕТ РАН, 2012. С. 240–242.
6. Kulik V.I., Kulik A.V., Ramm M.S., Demin S.E. Numerical study of gradient CVI processes for production of SiC-matrix composites. In: *Proc. of the V Intern. Conf. "Functional nanomaterials and high-purity substances"* (Suздal, 6–10 Oct. 2014). Moscow: Institute of Metallurgy and Materials Science, 2014. P. 128–129. (In Russ.).
Кулик В.И., Кулик А.В., Рамм М.С., Демин С.Е. Численное исследование градиентных газофазных процессов получения керамоматричных композитов с SiC матрицей. В сб. *матер. V Междунар. конф. «Функциональные наноматериалы и высокочистые вещества»* (Суздаль, 6–10 октября 2014 г.). М.: ИМЕТ РАН, 2014. С. 128–129.
 7. Shchurick A.G. Artificial carbon materials. Perm: UNIKM Publ., 2009. 342 p. (In Russ.).
Щурик А.Г. Искусственные углеродные материалы. Пермь: Изд-во УНИИМ, 2009. 342 с.
 8. Timofeev A.N., Razina A.S., Timofeev P.A., Bodyan A.G. Calculating the penetration depth of reaction in chemical gas-phase deposition of boron nitride within porous bodies. *Powder Metallurgy and Functional Coatings*. 2023;17(3): 38–46. <https://doi.org/10.17073/1997-308X-2023-3-38-46>
Тимофеев А.Н., Разина А.С., Тимофеев П.А., Бодян А.Г. Расчет глубины проникновения реакции при химическом газофазном осаждении нитрида бора в пористых телах. *Известия вузов. Порошковая металлургия и функциональные покрытия*. 2023;17(3):38–46. <https://doi.org/10.17073/1997-308X-2023-3-38-46>
 9. Pogozhev Yu.S., Potanin A.Yu., Rupasov S.I., Levashov E.A., Volkova V.A., Tashev V.P., Timofeev A.N. Structure, properties and oxidation resistance of prospective HfB₂-SiC based ceramics. *Russian Journal of Non-Ferrous Metals*. 2020;61(6):704–715. <https://doi.org/10.3103/S1067821220060164>
Погожев Ю.С., Потанин А.Ю., Рупасов С.И., Левашов Е.А., Волкова В.А., Ташев В.П., Тимофеев А.Н. Структура, свойства и окислительная стойкость перспективной керамики на основе HfB₂-SiC. *Известия вузов. Порошковая металлургия и функциональные покрытия*. 2020;(3):41–54. <https://doi.org/10.17073/1997-308X-2020-3-41-54>
 10. Demin V.A., Demina T.V., Maryshev B.S. Physical and mathematical model of gaseous silicon transfer during high-temperature siliconization of carbon composite materials. *Bulletin of Perm University. Physics*. 2022;(3):48–55. (In Russ.). <https://doi.org/10.17072/1994-3598-2022-3-48-55>
Демин В.А., Демина Т.В., Марышев Б.С. Физико-математическая модель переноса газообразного кремния в ходе высокотемпературного силицирования углеродных композитных материалов. *Вестник Пермского университета. Физика*. 2022;(3):48–55. <https://doi.org/10.17072/1994-3598-2022-3-48-55>
 11. Landau L.D., Lifshits E.M. Course of theoretical physics. Vol. 6. Hydrodynamics. Moscow: Fizmatlit, 2001. 736 p. (In Russ.).
Ландау Л.Д., Лифшиц Е.М. Курс теоретической физики. Т. 6. Гидродинамика. М.: Физматлит, 2001. 736 с.
 12. Sevast'yanov V.G., Nosatenko P.Ya., Gorskiy V.V., Ezhov Yu.S., Sevast'yanov D.V., Simonenko E.P., Kuznetsov N.T. Experimental and theoretical determination of the saturation vapour pressure of silicon in a wide range of temperatures. *Russian Journal of Inorganic Chemistry*. 2010;13(55):2073–2088. <https://doi.org/10.5702/massspec.47.49>
 13. Tomooka T., Shoji Y., Matsui T. High temperature vapor pressure of Si. *Journal of the Mass Spectrometry of Japan*. 1999;47(1):49–53.
 14. Hirschfelder J.O., Curtiss Ch.F., Bird R.B. Molecular theory of gases and liquids. N.Y.: Wiley & Sons, 1954. 1219 p.
Гиршфельдер Дж., Кертисс Ч., Берд Р. Молекулярная теория газов и жидкостей. М.: Изд-во иностр. лит-ры, 1961. 929 с.
 15. Ageeva M.V., Demin V.A. Physical model and numerical simulation of high-temperature silicification of carbon composite material. *Philosophical Transactions of the Royal Society A*. 2023;381:20220083. <https://doi.org/10.1098/rsta.2022.0083>
 16. Matsumoto M. Molecular dynamics simulation of interphase transport at liquid surfaces. *Fluid Phase Equilibria*. 1996;(125):195–203.
 17. Matsumoto M. Molecular dynamics of fluid phase change. *Fluid Phase Equilibria*. 1998;(144):307–314.
 18. Bond M., Struchtrup H. Mean evaporation and condensation coefficients based on energy dependent condensation probability. *Physical Review E* 70. 2004;061605. <https://doi.org/10.1103/PhysRevE.70.061605>
 19. Schwabl Fr. Statistical mechanics. Berlin: Springer, 2006. 577 p.
 20. Nield D.A., Bejan A. Convection in porous media. N.Y.: Springer, 2006. 654 p.
 21. Demin V.A., Petukhov M.I., Ponomarev R.S., Topova A.V. Nonlinear sorptive effects during the pumping of nano-fluid through porous medium. *Bulletin of Perm University. Physics*. 2021;(1):49–58. (In Russ.). <https://doi.org/10.17072/1994-3598-2021-1-49-58>
Демин В.А., Петухов М.И., Пономарев Р.С., Топова А.В. О роли анизотропии и нелинейных диффузионных эффектов при формировании волноводов в кристалле ниобата лития. *Вестник Пермского университета. Физика*. 2021;(1):49–58. <https://doi.org/10.17072/1994-3598-2021-1-49-58>
 22. Vohra S.T., Mickelson A.R., Asher S.E. Diffusion characteristics and waveguiding properties of proton exchanged and annealed LiNbO₃ channel waveguides. *Journal of Applied Physics (AIP)*. 1989;66(11):5161–5174. <https://doi.org/10.1063/1.343751>
 23. Korn G.A., Korn T.M. Mathematical handbook for scientists and engineers. Dover Publications, 2013. 1615 p.
Корн Г., Корн Т. Справочник по математике для научных работников и инженеров. М.: Наука, 1984. 831 с.
 24. Samarskii A.A. The theory of difference schemes. N.Y.: Marcel Dekker, Inc., 2001. 762 p.
Самарский А.А. Теория разностных схем. М.: Наука, 1989. 616 с.

Information about the Authors



Maria V. Ageeva – Research Engineer at the Laboratory of Underground Sequestration of Carbon at the Institute of Continuous Media Mechanics of the UB RAS; Master's Student at the Perm State National Research University (PSNRU)

ORCID: 0009-0008-6671-2787

E-mail: gretskioreshek0@mail.ru

Vitaly A. Demin – Dr. Sci. (Phys.-Math.), Prof., Head of Theoretical Physics Department at the PSNRU; Prof. at the Department of General Physics at the Perm National Research Polytechnic University

ORCID: 0000-0002-9765-7695

E-mail: demin@psu.ru

Tatyana V. Demina – Research Engineer at the Laboratory of Underground Sequestration of Carbon at the Institute of Continuous Media Mechanics of the UB RAS; Postgraduate Student at the PSNRU

ORCID: 0009-0006-5600-1354

E-mail: demina-tatyana99@yandex.ru

Сведения об авторах

Мария Викторовна Агеева – инженер-исследователь лаборатории подземной утилизации углерода Института механики сплошных сред (ИМСС) УрО РАН; магистр Пермского государственного национального исследовательского университета (ПГНИУ)

ORCID: 0009-0008-6671-2787

E-mail: gretskioreshek0@mail.ru

Виталий Анатольевич Демин – д.ф.-м.н., профессор, заведующий кафедрой теоретической физики ПГНИУ; профессор кафедры общей физики Пермского национального исследовательского политехнического университета

ORCID: 0000-0002-9765-7695

E-mail: demin@psu.ru

Татьяна Витальевна Демина – инженер-исследователь лаборатории подземной утилизации углерода ИМСС УрО РАН; аспирант кафедры теоретической физики ПГНИУ

ORCID: 0009-0006-5600-1354

E-mail: demina-tatyana99@yandex.ru

Contribution of the Authors



V. A. Demin – determined the statement of the problem, participated in the obtaining of the analytical solution, wrote the article, participated in the discussion of the results.

M. V. Ageeva – participated in the creation of computational code, conducted numerical simulation, wrote the article, participated in the discussion of the results.

T. V. Demina – participated in the obtaining of the analytical solution, created computational code, conducted numerical simulation, wrote the article, participated in the discussion of the results.

Вклад авторов

В. А. Демин – постановка задачи, участие в получении аналитического решения задачи, написание статьи, участие в обсуждении результатов.

М. В. Агеева – участие в написании вычислительного кода, участие в проведении численного моделирования, написание статьи, участие в обсуждении результатов.

Т. В. Демина – участие в получении аналитического решения, участие в написании вычислительного кода, участие в проведении численного моделирования, написание статьи, участие в обсуждении результатов.

Received 27.07.2023

Revised 23.10.2023

Accepted 26.10.2023

Статья поступила 27.07.2023 г.

Доработана 23.10.2023 г.

Принята к публикации 26.10.2023 г.



UDC 621.762

<https://doi.org/10.17073/1997-308X-2024-3-62-70>

Research article

Научная статья



Features of obtaining TiNi alloy samples from commercial powders with high oxygen content using the SLM technique

E. M. Farber , E. V. Borisov, A. A. Popovich

Peter the Great St. Petersburg Polytechnic University
29 Polytekhnicheskaya Str., St. Petersburg 195251, Russia

d.farber2010@yandex.ru

Abstract. Additive technologies, in particular selective laser melting (SLM), enable to manufacture the products with complex geometries. The SLM technique can help to effectively expand the titanium nickelide scope of application. However, SLM is a complex process – numerous factors significantly affect the characteristics of the resulting alloy. When the SLM technique is used, as the material is subject to laser processing, the content of nickel in the alloy drops due to evaporation, which can lead to changes in the temperatures of martensitic transformations. This impact on the resulting alloy characteristics can be regulated by changing the parameters of the SLM process. The objective of our research was to develop the processing methods for manufacturing samples from two commercial TiNi alloy powders using the SLM technique and to analyze the factors causing defects in the obtained samples. At the same time, processing methods with low values of volumetric energy density were used to reduce possible evaporation of nickel during printing. The initial powders were examined for the presence of impurities or other factors affecting the quality of the manufactured samples. The processing method A4 that we have developed for powder 1 enables to obtain a defect-free sample with the density of 6.45 g/cm³. It was found that none of the processing methods used enabled to obtain a defect-free sample from powder 2 due to presence of a large amount of oxygen impurities, including in particular Ti₄Ni₂O_x secondary phase, which leads to embrittlement and destruction of the samples. Therefore, high content of oxygen in the initial powders has a negative impact on the quality of the samples manufactured using the SLM technique.

Keywords: selective laser melting, TiNi alloy, titanium nickelide, impurities, defects, defect-free samples

For citation: Farber E.M., Borisov E.V., Popovich A.A. Features of obtaining TiNi alloy samples from commercial powders with high oxygen content using the SLM technique. *Powder Metallurgy and Functional Coatings*. 2024;18(3):62–70.
<https://doi.org/10.17073/1997-308X-2024-3-62-70>

Особенности получения образцов сплава TiNi методом СЛС из коммерческих порошков с повышенным содержанием кислорода

Э. М. Фарбер , Е. В. Борисов, А. А. Попович

Санкт-Петербургский политехнический университет Петра Великого
Россия, 195251, г. Санкт-Петербург, ул. Политехническая, 29

d.farber2010@yandex.ru

Аннотация. Аддитивные технологии, в частности метод селективного лазерного плавления (СЛС, или SLM), позволяют изготавливать изделия со сложной геометрией. С помощью СЛС можно эффективно расширить области применения никелида титана. Однако процесс СЛС является комплексным – множество факторов оказывают серьезное влияние на характеристики получаемого сплава. В процессе лазерной обработки материала в технологии СЛС происходит снижение содержания никеля в составе сплава за счет испарения, что может приводить к изменению температур мартенситных превращений.

Регулирование данного влияния на результирующие характеристики сплава возможно за счет изменения параметров процесса СЛС. Цель работы состояла в разработке технологических режимов изготовления образцов из двух коммерческих порошков сплава TiNi методом СЛС и анализе факторов, влияющих на наличие дефектов в полученных образцах. При этом для снижения возможного испарения никеля в процессе печати применялись технологические режимы с невысокими значениями объемной плотности энергии. Исходные порошки исследованы на наличие примесей или иных факторов, влияющих на качество изготавливаемых образцов. В результате проведенного исследования для используемого порошка 1 разработан технологический режим А4, с помощью которого изготовлен бездефектный образец, плотность которого составила 6,45 г/см³. Установлено, что ни один из применяемых режимов не позволил получить бездефектный образец из порошка 2 ввиду наличия в нем большого количества примесей кислорода, в частности вторичной фазы Ti₄Ni₂O_x, приводящей к охрупчиванию и разрушению образцов. Следовательно, высокое содержание кислорода в исходных порошках отрицательно влияет на результаты изготовления образцов методом СЛС.

Ключевые слова: селективное лазерное сплавление, сплав TiNi, никелид титана, примеси, дефекты, бездефектные образцы

Для цитирования: Фарбер Э.М., Борисов Е.В., Попович А.А. Особенности получения образцов сплава TiNi методом СЛС из коммерческих порошков с повышенным содержанием кислорода. *Известия вузов. Порошковая металлургия и функциональные покрытия*. 2024;18(3):62–70. <https://doi.org/10.17073/1997-308X-2024-3-62-70>

Introduction

Titanium nickelide (TiNi) is one of the most well-known smart materials famous for superelasticity and its ability to exhibit shape memory effect. It is widely used in the aerospace and automotive industries, medicine, microelectronics and other fields of science and technology [1–5]. Additive technologies, in particular the selective laser melting (SLM) method, enable to create highly complex geometries [6] and can dramatically increase applications of titanium nickelide. However, SLM is a complex process – numerous factors significantly affect the characteristics of the resulting alloy.

It is known that when the SLM technique is used for laser processing of the material, the nickel content in the alloy drops due to evaporation as the boiling points of nickel and titanium differ: nickel boils at 2913 °C, while titanium has a boiling point of 3287 °C [7–12]. Additionally, nickel has a higher partial pressure than titanium, and therefore nickel is more volatile at elevated temperatures [7]. It has been established that changes in the nickel content in the alloy can result in changing temperatures of martensitic transformations – the main parameters indicating that the functional properties of the alloy can manifest themselves at certain temperatures [13–15].

This impact on the resulting alloy characteristics can be regulated by changing the parameters of the SLM process – volumetric energy density (E) and its determining factors – scanning speed, distance between laser passes, laser power and layer thickness. It was found that as the E value increases, so does nickel evaporation during the SLM process [16–18]. Some researchers point out that an average volumetric energy density of more than 100 J/mm³ is required to obtain dense products from nitinol using the SLM technique [3; 18–20]. At the same time, in some stu-

dies, defect-free samples were obtained with lower E values [11; 21; 22]. Such a spread in the values of volumetric energy density may indicate that the quality of the initial powder (presence of impurities or secondary phases in it) affects the characteristics of the resulting products.

Based on the above, the objective of our research was to develop the processing methods for manufacturing samples from two commercial TiNi alloy powders with enhanced oxygen content using the SLM technique and to analyze the factors causing defects in the obtained samples. At the same time, processing methods with low values of volumetric energy density were used to reduce the possible evaporation of nickel during printing [17]. The initial powders were examined for the presence of impurities or other factors affecting the quality of the manufactured samples. The results obtained will, in the future, enable to improve the quality of the resulting products and to simplify the selection of TiNi alloy powders, as well as the development of processing methods for manufacturing products from these powders.

Materials and methods

In this study, we used two commercially produced spherical powders (1 and 2, respectively) of TiNi alloy with similar chemical composition Ti₄₉Ni₅₁ (at. %). The chemical composition of these powders is presented in Table 1.

The cylindrical samples with a diameter of 10 mm and a height of 60 mm were fabricated for the study. Table 2 shows 4 methods of their production using the SLM technique. The processing methods with low values of volumetric energy density – $E < 100$ J/mm³ – were selected to minimize nickel evaporation during the SLM process. The E values are changed by gradually reducing the scanning speed in increments

Table 1. Chemical composition (at. %) of the powders under study

Таблица 1. Химический состав (ат. %) исследуемых порошков

Powder	Ti	Ni	O	N	C
1	48.63	51.03	0.14	0.01	0.19
2	48.56	50.96	0.29	0.01	0.18

of 175 mm/s. The laser power, distance between passes, and layer thickness remained the same for all processing methods. For convenience, the samples manufactured using a certain processing method from powder 1 will hereinafter be marked as A1/1, A2/1, A3/1 and A4/1, and those from powder 2 – A1/2, A2/2, A3/2 and A4/2.

The SLM process was conducted on the SLM280HL printer (SLM Solutions GmbH, Germany), which uses an ytterbium fiber laser with a maximum power of 400 W, has a wavelength of 1070 nm, the minimum laser beam diameter of 80 μm and the maximum scanning speed of 15 m/s. The process was implemented in an inert gas atmosphere (argon). The chemical composition of the initial powders and the resulting samples was visually analyzed and determined using Tescan Mira 3 LMU scanning electron microscope (SEM) (Tescan, Brno, Czech Republic) with an energy-dispersive X-ray spectroscopy module “EDX X-max 80” (Oxford Instruments, Abingdon, United Kingdom). The microstructure of the obtained samples was evaluated on a Leica DMI 5000 light optical microscope (Leica Microsystems, Germany). The granulometric composition of the powders was assessed using an Analysette 22 NanoTec particle size analyzer (Fritsch, Germany). The phase composition of the initial powder and the resulting samples was determined on a Bruker D8 Advance X-ray diffractometer (Bruker, Bremen, Germany).

Results and discussion

Fig. 1 shows the granulometric composition of the powders under study. Volume distribution frac-

tions for powder 1 – $d_{10} = 28.7 \mu\text{m}$, $d_{50} = 48.1 \mu\text{m}$, $d_{90} = 76.5 \mu\text{m}$, for powder 2 – $d_{10} = 15.1 \mu\text{m}$, $d_{50} = 29 \mu\text{m}$, and $d_{90} = 52.6 \mu\text{m}$.

Fig. 2 demonstrates SEM images of the powders under study.

Fig. 3 shows the samples made from powder 1 using various processing methods; Fig. 4 demonstrates the samples from powder 2. In Fig. 3, we see that the samples manufactured at a lower volumetric energy density (A1/1, A2/1) have multiple defects in the form of cracks. As E was increased by reducing the scanning speed, first, the number of visually detectable cracks (sample A3/1) decreased, and as E reached 90 J/mm³ (sample A4/1), no cracks were detected by visual inspection. The density of the resulting sample A4/1 was 6.45 g/cm³. The nickel content in the defect-free sample A4/1 (50.85 at. %) dropped by 0.18 at. % against the original powder 1. The results of our study are generally consistent with those previously obtained in [17].

The samples from powder 2, which were manufactured using processing methods with low volumetric energy density, are severely deformed and partially destroyed (see Fig. 4). The increase in E resulted

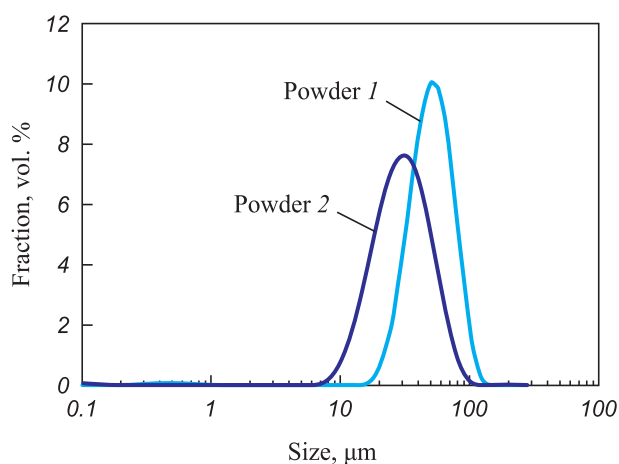


Рис. 1. Гранулометрический состав исследуемых порошков

Fig. 1. Granulometric composition of the powders under study

Table 2. Processing methods for manufacturing samples

Таблица 2. Технологические режимы изготовления образцов

Method	Power, W	Scanning rate, mm/s	Distance between laser passes, mm	Layer thickness, mm	Volumetric energy density, J/mm ³
A1	200	1450	0.08	0.03	57
A2	200	1275	0.08	0.03	65
A3	200	1100	0.08	0.03	75
A4	200	925	0.08	0.03	90

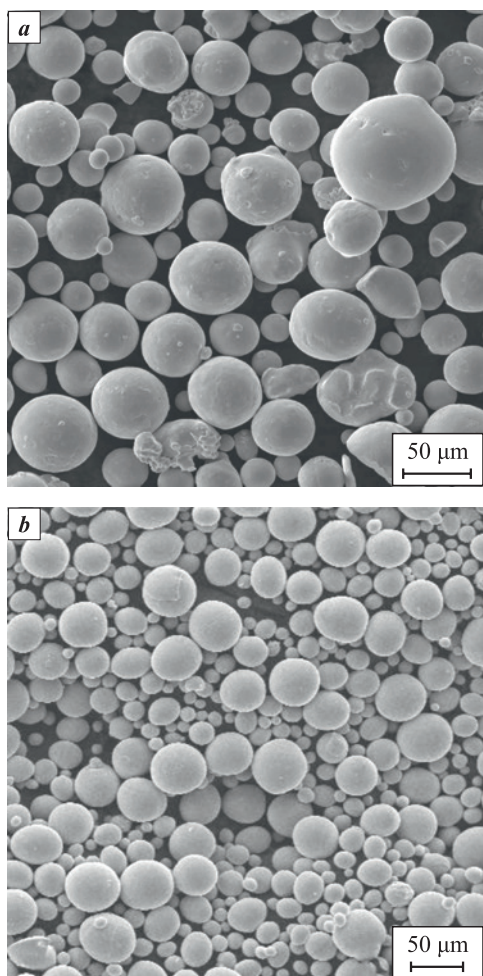


Fig. 2. SEM images of the powders used
a – powder 1, *b* – powder 2

Рис. 2. СЭМ-изображения используемых порошков
a – порошок 1, *b* – порошок 2

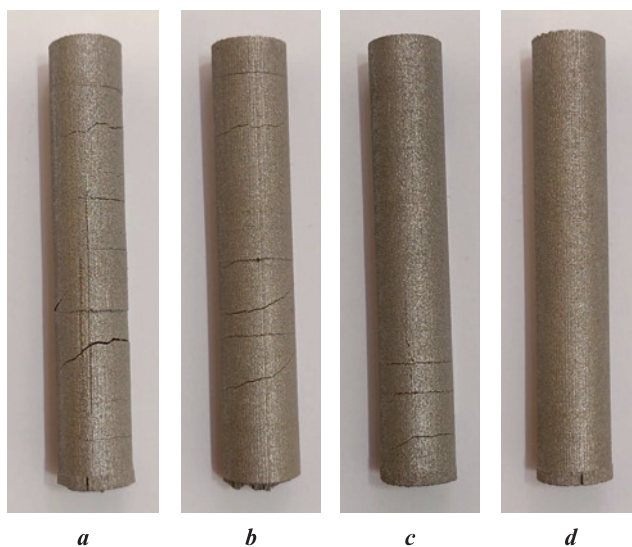


Fig. 3. Samples made from powder 1
a – A1/1, *b* – A2/1, *c* – A3/1, *d* – A4/1

Рис. 3. Образцы, изготовленные из порошка 1
a – A1/1, *b* – A2/1, *c* – A3/1, *d* – A4/1

in a decreased level of deformation; however, even at $E = 90 \text{ J/mm}^3$ (sample A4/2), multiple cracks were observed along the entire length of the sample.

The large number of cracks in the samples is associated primarily with the features of the SLM process, namely with residual stresses caused by a high temperature gradient during the samples manufacture due to rapid heating, melting and, subsequently, rapid cooling and solidification of the material, as well as possible presence of defects in the form of micropores [23–25]. An increase in the scanning speed during the samples



Fig. 4. Samples made from powder 2
a – A1/2, *b* – A2/2, *c* – A3/2, *d* – A4/2

Рис. 4. Образцы, изготовленные из порошка 2
a – A1/2, *b* – A2/2, *c* – A3/2, *d* – A4/2

manufacture causes an expected drop in volumetric energy density. When the energy density is insufficient, micropores and discontinuities emerge in the sample structure due to the small size of the molten bath and presence of unmelted powder particles [3]. These defects are stress concentrators that contribute to active propagation of cracks in the samples. This phenomenon was observed in the samples made from powder 1. When the processing method A1 was used with a scanning speed of 1450 mm/s, a large number of cracks was registered over the entire area of the sample; and when the scanning speed was reduced to 925 mm/s, cracks were not visually detected.

Fig. 5 shows the microstructure of samples from powder 2 with various defects. We can see multiple cracks at the edges of the sample (Fig. 5, *a* and *b*) and also the ones running through the entire sample (Fig. 5, *c*), up to 200 μm thick. In addition, spherical and non-spherical pores of various sizes (some larger than 100 μm) are visible. Some cracks penetrate through pores and propagate in them (Fig. 5, *a* and *b*).

The samples made from powder 2 underwent rather severe deformations, which is indicative of additional

factors contributing to crack formation, along with the scanning speed. One of the hypothetical causes may be the presence of a large amount of oxygen in the initial powder 2 (more than in powder 1), which may also be present in the form of $\text{Ti}_4\text{Ni}_2\text{O}_x$ secondary phase. In powder 2 under study, the oxygen content was initially 2 times higher than in powder 1. The $\text{Ti}_4\text{Ni}_2\text{O}_x$ secondary phase is a Ti_2Ni phase with oxygen in the solid solution. The presence of this phase has a negative impact on the alloy and can lead to embrittlement and destruction of samples [26; 27]. It was noted [28] that initially cracks emerge in this very $\text{Ti}_4\text{Ni}_2\text{O}_x$ secondary phase. Therefore, a large amount of this phase in the composition of the initial powder can lead to increased cracking when the samples are manufactured. Another assumption is that a large amount of oxygen contributes to the formation of these secondary phases during the sample preparation process.

To determine the reasons more clearly, a cross-section of powder 2 was prepared. Fig. 6 shows SEM images of particles of powder 2 at high magnification. It is clearly visible that the particles contain dark inclusions, which may be $\text{Ti}_4\text{Ni}_2\text{O}_x$ secondary phases.

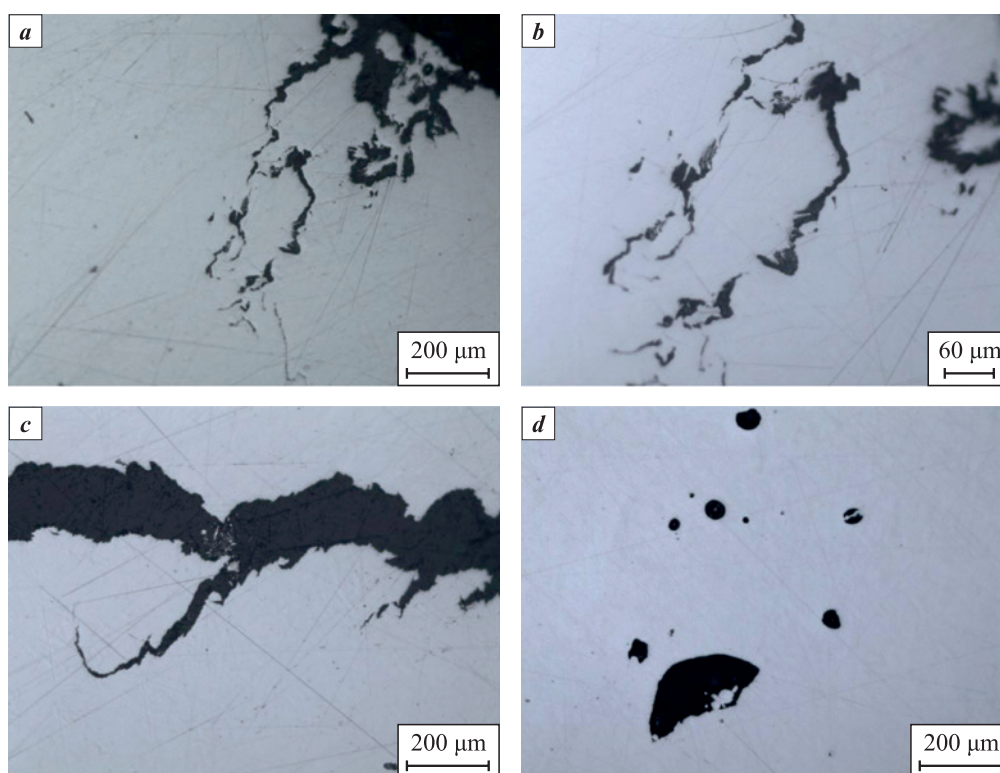


Fig. 5. Defects in the samples made from powder 2 using the SLM technique
a – cracks and pores at the edge of the sample; *b* – cracks penetrating through pores;
c – crack running through the entire thickness of the sample, *d* – spherical pores

Рис. 5. Дефекты в образцах, изготовленных из порошка 2 методом СЛС

a – трещины и поры с краю образца; *b* – трещины, проходящие через поры;
c – трещина, пересекающая всю толщину образца, *d* – сферические поры

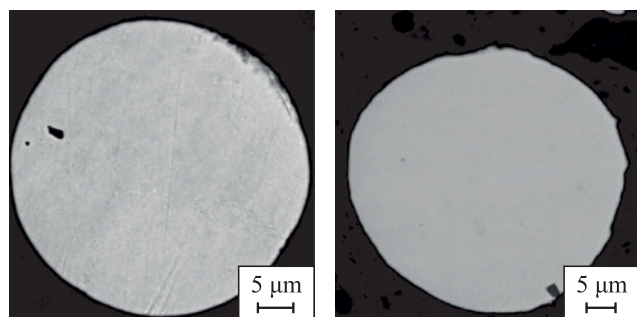


Fig. 6. SEM image at high magnification of powder particles 2 in the BSE mode with inclusions – secondary phases

Рис. 6. СЭМ-изображения с большим увеличением в режиме BSE частиц порошка 2 с наличием включений – вторичных фаз

Fig. 7 shows the results of X-ray phase analysis of powder 2 and a sample made from it.

The X-ray diffraction pattern of the sample (Fig. 7, b) shows that the lines of the B2 phase have widened

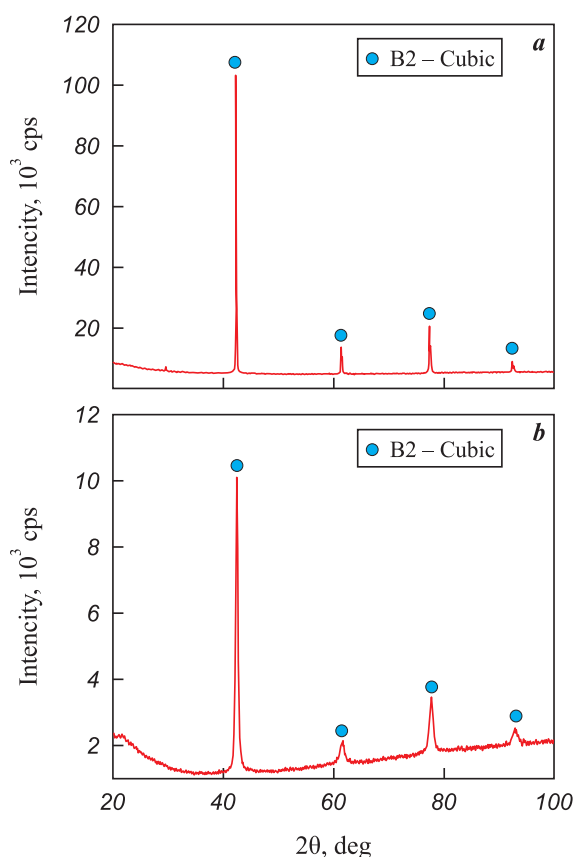


Fig. 7. X-ray diffraction patterns

a – powder 2

b – sample made from powder 2 using the SLM technique

Рис. 7. Рентгеновские дифрактограммы

a – порошок 2

b – образец, изготовленный из порошка 2 методом СЛС

Table 3. Oxygen content in the samples

Таблица 3. Содержание кислорода в образцах

Sample	Oxygen content, at. %
A4/1	0.26
A4/2	0.40

severalfold compared to the original powder. This widening is attributed to increased dislocation density and micro stresses. No secondary phases were detected in the composition of either the powder or the sample. This may suggest an extremely low content of the indicated $Ti_4Ni_2O_x$ phases in the composition of both powder 2 and the samples made from it – below the detection limit of the research method used. Moreover, as the lines of the B2 phase have widened, the coordinates of all the sought $Ti_4Ni_2O_x$ lines (39.0, 41.4 and 45.2) lie at the (110) B2 peak base. It can be assumed that the sample contains the indicated $Ti_4Ni_2O_x$ secondary phase, but its detection is hampered.

In general, based on the results obtained, we can confidently state that the increased oxygen content in the initial powder negatively affects the quality of the resulting samples, especially when they are manufactured with low values of volumetric energy density. To confirm this conclusion, we investigated the chemical composition of samples A4/1 and A4/2 for oxygen content. The results are presented in Table 3. It was found that the oxygen content in sample A4/2 reached 0.4 at. %, which is 0.14 at. % more than in sample A4/1. The oxygen level in the samples is higher than in the powder due to the capture of oxygen during the samples manufacture using the SLM technique. It can be noted that as the same processing method A4 was used, the oxygen content being high both in the original powder and in the manufactured sample, the sample from powder 1 had no defects, while that from powder 2 had numerous cracks. It confirms the assumption that oxygen content affects formation of defects in the samples manufactured using the SLM technique.

Conclusions

1. Having tested the processing methods, we came to conclusion that the defect-free sample from powder 1 can be obtained using the processing method A4. The density of the resulting sample A4/1 was 6.45 g/cm³. Defect-free samples from powder 1 cannot be obtained using the processing methods with lower volumetric energy density.

2. We failed to obtain a defect-free sample from powder 2 using any of the processing methods. Probably

methods with higher values of volumetric energy density are required to obtain defect-free samples from this powder.

3. The presence of a large amount of oxygen impurities in powder 2 is one of the factors that hampered us to obtain defect-free samples when using the indicated processing methods. This is attributed to $Ti_4Ni_2O_x$ secondary phase present in the powder composition, which leads to embrittlement and destruction of the samples. That is, the increased oxygen content in the initial powders negatively affects the quality of samples manufactured using the SLM technique.

4. The study of the microstructure of samples obtained from powder 2 revealed the presence of spherical and non-spherical pores and cracks of various sizes. It was found that cracks propagate directly through the detected pores.


References / Список литературы

- Horvay K., Schade C. Development of nitinol alloys for additive manufacturing. In: *Contributed papers from materials science and technology*. USA, Ohio, Columbus: Greater Columbus Convention Center, 2018. P. 63–70. https://doi.org/10.7449/2018mst/2018/mst_2018_63_70
- Borisov E., Starikov K., Popovich A., Tihonovskaya T. Investigation of the possibility of tailoring the chemical composition of the NiTi alloy by selective laser melting. *Metals (Basel)*. 2021;11(9):1–11. <https://doi.org/10.3390/met11091470>
- Chernyshikhin S.V., Pelevin I.A., Karimi F., Shishkovsky I.V. The study on resolution factors of LPBF technology for manufacturing superelastic NiTi endodontic files. *Materials (Basel)*. 2022;15(19):6556. <https://doi.org/10.3390/ma15196556>
- Chernyshikhin S.V., Panov D.V., Van Tuan T., Ozherelkov D.Y., Sheremetyev V.A., Shishkovsky I.V. Laser polishing of nickel-titanium shape memory alloy produced via laser powder bed fusion. *Metals and Materials International*. 2023;29(10):3024–3038. <https://doi.org/10.1007/s12540-023-01432-8>
- Dadbakhsh S., Speirs M., Kruth J.P., Van Humbeeck J. Influence of SLM on shape memory and compression behaviour of NiTi scaffolds. *CIRP Annals*. 2015;64(1): 209–212. <https://doi.org/10.1016/j.cirp.2015.04.039>
- Ehsan Saghaian S., Nematollahi M., Toker G., Hinojos A. Effect of hatch spacing and laser power on microstructure, texture, and thermomechanical properties of laser powder bed fusion (L-PBF) additively manufactured NiTi. *Optics & Laser Technology*. 2022;149:107680. <https://doi.org/10.1016/j.optlastec.2021.107680>
- Elahinia M., Moghaddam N.S., Andani M.T., Amerinatanzi A., Bimber B.A., Hamilton R.F. Fabrication of NiTi through additive manufacturing: A review. *Progress in Materials Science*. 2016;83(12):630–663. <https://doi.org/10.1016/j.pmatsci.2016.08.001>
- Farber E., Zhu J.-N., Popovich V.A. A review of NiTi shape memory alloy as a smart material produced by additive manufacturing. *Materials Today: Proceedings*. 2020;30: 761–767. <https://doi.org/10.1016/j.matpr.2020.01.563>
- Jalali M., Mohammadi K., Movahhedy M.R., Karimi F., Sadrnezhaad S.K., Chernyshikhin S.V., Shishkovsky I.V. SLM additive manufacturing of NiTi porous implants: A review of constitutive models, finite element simulations, manufacturing, heat treatment, mechanical, and biomedical studies. *Metals and Materials International*. 2023;29(9):2458–2491. <https://doi.org/10.1007/s12540-023-01401-1>
- Kai W.-Y., Chang K.-C., Wu H.-F., Chen S.-W., Yeh A.-C. Formation mechanism of Ni₂Ti₄O in NiTi shape memory alloy. *Materialia*. 2019;5:100194. <https://doi.org/10.1016/j.mtla.2018.100194>
- Kang G., Song D. Review on structural fatigue of NiTi shape memory alloys: Pure mechanical and thermo-mechanical ones. *Theoretical and Applied Mechanics Letters*. 2015;5(6):245–254. <https://doi.org/10.1016/j.taml.2015.11.004>
- Ma J., Franco B., Tapia G., Karayagiz K., Johnson L., Liu J., Arroyave R., Karaman I., Elwany A. Spatial control of functional response in 4D-printed active metallic structures. *Scientific Reports*. 2017;7(1):46707. <https://doi.org/10.1038/srep46707>
- Mahmoudi M., Tapia G., Franco B., Ma J., Arroyave R., Karaman I., Elwany A. On the printability and transformation behavior of nickel-titanium shape memory alloys fabricated using laser powder-bed fusion additive manufacturing. *Journal of Manufacturing Processes*. 2018;35:672–680. <https://doi.org/10.1016/j.jmapro.2018.08.037>
- Meier H., Haberland C., Frenzel J. Structural and functional properties of NiTi shape memory alloys produced by Selective Laser Melting. In: *Innovative developments in virtual and physical prototyping: Proc. of the 5th Inter. Conf. on advanced research in virtual and rapid prototyping* (Leiria, Portugal, 28 Sept.–1 Oct. 2011). London: CRC Press, 2011. P. 291–296. <https://doi.org/10.1201/b11341-47>
- Melnikova M.A., Melnikov D.M., Kolchanov D.S. Selective laser melting: Application and formation features of three-dimensional structural engineering elements. *Photonics Russia*. 2017;(2):42–49. <https://doi.org/10.22184/1993-7296.2017.62.2.42.49>
 Мельникова М.А., Колчанов Д.С., Мельников Д.М. Селективное лазерное плавление: применение и особенности формирования трехмерных конструктивных технологических элементов. *Фотоника*. 2017;(2):42–49. <https://doi.org/10.22184/1993-7296.2017.62.2.42.49>
- Mentz J., Bram M., Buchkremer H.P., Stöver D. Improvement of mechanical properties of powder metallurgical NiTi shape memory alloys. *Advanced Engineering Materials*. 2006;8(4):247–252. <https://doi.org/10.1002/adem.200500258>
- Mentz J., Frenzel J., Wagner M.F.X., Neuking K., Eggele G., Buchkremer H.P., Stöver D. Powder metallurgical processing of NiTi shape memory alloys with elevated

- transformation temperatures. *Materials Science and Engineering: A*. 2008;491(1–2):270–278.
<https://doi.org/10.1016/j.msea.2008.01.084>
18. Mohd Jani J., Leary M., Subic A., Gibson M.A. A review of shape memory alloy research, applications and opportunities. *Materials & Design*. 2014;56:1078–1113.
<https://doi.org/10.1016/j.matdes.2013.11.084>
 19. Parvizi S., Hashemi S.M., Asgarinia F., Nematollahi M., Elahinia M. Effective parameters on the final properties of NiTi-based alloys manufactured by powder metallurgy methods: A review. *Progress in Materials Science*. 2021;117:100739.
<https://doi.org/10.1016/j.pmatsci.2020.100739>
 20. Saedi S., Moghaddam N.S., Amerinatanzi A., Elahinia M., Karaca H.E. On the effects of selective laser melting process parameters on microstructure and thermomechanical response of Ni-rich NiTi. *Acta Materialia*. 2018;144:552–560.
<https://doi.org/10.1016/j.actamat.2017.10.072>
 21. Saedi S., Saghaian S.E., Jahadkbar A., Moghaddam N.S., Taheri Andani M., Saghaian S.M., Lu Y.C., Elahinia M., Karaca H.E. Shape memory response of porous NiTi shape memory alloys fabricated by selective laser melting. *Journal of Materials Science: Materials in Medicine*. 2018;29(4):1–12.
<https://doi.org/10.1007/s10856-018-6044-6>
 22. Safaei K., Abedi H., Nematollahi M., Kordizadeh F., Dabbaghi H., Bayati P., Javanbakht R., Jahadkbar A., Elahinia M., Poorganji B. Additive manufacturing of NiTi shape memory alloy for biomedical applications: Review of the LPBF process ecosystem. *JOM: The Journal of the Minerals, Metals & Materials*. 2021;73(12):3771–3786.
<https://doi.org/10.1007/s11837-021-04937-y>
 23. Song B., Zhao X., Li S., Han C., Wei Q., Wen S., Liu J., Shi Y. Differences in microstructure and properties between selective laser melting and traditional manufacturing for fabrication of metal parts: A review. *Frontiers of Mechanical Engineering*. 2015;10(2):111–125.
<https://doi.org/10.1007/s11465-015-0341-2>
 24. Wang X., Kustov S., Humbeeck J. Van. A short review on the microstructure, transformation behavior and functional properties of NiTi shape memory alloys fabricated by selective laser melting. *Materials (Basel)*. 2018;11(9):1683.
<https://doi.org/10.3390/ma11091683>
 25. Zhang C., Ozcan H., Xue L., Atli K.C., Arróyave R., Karaman I., Elwany A. On the effect of scan strategies on the transformation behavior and mechanical properties of additively manufactured NiTi shape memory alloys. *Journal of Manufacturing Processes*. 2022;84:260–271.
<https://doi.org/10.1016/j.jmapro.2022.09.051>
 26. Zhang Y., Attarilar S., Wang L., Lu W., Yang J., Fu Y. A review on design and mechanical properties of additively manufactured NiTi implants for orthopedic applications. *International Journal of Bioprinting*. 2021;7(2):1–28.
<https://doi.org/10.18063/ijb.v7i2.340>
 27. Logacheva A.I., Sentyurina Zh.A., Logachev I.A. Additive manufacturing technology responsible products from metals and alloys (review). *Perspektivnye Materialy*. 2015;5:5–15. (In Russ.).
 Логачева А.И., Сентюрина Ж.А., Логачев И.А. Аддитивные технологии производства ответственных изделий из металлов и сплавов (обзор). *Перспективные материалы*. 2015;5:5–15.
 28. Shtin V.I., Novikov V.A., Choynzonov E.L., Marchenko E.S., Stakheyeva M.N., Kucherova T.Ya., Menshikov K.Yu., Cheremisina O.V., Gribova O.V. Orbital wall reconstruction with titanium nickelide implants in cancer patients: characteristics of reparative processes and the potential for their management *Voprosy Onkologii*. 2023;69(2):259–267. (In Russ.).
<https://doi.org/10.37469/0507-3758-2023-69-2-259-267>
 Штин В.И., Новиков В.А., Чойнзонов Е.Л., Марченко Е.С., Стахеева М.Н., Кучерова Т.Я., Меньшиков К.Ю., Черемисина О.В., Грибова О.В. Эндопротезирование стенок орбиты имплантатами из никелида титана в онкологической практике: аспекты течения репаративных процессов и возможность управления последними. *Вопросы онкологии*. 2023;69(2):259–267.
<https://doi.org/10.37469/0507-3758-2023-69-2-259-267>

Information about the Authors

Eduard M. Farber – Engineer of the Laboratory “Synthesis of new materials and structures”, Peter the Great St. Petersburg Polytechnic University (SPbPU)

 **ORCID:** 0009-0007-8830-9887


 **E-mail:** d.farber2010@yandex.ru

Evgenii V. Borisov – Cand. Sci. (Eng.), Leading Researcher of the Laboratory “Synthesis of new materials and structures”, SPbPU

 **ORCID:** 0000-0003-2464-6706

 **E-mail:** evgenii.borisov@icloud.com

Anatoly A. Popovich – Dr. Sci. (Eng.), Professor, Director of the Institute of Machinery, Materials and Transport, SPbPU


 **ORCID:** 0000-0002-5974-6654

 **E-mail:** popovicha@mail.ru

Сведения об авторах

Эдуард Михайлович Фарбер – инженер лаборатории «Синтез новых материалов и конструкций» Санкт-Петербургского политехнического университета Петра Великого (СПбПУ)

 **ORCID:** 0009-0007-8830-9887

 **E-mail:** d.farber2010@yandex.ru

Евгений Владиславович Борисов – к.т.н., вед. науч. сотрудник лаборатории «Синтез новых материалов и конструкций» СПбПУ

 **ORCID:** 0000-0003-2464-6706

 **E-mail:** evgenii.borisov@icloud.com

Анатолий Анатольевич Попович – д.т.н., профессор, директор Института машиностроения, материалов и транспорта СПбПУ

 **ORCID:** 0000-0002-5974-6654

 **E-mail:** popovicha@mail.ru

Contribution of the Authors**Вклад авторов**

E. M. Farber – performing experiments, processing the obtained results, article writing, participating in the discussion of the results.

E. V. Borisov – planning the experiments, fabricating samples, participating in the discussion of the results.

A. A. Popovich – conceptualizing the idea, determining the purpose and objectives of the work, participating in the discussion of the results.

Э. М. Фарбер – проведение экспериментов, обработка полученных результатов, написание текста статьи, участие в обсуждении результатов.

Е. В. Борисов – планирование экспериментов, изготовление образцов, участие в обсуждении результатов.

А. А. Попович – концептуализация идеи, определение цели работы и ее задач, участие в обсуждении результатов.

Received 26.06.2023

Revised 19.01.2024

Accepted 23.01.2024

Статья поступила 26.06.2023 г.

Доработана 19.01.2024 г.

Принята к публикации 23.01.2024 г.



UDC 66.046.44

<https://doi.org/10.17073/1997-308X-2024-3-71-84>

Research article

Научная статья



Investigation of influence of technological parameters on the properties of SiC samples fabricated by selective laser sintering. Part 1

B. B. Bubnenkov¹, A. S. Zharmukhambetov¹, I. A. Ivanov¹, A. V. Yudin¹,
A. E. Taktashov¹, A. M. Starkov², I. S. Sharapov², E. M. Alekseeva²

¹ Joint Stock Company “Scientific and Production Association “Central Research Institute of Mechanical Engineering Technology (CRIMET)”

4 Sharikopodshipnikovskaya Str., Moscow 115088, Russia

² Joint Stock Company “Scientific Research Institute (SRI) Scientific and Production Association “LUCH”
24 Zheleznodorozhnaya Str., Podolsk, Moscow Region 142103, Russia

✉ bogis13@yandex.ru

Abstract. The paper describes experiments on selective laser sintering (SLS) of a high-temperature ceramic material – silicon carbide powder F320 – using the MeltMaster3D-160 SLS unit equipped with a fiber ytterbium laser with a peak power of 200 W. We investigated the sintering mechanism and the impact of technological parameters on the microstructure, phase composition, and density of the resulting 3D cubic samples. The technological properties of the initial powder were also investigated, including morphology, granulometric composition, bulk density, and flow rate. The powder morphology mainly consists of acicular particles with an aspect ratio of 1:5. Granulometric analysis revealed an average particle size of 48 μm . Measurements indicated that the bulk density reached $1.11 \pm 0.01 \text{ g/cm}^3$, approximately 36.6 % of the theoretical density value. The average time of powder outflow from the Hall funnel was $21.0 \pm 0.1 \text{ s}$, with 2–3 hits on the funnel during the measurement process. Experimental cubic samples of $10 \times 10 \text{ mm}$ were manufactured using 75 technological modes. Silicon carbide powder particles sinter due to the thermal effect of laser radiation and the release of SiC microparticles on the surface of the powder particles, with silicon (average size less than $1 \mu\text{m}$) prevailing in the composition, followed by mutual bonding of neighboring powder particles in the sintering region. X-ray phase analysis demonstrated that due to the laser radiation, the resulting 3D samples contain the following phases: SiC (6H), Si, and C. It was revealed that a scanning step larger than the actual spot diameter (spot diameter + thermal influence zone), 60–70 μm in size, causes the formation of unsintered areas between sintering tracks. The key parameters affecting the density index of the obtained samples are layer height, energy density, and scanning step. The best density index for the obtained samples is 86.7 % relative to the absolute density of the material (3.21 g/cm^3). Further research will be devoted to the development of techniques for post-processing the resulting porous samples-blanks to obtain a density close to 100 %.

Keywords: selective laser sintering, silicon carbide, high-temperature ceramics, technological properties of powder, laser energy density, porous ceramics

For citation: Bubnenkov B.B., Zharmukhambetov A.S., Ivanov I.A., Yudin A.V., Taktashov A.E., Starkov A.M., Sharapov I.S., Alekseeva E.M. Investigation of influence of technological parameters on the properties of SiC samples fabricated by selective laser sintering. Part 1. *Powder Metallurgy and Functional Coatings*. 2024;18(3):71–84.
<https://doi.org/10.17073/1997-308X-2024-3-71-84>

Исследование влияния технологических параметров на свойства образцов из SiC, получаемых методом селективного лазерного спекания. Часть 1

Б. Б. Бубненко¹, А. С. Жармухамбетов¹, И. А. Иванов¹, А. В. Юдин¹,
А. Е. Такташов¹, А. М. Старков², И. С. Шарапов², Е. М. Алексеева²

¹ АО «НПО «Центральный научно-исследовательский институт
технологии машиностроения (ЦНИИТМАШ)»

Россия, 115088, г. Москва, Шарикоподшипниковская, 4

² АО «НИИ НПО «ЛУЧ»

Россия, 142103, Московская обл., г. Подольск, Железнодорожная, 24

✉ bogis13@yandex.ru

Аннотация. Проведены эксперименты по селективному лазерному спеканию (СЛС) высокотемпературного керамического материала – порошка карбида кремния марки F320 – на СЛС-установке «Melt-Master3D-160», оснащенной волоконным иттербиевым лазером с пиковой мощностью 200 Вт. Изучены механизм спекания и влияние технологических параметров на микроструктуру, фазовый состав и плотность получаемых объемных кубических образцов. Исследованы технологические свойства исходного порошка с определением морфологии, гранулометрического состава, насыпной плотности и текучести. Морфология порошка представлена, в основном, игловидными частицами с соотношением сторон 1:5. Гранулометрическим анализом установлено среднее значение размера частиц 48 мкм. Насыпная плотность измерена на уровне $1,11 \pm 0,01$ г/см³, что составляет ~36,6 % от значения теоретической плотности. Среднее время истечения порошка из воронки Холла составило $21,0 \pm 0,1$ с при 2–3 ударах по воронке в процессе измерения при остановке течения порошка. Экспериментальные кубические образцы 10×10 мм изготавливались по 75 технологическим режимам. Спекание частиц порошка карбида кремния происходит за счет теплового воздействия лазерного излучения и выделения на поверхности частиц порошка микрочастиц SiC с преобладанием в составе кремния со средним размером <1 мкм при дальнейшем взаимном скреплении соседних частиц порошка в области спекания. По данным рентгенофазового анализа, в результате лазерного излучения получаемые объемные образцы содержат следующие фазы: SiC (6H), Si, C. Выявлено, что шаг сканирования, превышающий реальный диаметр пятна (диаметр пятна + зона термического влияния), составляющий 60–70 мкм, вызывает образование неспеченных областей между треками спекания. Ключевыми параметрами, влияющими на показатель плотности получаемых образцов, являются высота слоя, плотность энергии и шаг сканирования. Наилучший показатель плотности для полученных образцов – 86,7 % относительно абсолютной плотности вещества 3,21 г/см³. Последующие исследования будут связаны с разработкой технологии постобработки получаемых пористых образцов-заготовок с целью получения плотности, близкой к 100 %.

Ключевые слова: селективное лазерное спекание, карбид кремния, высокотемпературная керамика, технологические свойства порошка, плотность энергии лазера, пористая керамика

Для цитирования: Бубненко Б.Б., Жармухамбетов А.С., Иванов И.А., Юдин А.В., Такташов А.Е., Старков А.М., Шарапов И.С., Алексеева Е.М. Исследование влияния технологических параметров на свойства образцов из SiC, получаемых методом селективного лазерного спекания. Часть 1. *Известия вузов. Порошковая металлургия и функциональные покрытия*. 2024;18(3):71–84. <https://doi.org/10.17073/1997-308X-2024-3-71-84>

Introduction

Silicon carbide materials are used in various industries, including manufacture of critical duty products. This is due to their high compressive strength, dimensional stability, wear and heat resistance, thermal conductivity, heat stability, as well as chemical and radiation resistance. The listed properties determine their use as a material for gas turbine engine nozzles, bearings, working units of chemical pumps, atomizers, burners, cutting tools, pipelines, heat exchangers, heaters, and other critical applications.

The operating temperature range of pure silicon carbide material reaches $t = 1400 \div 1500$ °C in air,

and when high-temperature coatings are applied, it increases to 2000 °C and higher (depending on the type of coating, the aggressiveness of the oxidizing environment and the operating time) [1]. More technologically advanced composite silicon carbide materials, such as RS–SiC, can be operated in air at temperatures up to 1350 °C [2].

The bulk of silicon carbide products are manufactured by: simple sintering; activation sintering at $t \approx 1600 \div 1800$ °C of workpieces initially pressed from powder with sintering additives (Al_2O_3 , Y_2O_3 , Si_3N_4 and etc.); reaction sintering; hot pressing (HP); hot isostatic pressing (HIP); spark plasma sintering (SPS).

ring (SPS) – one of the types of hot pressing [3–5]. When HP and its varieties are used for molding products, silicon carbide powder in combination with sintering additives are applied to intensify compaction processes [3; 4; 6]. The process key features are high sintering temperature $\sim 1700\div 2000$ °C and pressure of $\sim 50\div 70$ MPa [3–5], while the exposure can take several hours. The methods based on HP are characterized by high performance, but they are limited to manufacturing products of simple geometric shapes and require the previous stage when an individual mold is fabricated for a specific part.

Additive technologies (AT) have an undeniable competitive edge over traditional ones, including fabricating products with complex geometries (branched topology), thin-walled products and the ones with closed cavities, which enables to solve a wide range of new design issues in the framework of modernization of the energy complex, military and space industries. There are direct and indirect At methods for manufacturing ceramic products.

The direct methods are the ones that require one stage to obtain a finished product – the product is manufactured on an additive unit with minimal subsequent mechanical processing or without it. Typically, the objective is to obtain completely dense products or the ones with a density of minimum 98 %. The following methods can yield this result: selective laser sintering (SLS) technology – selective layer-by-layer laser sintering of ceramic powder; micro-SLS process, which uses a laser scanning spot that is 2–3 times smaller than in traditional SLS [7]; SLS of a mixture of ceramic powder with a more fusible component, for example silicon, which ensures that during the sintering process, the pores of each of the product layers are filled [8]. The advantage of this approach is that it requires less production time and fewer resources due to reduced process steps.

Indirect methods include one or more operations for post-processing of a workpiece manufactured by the additive method. Post-processing typically includes 3 additional stages:

- 1) impregnation with a reagent;
- 2) reagent pyrolysis to form an additional carbon or silicon carbide framework;
- 3) molten silicon infiltration to ensure compaction and form the secondary silicon carbide as molten silicon interacts with free carbon released from the reagent [9].

Indirect methods include: selective layer-by-layer SLS of a mixture of ceramic and polymer powders followed by pyrolysis and molten silicon infiltration; SLS

of a mixture of ceramic powder and elements that form the main component during post-processing [10], followed by impregnation with polymer to fill the remaining pores, pyrolysis and silicon infiltration; light stereolithography (SLA) – selective layer-by-layer curing of a mixture of photopolymer and base material powder using a light source, followed by pyrolysis and silicon infiltration [11–14]; selective layer-by-layer binding of powder material (binder jetting – BJ) – applying glue on the powder layer, followed by pyrolysis and silicon infiltration [15–18]; extrusion (direct ink writing – DIW) of material (ceramic paste = powder + binder) using a print head, layer by layer, followed by pyrolysis and silicon infiltration [19–23].

With regard to the production of ceramic structural materials, direct and indirect SLS has a number of advantages compared to other 3D printing methods:

- fewer resources are required to prepare initial materials as powder components of the composition are used in their pure form and can be further processed and mixed under certain modes in specific proportions to obtain the required properties of the final product;
- minimum shrinkage coefficient relative to the CAD model that ensures high-accuracy manufacture of complex-profile products, including thin-walled ones;
- reduced free silicon content as a result of post-processing using reaction sintering technology, which helps to enhance the product strength and dimensional stability;
- reduced content of a polymer binder with a high carbon residue (if used), which during subsequent post-processing (pyrolysis) decreases stress across the cross-section of the workpiece during polymer decomposition, in contrast to BJ and SLA, which require significantly larger amount of binder for effective bonding of particles without high temperature, complicating the manufacture of thick-section and complex-profile products and causing problems with selecting the optimal post-processing parameters.

The advantages of SLS will significantly expand the range of products to synthesize from refractory, heat-, corrosion- and radiation-resistant materials based on silicon carbide, in terms of increased complexity of their geometry and topological optimization, and will also considerably reduce the amount of mechanical processing, which is critical for products with internal geometry and cavities where mechanical operations are difficult or impossible.

This technology is intended for manufacturing parts and components of nuclear and thermal energy equipment operating in aggressive environments at high

temperatures and pressures, for example, advanced reactors with molten salt as coolant (MSR) and acidic coolants (in alkaline coolants, residual silicon will transform into silicates and pollute it), as well as the equipment used in other fields.

We conducted a number of initial experiments to obtain samples from SiC using the direct SLS method and proved that 3D samples can be obtained using a Russian-made MeltMaster3D-160 unit (JSC SPA CRIMET, Moscow) from silicon carbide-based powder material produced by JSC “SRI SIA “LUCH” (Moscow). We also studied the impact of the unit technological parameters on the properties of the resulting samples.

The research was based on domestic and foreign experience in selective laser sintering of ceramic materials; the parameters for manufacturing samples were adjusted taking into account the characteristics of the unit and the materials used. The unit design was elaborated as the technological parameters for SiC-based material were developed.

For the first time, 3D silicon carbide samples were obtained using unconventional part construction modes. Based on the findings of the analysis, we provide recommendations on improving the manufacturing parameters to enhance the properties of the resulting samples.

Materials and methods of the experiment

Silicon carbide powder, graded F320 according to FEPA standard, served as the initial material for selective laser sintering.

The flow rate of powder was determined using a calibrated Hall funnel (according to GOST 20899-98). The prepared portion of the powder was poured into a funnel with a 5-mm outlet hole. In accordance with the standard, three measurements were made from three 50-g portions of powder.

Bulk density was assessed using a Scott volumeter. According to GOST 19440-94, three measurements were performed on three portions of powder from a sample with a volume of 100 cm³.

To determine the average particle size, as well as the particles distribution curve, a Laser Particle Sizer Analysette 22 MicroTec plus (Fritsch GmbH, Germany) was used in accordance with GOST R 8.777-2011. The measurements were conducted using a dispersion unit in a liquid medium, designed for measuring solid materials and suspensions in a liquid, mainly aqueous, medium. 2–3 measurements of the granulometric composition of the powders under study were performed and the results were averaged. The shape and

size of the particles were assessed using a Neophot 21 microscope (Carl Zeiss Jena, Germany) according to GOST 25849-83.

During the incoming inspection at the delivery stage and during the repeated circulating powder sieving, an ASV-200 sieve analyzer (NPK Mekhanobr-Tekhnika, St. Petersburg) with a set of sieves with a nominal value of 100 and 56 µm was used to separate the target fraction.

Before the SLS process, moisture was removed from the powder by drying it in an NK 7.7.7/3.5 oven (JSC Nakal – Industrial furnaces, Solnechnogorsk) at a temperature of 70–100 °C.

MeltMaster3D-160 unit made in Russia (JSC SPA CRIMET, Moscow) was used for SLS. The main characteristics of the unit: laser type – fiber; laser power – from 5 to 200 W; laser spot size – from 50 to 150 µm; scanning step – from 10 to 150 µm; scanning speed – from 50 to 1500 mm/s; approach increment of the construction platform – from 10 to 200 µm; protective atmosphere – nitrogen/argon/helium; platform heating – up to 120 °C; working area for sintering a part – 160×160×200 mm. Argon of purity 6.0 (99.9999 %) was used as the working gas.

Preparation for SLS. The powder was dried at a temperature of 100 °C before selective laser sintering of the samples.

To prepare and support the layer-by-layer prototyping of experimental samples on MeltMaster3D-160 unit, we used 3Ddigit specialized software package (JSC SPA CRIMET, Moscow) designed for placing a 3D model relative to the construction platform, forming supporting structures, setting technological parameters, cutting a 3D model into layers and generating the control code. The software functionality is responsible for automating all stages of layer-by-layer synthesis based on the original 3D model.

Additive production of samples using the SLS method includes the following steps:

- setting technological parameters in the software;
- checking the 3D model for integrity and correcting errors;
- placing the 3D model relative to the technological platform;
- creating technological support for the model;
- cutting a 3D model into layers;
- generating the control code;
- SLS process.

During preparation for printing, the working chamber was filled with an inert gas – argon, which enables

to process reactive materials. Reliable filtration and efficient circulation provided by the system of blowers ensure a high degree of gas purity. Thus, the selective laser sintering of laboratory sample blanks was performed in an argon atmosphere with a stable residual oxygen concentration of less than 700 ppm, to avoid the formation of SiO_2 under high-temperature laser action.

SLS process. Based on the analysis of domestic and foreign literary sources on SLS of ceramic materials, the initial set of parameters for the unit operation was selected, which was gradually changed based on the analysis of the microstructure and density of the resulting samples.

Experimental cubic samples of 10×10 mm were manufactured using 75 technological modes in order to study the impact of SLS process parameters on their density and microstructure. The following parameters were changed: laser power (P) in the range from 30 to 190 W, scanning speed (V) – from 100 to 1000 mm/s, scanning step (d) – the distance between tracks (line marks) – in the range from 20 to 150 μm , layer thickness (h) – from 20 to 60 μm . The combination of these parameters forms the energy density (E) of laser radiation:

$$E = \frac{P}{Vhd}.$$

The density of the manufactured samples was measured on Discovery DV215CD balance (OHAUS Corporation, USA) using the hydrostatic method according to GOST 25281-82 “Powder metallurgy. Method of determination of formings density”. First, the mass of the sample in air was determined. Then the sample was covered with a thin protective layer of vaselene to isolate the surface pores and to avoid

the formation of near-surface air bubbles, and its mass in air was measured again. The next step was weighing in distilled water at a fixed temperature. Based on the measurement results, the density of the samples was calculated taking into account the density of vaselene, water and air.

Microstructural studies and EDS analysis were performed using a Zeiss EVO 50 XVP scanning electron microscope (Carl Zeiss AG, Germany) with an attachment for energy dispersive analysis to determine the patterns of sintering and the impact of technological parameters on the microstructure of the resulting samples.

The D8 Discover diffractometer (Bruker Optic GmbH, Germany) with CuK_α -radiation was used to perform X-ray phase analysis in order to determine the final phase composition of the samples and to confirm the impact of manufacturing parameters on the phase composition. Bruker AXS DIFFRAC.EVA v. 4.1 software and ICDD PDF-2 international database were used for phase identification.

Results and discussion

The morphology of silicon carbide powder particles was analyzed using several visual fields (Fig. 1).

When viewed under a light microscope, SiC particles look like transparent green crystals without pores or inclusions (Fig. 1, *a*). Most of the particles are non-spherical and have a non-equiaxial/non-spherical or splintered shape; acicular particles with an aspect ratio up to 1:5 are also observed (Fig. 1, *b*). Some particles are joined into agglomerates, their size is larger than that of most particles. This morphology of particles cannot provide good flow rate or ensure the formation of a uniform powder layer. Also, such morphology

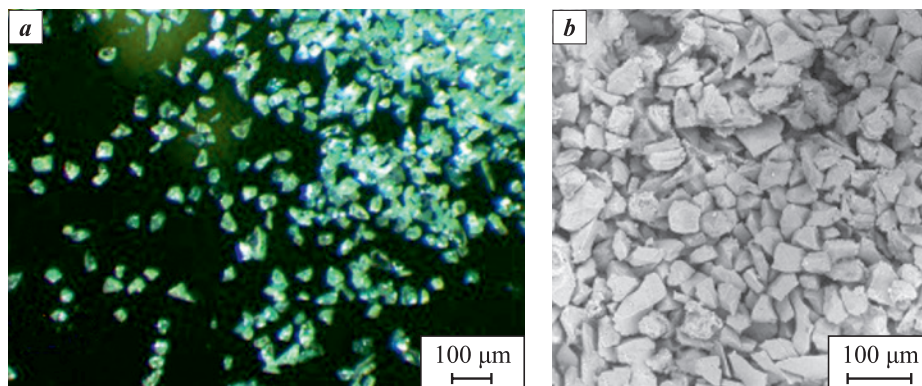


Fig. 1. Morphology of SiC powder (F320)

a – optical microscope ($\times 100$); *b* – electron microscope ($\times 420$)

Рис. 1. Морфология порошка SiC-порошка F320

a – оптический микроскоп ($\times 100$); *b* – электронный микроскоп ($\times 420$)

will affect the density characteristics of the resulting samples.

The agglomerates and non-equiaxial particles negatively affect the sintering characteristics of the material. The tendency to agglomerate is a natural property of powder particles, and the more non-equiaxed their shape is, the higher the tendency to agglomerate. Large agglomerates interfere with the process of “healing” pores during the sintering process, since the driving forces – their direction and speed – of the particles inside the agglomerate will significantly differ from those of the particles next to it. This difference leads to significant internal stresses, emergence of large pores or even the formation of microcracks. The dimensions of such defects and the resulting structural heterogeneity directly determine the density, strength and other properties of the material.

For this reason, before being used for the SLS process, the powder should be classified to recover the target fraction <60 µm by screening off large particle agglomerates.

Study of the granulometric composition.

The powder particles distribution was obtained (Table 1).

Table 1 shows that the average particle size of silicon carbide powder F320 under study, in the as-delivered condition is 48.2 µm. After 25 series of production processes, it slightly increases (by 7.2 µm) to 55.4 µm.

The sizes of fractions vary from 5 to 110 µm – this wide range is attributed to the powder particles being non-equiaxed and having a splintered or acicular shape. This spread is not a typical particle size distribution for the units operating based on the SLS method (20–63 µm), which can contribute to the formation of defects such as pores and voids and adversely affect the sample manufacturing process. Therefore, the target fraction <60 µm was recovered from the total mass of the powder by screen sizing. Acicular particles

cannot be removed from screen sizing using the sieve analysis. However, to be used in additive technologies, including SLS, these particles should be separated, and the remaining particles should be spheroidized, if possible.

Determination of the flow rate. The average time of the powder outflow from the Hall funnel could not be determined, since the outflow spontaneously stopped. Next, based on the standard, the funnel was hit once, but after some time the outflow of powder stopped. According to the standard, it means that the flow rate of the powder does not conform with the test method described in this standard.

Determination of bulk density. The bulk density of powders that do not flow spontaneously from a funnel with a hole 5 mm in diameter is measured using a volumeter according to GOST 19449-94.

The analysis of the bulk density of silicon carbide powder F320 showed that its average value (1.11 ± 0.01 g/cm³) accounts for ~36.6 % of the theoretical density of this material (the vibro-compacted density being 45 %). This bulk density value can be attributed to the fact that the powder contains a significant amount of acicular particles with a large aspect ratio and splintered particles: the former contribute to the emergence of “bridges” with voids underneath, while the latter, due to their roughness, additionally prevent powder distribution and its free spreading during layer formation.

The set of characteristics and properties of the powder used is presented below:

Average particle size, µm 48 ± 0.5
Flow rate, s None¹
Bulk density, g/cm³ 1.11 ± 0.01

Microstructural studies. Determining the size of the laser spot area and the effective scanning step.

As a result of microstructural studies (Fig. 2), it was revealed that the scanning step is larger than the actual spot diameter (spot diameter + heat-affected zone), which is 60–70 µm (Fig. 3), causes the formation of unsintered regions between the tracks. The width of these areas is comparable to the difference between the step size and the laser spot diameter. The unsintered regions significantly affect the samples density, as evidenced by the results of density determination.

¹ The average time of powder outflow from the Hall funnel was 21.0 ± 0.1 s with 2–3 hits on the funnel during the measurement process when the powder flow stopped. However, hits on the funnel are unacceptable according to GOST; therefore, it is generally assumed that the powder under study does not flow.

Table 1. Granulometric composition of SiC powder F320 in the initial state and after 25 cycles of use

Таблица 1. Гранулометрический состав порошка SiC марки F320 в исходном состоянии и после 25 циклов использования

Powder	D_{10} , µm	D_{50} , µm	D_{90} , µm	D_{avg} , µm
In the as-delivered condition	15.2	38.5	95.9	48.2
In the as-delivered condition after sieving	15.7	40.6	93.6	48.7
After 25 printing series	14.1	44.6	113.3	55.4

This effect may be associated with high thermal conductivity of the material, which prevents accumulation of the thermal energy in the scanned area (laser beam path) and its transfer to neighboring areas outside the spot diameter, where there was no direct exposure to laser radiation, as it was the case with metal powders. Laser radiation sinters powder particles to form a sintered region only in the area directly exposed

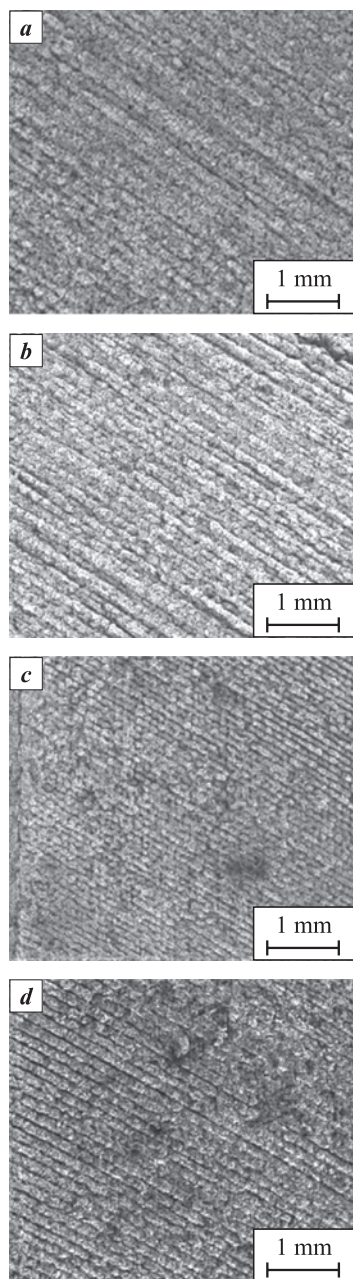


Fig. 2. Impact of the scanning step (d) on the sintering of SiC powder (F320) at a constant speed
 d , μm : $a - 75$; $b - 100$; $c - 125$; $d - 150$

Рис. 2. Влияние шага сканирования (d) на спекаемость порошка SiC марки F320 при постоянной скорости сканирования
 d , мкм: $a - 75$; $b - 100$; $c - 125$; $d - 150$

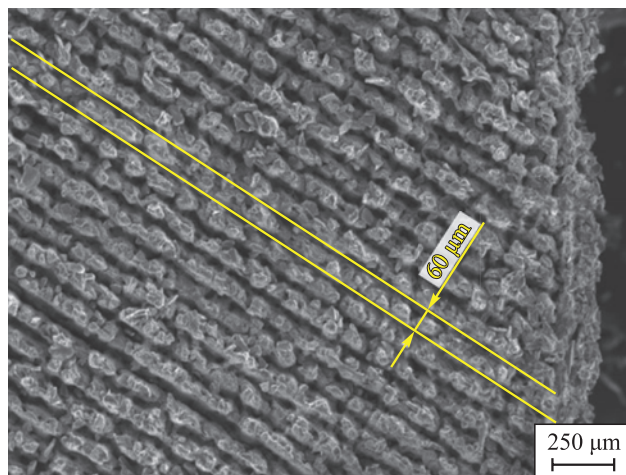


Fig. 3. Width of a single sintering zone as SiC powder is exposed to laser radiation

Рис. 3. Ширина единичной области спекания при воздействии лазерного излучения на порошок SiC

to the laser spot $+ 5 \div 10 \mu\text{m}$, then the heat flow follows the path of least resistance or, in other words, moves in the direction with greater thermal conductivity than that of freely poured powder. For this reason, thermal energy is most actively absorbed in the vertical direction by the previous, already sintered monolithic layers, which are denser and more thermally conductive compared to the area of unsintered powder surrounding the part and acting as a heat insulator with a relatively small degree of thermal absorption.

Sintering mechanism. Fig. 4 shows microphotographs of the surface of SiC powder particles after sintering in the resulting samples. Upon a detailed examination of the surface of the original powder particles, one can note that microparticles are formed, $1\text{--}7 \mu\text{m}$ in size, the shape being close to spherical, but with an uneven surface. They have a lighter shade than the particles of the original powder. These microparticles form clusters – areas with an increased number of cluster-shaped defects – on the surface of the original powder particles (including at the points of contact between them). The predominant size of the resulting microparticles is less than $1 \mu\text{m}$. Thus, we can conclude that after laser sintering, more defects emerge on the surface of the original powder particles.

It can be assumed that short-term high-temperature exposure of the SiC powder surface to laser radiation result in local overheating and micromelting with partial SiC decomposition. This assumption is also made in [24]. Further, as the locally overheated area cools down, the oval and spherical microparticles, lighter in color than SiC powder, form. They have a size of $1\text{--}7 \mu\text{m}$, sometimes less than $1 \mu\text{m}$, and a chemical composition identical to that of silicon carbide, with

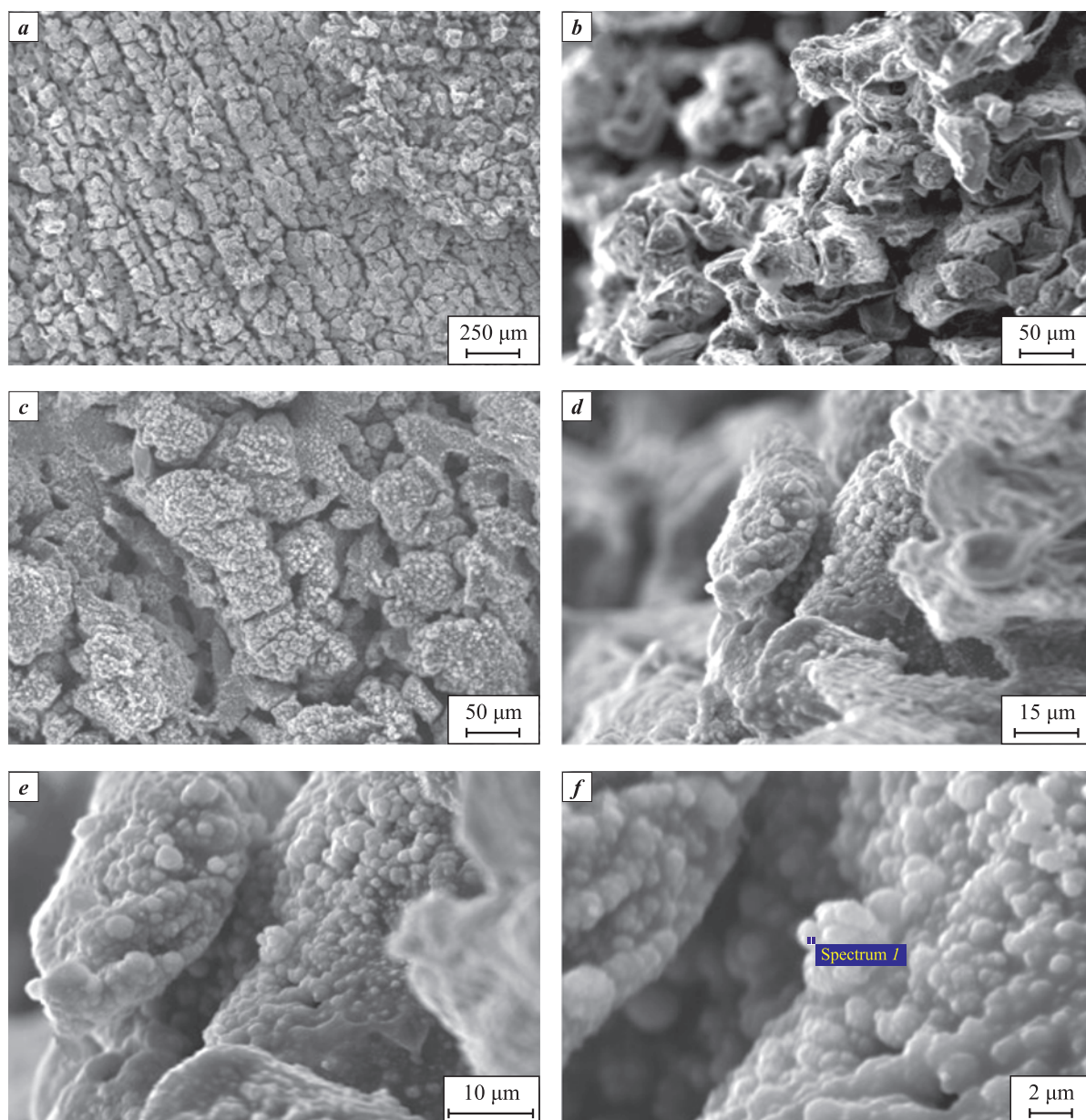


Fig. 4. Scaled representation of the mechanism of laser sintering of SiC powder particles

a – general view of the sample surface with visible strips – “tracks” of the laser passage;

b, c – images of large groups of sintered SiC powder particles with visible light areas on the powder particles surface;

d–f – detailed images of the surface of SiC particles after laser sintering, with clearly visible light microparticles on the surface of the initial powder

Рис. 4. Масштабное представление механизма лазерного спекания частиц порошка SiC

a – общий вид поверхности образца, различимы полосы – «треки» прохода лазера;

b, c – изображения больших групп спекленных порошковых частиц SiC, различимы светлые участки на поверхности частиц порошка;

d–f – детализированные изображения поверхности частиц SiC после лазерного спекания, отчетливо видны светлые микрочастицы на поверхности исходного порошка

silicon prevailing, as evidenced by the results of EDS analysis given in Table 2.

The SiC decomposition temperature is 2730 °C, and the Si and C melting temperatures are 1414 and 3367 °C, respectively. At the same time, in accordance with reference data [25], the vapor pressure of 100 kPa (~1 atm) is set at temperatures of 2613 and 4985 °C for silicon and carbon, respectively.

Therefore, when exposed to laser radiation, SiC powder presumably decomposes, while silicon simultaneously melts and evaporates. At the next stage, in accordance with the phase diagram, in the Si–C system the phase equilibrium during crystallization will shift to the “SiC + graphite” region.

There are two assumptions why oval and spherical precipitates with silicon dominating in the com-

Table 2. Results of EDS analysis of the surface of SiC powder particles after laser sintering
Таблица 2. Результаты ЭДС-анализа поверхности частиц порошка SiC после лазерного спекания

Spectrum	Content			
	wt. %		at. %	
	C	Si	C	Si
1	29.69	70.31	49.21	50.79
2	34.04	65.96	54.22	45.78
3	32.38	67.62	52.26	47.74
4	34.63	65.37	54.66	45.34
5	36.67	63.33	56.81	43.19
Max	36.67	70.31	56.81	50.79
Min	29.69	63.33	49.21	43.19

Spectrum	Content, wt. %	
	C	Si
1	24.6	75.4
2	28.2	71.8

position form: the first one is that ultra-fast cooling of the melt with undissolved graphite results in the formation of microparticles of non-stoichiometric $\text{SiC}_{(1-x)}$ depleted in carbon; the second is that silicon sweats out on the surface from the depths of the melt bath. Starting from the stage of SiC decomposition, Si concentrates in the near-surface zone and evaporates from the melt bath. When crystallization, initiated from the bath surface, starts, Si continues to sweat out, since the deep layers in contact with the bath are heated due to the high thermal conductivity of SiC.

Thus, during SLS of SiC powder, the sintering driving force is not the system (powder particles) striving to minimize surface energy and transit to a more equilibrium state, that is, to acquire a more spherical shape, reduce defects and gradually move towards the state of reciprocal slipping and consolidation. On the contrary, the interaction regions are formed at the contact boundary of powder particles from the more low-melting phase. These regions account for reciprocal slipping of powder particles during compaction and, at the final sintering stage as they cool down, they are “bound” as more defective cluster-like structures emerge at the point of contact and on the “free” surface of the particles, in contrast to the less defective

morphology of the particles before exposure to laser radiation (see Fig. 1). It should also be noted that compaction during sintering is not facilitated by the curvature of the surface of splintered SiC powder particles, which reduces the density of the initial layer and further compaction during mutual slipping of particles under the influence of laser radiation.

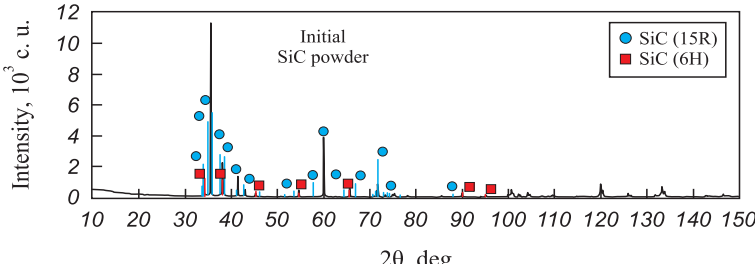
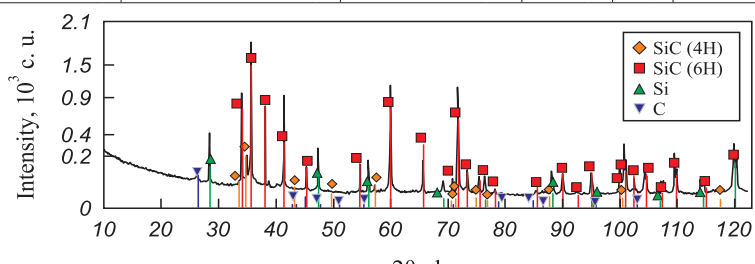
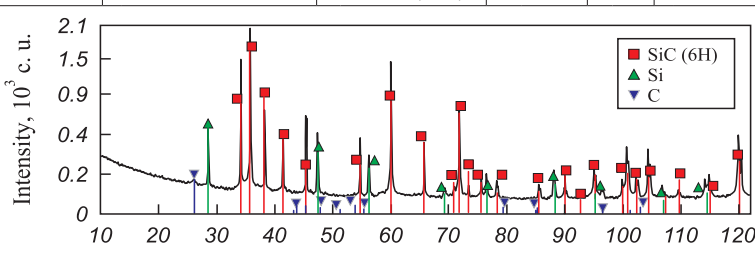
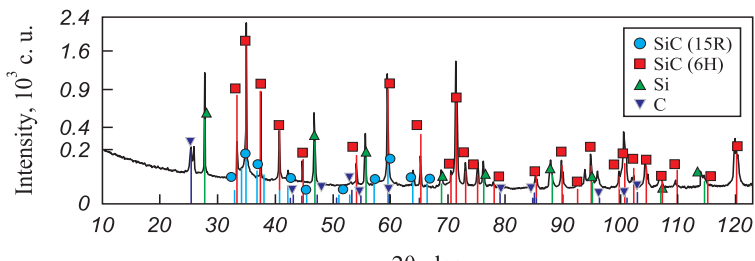
X-ray phase analysis. XRF was performed to determine the phase composition of the initial SiC powder, as well as to identify patterns of the impact of laser radiation on the composition of phases in samples after SLS. The results of X-ray phase analysis are presented in Table 3.

The samples revealed silicon Si, silicon carbide with a hexagonal crystal lattice of SiC (6H), traces of modification of SiC with a hexagonal lattice of SiC (4H), as well as (in some samples) traces of modification of silicon carbide with a rhombohedral lattice of SiC (15R), the position of flat layers in the structure of which it is repeated every third layer, not every second one, as in the hexagonal modification.

Also, the SiO_2 phase was detected in some samples, which may be due to insufficient oxygen purity of the working atmosphere or to the initial quality

Table 3. Phase composition of the initial SiC powder and SiC samples obtained by the SLS method

Таблица 3. Фазовый состав исходного порошка SiC и образцов, полученных из него методом СЛС

Sample	Phase	Crystal structure	Space group	Lattice parameter, pm			Phase amount, wt. %		
				<i>a</i>	<i>b</i>	<i>c</i>	SiC	Si	C
Initial SiC powder	SiC (6H)	HCP	<i>P63mc</i> (186)	3.0815	—	15.1185	100	—	—
	SiC (168R)	Rhombohedral	<i>R3m</i> (160)	3.0822	—	37.7446			
									
Test 8 sample No. 3	SiC (6H)	HCP	<i>P63mc</i> (186)	3.0852	—	15.1359	86.93	12.79	0.28
	SiC (4H)	HCP	<i>P63mc</i> (186)	3.0821	—	10.0804			
	Si	FCC	<i>Fd-3m</i> (227)	5.4344	—	—			
	C	HCP	<i>P63mc</i> (186)	2.4180	—	13.5203			
									
Test 23 sample No. 3	SiC (6H)	HCP	<i>P63mc</i> (186)	3.0777	—	15.1074	87.94	11.15	0.92
	Si	FCC	<i>Fd-3m</i> (227)	5.4263	—	—			
	C	HCP	<i>P63mc</i> (186)	2.4413	—	13.4977			
									
Test 24 sample No. 3	SiC (6H)	HCP	<i>P63mc</i> (186)	3.0815	—	15.1193	78.26	18.97	2.77
	SiC (15R)	Rhombohedral	<i>R3m</i> (160)	3.0802	—	37.8227			
	Si	FCC	<i>Fd-3m</i> (227)	5.4291	—	—			
	C	HCP	<i>P63mc</i> (186)	2.4206	—	13.5228			
									

of the supplied powder. However, this phase was not identified during incoming inspection, from which we can conclude that it probably emerged during the SLS process at the early stages, when the first layers of the sample were formed.

Determination of the density of SLS samples.

Our objective was to determine the impact of the unit technological parameters on the properties of the resulting samples, including the relative density. For this purpose, during the experiments, we performed statistical analysis, which revealed that the parameters such as speed (V), scanning step (d) and the height (thickness) of the layer (h) exert a decisive influence on the density of the resulting samples.

Based on the experimental data obtained, the graphs were plotted to show dependence of the samples' rela-

tive density on the technological parameters – scanning step, layer height and energy density (Fig. 5). It has been established that the density of the samples depends nonlinearly on the scanning step – as the scanning step increases, so does the density, reaching a peak at $d = 50\div 70\ \mu\text{m}$, and then it reduces. It is important that for this material, the scanning step significantly affects the density of the samples and cannot be considerably increased with a decrease in scanning speed due to the thermophysical properties of the material. On the contrary, there is a linear dependence of the samples' density on the layer height – as the height increases, the density reduces. Speaking about the impact of the layer height, we should note the stage-by-stage selection of the optimal value of this parameter. The choice of $h = 30\ \mu\text{m}$ contributed to higher density of the samples and lower delamination between the sintered layers. There is a certain peak value for the energy density, as well as for the scanning step, after which these values plummet, which is also typical for other materials [26; 27].

The best density index for the obtained samples is 86.7 % relative to the absolute density of the material ($3.21\ \text{g/cm}^3$). This result exceeds the values of foreign studies of previous years, and is also consistent with the data of foreign publications [28–31]. It should be noted that we used pure SiC powder without a binder and the shape of the powder particles had a large aspect ratio (up to 1:5). Despite this, we succeeded in achieving fairly high density values of the resulting samples given the material and technique used. In the future, the samples density can be increased by refining the unit and manufacturing parameters, improving the composition and quality of the initial materials, as well as by developing the technique for post-processing of the resulting samples.

Conclusions

1. This study proved that samples-blanks can be formed from silicon carbide powder by the SLS method without using a binder. The resulting SLS blanks have a density of up to 86.7 %, which can be increased by subsequent reaction sintering at temperatures from 1600 to 1800 °C.

2. A set of technological parameters affecting the properties of the resulting samples was determined: scanning speed, scanning step and layer height.

3. One of the factors limiting an increase in the samples density is the combination of properties of the initial powder material – particle morphology and a wide size range, which results in insufficient density when the layer is formed. As a consequence, additional pores emerge after SLS.

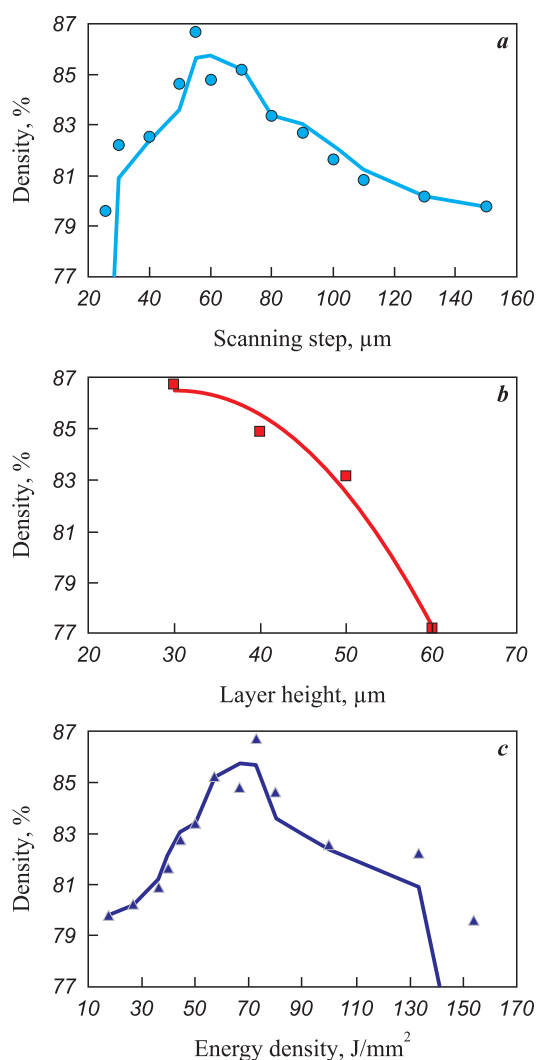


Fig. 5. Main dependences of the density of silicon carbide samples on technological parameters (a, b) and energy density (c)

Рис. 5. Основные зависимости плотности образцов из карбида кремния от технологических параметров (a, b) и плотности энергии (c)

4. When exposed to laser radiation, the silicon carbide powder particles sinter due to the decomposition of SiC (6H; 15R) into C, Si and SiC of another modification (4H), as confirmed by X-ray diffraction data. However, it should be noted that, according to EDS data, non-stoichiometric SiC_(1-x), with silicon prevailing in the composition, can form. Decomposition products are present on the surface of the original powder particles in the form of microparticles with an average size of less than 1 μm. The formation of more low-melting phases Si and, probably, SiC_(1-x) on the surface of the initial powder result in mutual slipping and compaction of powder particles in the sintering region, followed by relative binding during crystallization.

5. Further research will involve improvement of the technological characteristics of the initial materials and development of the technique for post-processing of the samples obtained during SLS.

References / Список литературы

1. Droillard C., Lamon J. Fracture toughness of 2-D woven SiC/SiC CVI-composites with multilayered interphases. *Journal of the American Ceramic Society*. 1996; 79(4):849–858.
<https://doi.org/10.1111/j.1151-2916.1996.tb08516.x>
2. Gnesin G.G. Silicon carbide materials. Moscow: Metallurgiya, 1977. 215 p. (In Russ.).
Гнесин Г.Г. Карбидокремниевые материалы. М.: Металлургия, 1977. 215 с.
3. Šajgalík P., Sedláček J., Lenčes Z., Dusza J., Lin H.-T. Additive-free hot-pressed silicon carbide ceramics – A material with exceptional mechanical properties. *Journal of the European Ceramic Society*. 2016;36(6):1333–1341.
<https://doi.org/10.1016/j.jeurceramsoc.2015.12.013>
4. Hayun S., Paris V., Mitrani R., Kalabukhov S., Darinel M.P., Zaretsky E., Frage N. Microstructure and mechanical properties of silicon carbide processed by Spark Plasma Sintering (SPS). *Ceramics International*. 2012;38(8):6335–6340.
<https://doi.org/10.1016/j.ceramint.2012.05.003>
5. Li J.F., Sugimoto S., Tanaka S., Esashi M., Watanabe R. Manufacturing silicon carbide microrotors by reactive hot isostatic pressing within micromachined silicon molds. *Journal of the American Ceramic Society*. 2004;85(1):261–263.
<https://doi.org/10.1111/j.1151-2916.2002.tb00077.x>
6. Saleem A., Zhang Y., Gong H., Majeed M.K. Fluoride doped SiC/Si₃N₄ composite as a high thermal conductive material with enhanced mechanical properties. *Ceramics International*. 2019;45(16):21004–21010.
<https://doi.org/10.1016/j.ceramint.2019.06.289>
7. Streek A., Regenfuss P., Ullmann F., Hartwig L., Ebert R., Exner H. Processing of silicon carbide by laser micro sintering. In: 2006 International Solid Freeform Fabrication Symposium (17th Solid Freeform Fabrication Symposium, Austin, Texas, USA, 14–16 August 2006). 2006. P. 349–358. <https://doi.org/10.26153/tsw/7144>
8. Song S., Gao Z., Lu B., Bao C., Zheng B., Wang, L. Performance optimization of complicated structural SiC/Si composite ceramics prepared by selective laser sintering. *Ceramics International*. 2019;46(1):568–575.
<https://doi.org/10.1016/j.ceramint.2019.09.004>
9. Pelanconi M., Colombo P., Ortona A. Additive manufacturing of silicon carbide by selective laser sintering of PA12 powders and polymer infiltration and pyrolysis. *Journal of the European Ceramic Society*. 2021; 41(10):5056–5065.
<https://doi.org/10.1016/j.jeurceramsoc.2021.04.014>
10. Zhang K., Zeng T., Xu G., Cheng S., Yu S. Mechanical properties of SiC_p/SiC composite lattice core sandwich panels fabricated by 3D printing combined with precursor impregnation and pyrolysis. *Composite Structures*. 2020;240:112060.
<https://doi.org/10.1016/j.compstruct.2020.112060>
11. Tang J., Guo X., Chang H., Hu K., Shen Z., Wang W., Liu M., Wei Y., Huang Z., Yang Y. The preparation of SiC ceramic photosensitive slurry for rapid stereolithography. *Journal of the European Ceramic Society*. 2021; 41(15):7516–7524.
<https://doi.org/10.1016/j.jeurceramsoc.2021.08.029>
12. Bai X., Ding G., Zhang K., Wang W., Zhou N., Fang D., He R. Stereolithography additive manufacturing and sintering approaches of SiC ceramics. *Open Ceramics*. 2021;5:100046.
<https://doi.org/10.1016/j.oceram.2020.100046>
13. Ding G., He R., Zhang K., Zhou N., Xu H. Stereolithography 3D printing of SiC ceramic with potential for lightweight optical mirror. *Ceramics International*. 2020;46(11B):18785–18790.
<https://doi.org/10.1016/j.ceramint.2020.04.196>
14. Chen R., Lian Q., Li D., He X., Wang S., Zhuang J. Stereolithographic additive manufacturing diamond/SiC composites with high thermal conductivity for electronic 3D-packaging applications. *Ceramics International*. 2021;47(10A):14009–14020.
<https://doi.org/10.1016/j.ceramint.2021.01.270>
15. Thomas J., Banda M., Du W., Yu W., Chuang A., France D.M., Singh D. Development of a silicon carbide ceramic based counter-flow heat exchanger by binder jetting and liquid silicon infiltration for concentrating solar power. *Ceramics International*. 2022;48(16):22975–22984.
<https://doi.org/10.1016/j.ceramint.2022.04.269>
16. Feng K., Hu S., Li L., Mao Y., Heng Y., Yuan J., Wu J., Wei Q. Preparation of low residual silicon content Si–SiC ceramics by binder jetting additive manufacturing and liquid silicon infiltration. *Journal of the European Ceramic Society*. 2023;43(13):5446–5457.
<https://doi.org/10.1016/j.jeurceramsoc.2023.05.038>
17. Oh J.-W., Park J., Nahm S., Choi H. SiC–Si composite part fabrication via SiC powder binder jetting additive manufacturing and molten-Si infiltration. *International Journal of Refractory Metals and Hard Materials*. 2021;101:105686.
<https://doi.org/10.1016/j.ijrmhm.2021.105686>
18. Zheng C., Lee J.-K., Nettleship I. Three-dimensional characterization of the pore structures in SiC formed by binder jet 3D printing, polymer infiltration and pyrolysis (PIP). *Journal of the European Ceramic Society*. 2023;

- 43(10):4255–4262.
<https://doi.org/10.1016/j.jeurceramsoc.2023.03.041>
19. Chen H., Wang X., Xue F., Huang Y., Zhou K., Zhang D. 3D printing of SiC ceramic: Direct ink writing with a solution of preceramic polymers. *Journal of the European Ceramic Society*. 2018;38(16):5294–5300.
<https://doi.org/10.1016/j.jeurceramsoc.2018.08.009>
 20. Ma S., Liu X., Fu S., Zhao S., He P., Duan X., Yang Z., Jia D., Colombo P., Zhou Y. Direct ink writing of porous SiC ceramics with geopolymer as binder. *Journal of the European Ceramic Society*. 2022;42(15):6815–6826.
<https://doi.org/10.1016/j.jeurceramsoc.2022.08.004>
 21. Held A., Puchas G., Müller F., Krenkel W. Direct ink writing of water-based C–SiC pastes for the manufacturing of SiSiC components. *Open Ceramics*. 2021;5:100054.
<https://doi.org/10.1016/j.oceram.2020.100054>
 22. Kemp J.W., Diaz A.A., Malek E.C., Croom B.P., Apostolov Z.D., Kalidindi S.R., Compton B.G., Rueschhoff L.M. Direct ink writing of ZrB₂–SiC chopped fiber ceramic composites. *Additive Manufacturing*. 2021;44:102049.
<https://doi.org/10.1016/j.addma.2021.102049>
 23. Petrie C.M., Schrell A.M., Leonard D.N., Yang Y., Jolly B.C., Terrani K.A. Embedded sensors in additively manufactured silicon carbide. *Journal of Nuclear Materials*. 2021;552:153012.
<https://doi.org/10.1016/j.jnucmat.2021.153012>
 24. Zarazag A.M., Abdelmoula M., Küçüktürk G., Maury F., Grossin D., Ferrato M. Experimental and numerical study for direct powder bed selective laser processing (sintering/melting) of silicon carbide ceramic. *Materials Research Express*. 2021;8(4):045603.
<https://doi.org/10.1088/2053-1591/abf6fc>
 25. Babichev A.P., Babushkina N.A., Bratkovsky A.M. Physical quantities: Reference book. Eds. I.S. Grigoriev, E.Z. Meilikhov. Moscow: Energoatomizdat, 1991. 1232 p. (In Russ.).
 Баби́чев А.П., Бабу́шкина Н.А., Бра́тковский А.М. Физические величины: Справочник. Под ред. И.С. Григорьева, Е.З. Мейлихова. М.: Энергоатомиздат, 1991. 1232 с.
 26. Wang D., Feng Y., Liu L., Wei X., Yang Y., Yuan P., Liu Y., Han C., Bai Y. Influence mechanism of process parameters on relative density, microstructure, and mechanical properties of low Sc-content Al–Mg–Sc–Zr alloy fabricated by selective laser melting. *Chinese Journal of Mechanical Engineering: Additive Manufacturing Frontiers*. 2022;1(4):100034.
<https://doi.org/10.1016/j.cjmeam.2022.100034>
 27. Xie M., Li F., Zhou S., Lu L., Peng F., Zhang L., Zhang Y., Lu Y. Effect of laser energy density on microstructure and properties Cu–Fe–P immiscible alloys fabricated by laser selective melting: heterogeneous and high strength and magnetic. *Journal of Materials Research and Technology*. 2023;26:2759–2769.
<https://doi.org/10.1016/j.jmrt.2023.08.080>
 28. Koyanagi T., Terrani K., Harrison S., Liu J., Kato Y. Additive manufacturing of silicon carbide for nuclear applications. *Journal of Nuclear Materials*. 2021;543:152577.
<https://doi.org/10.1016/j.jnucmat.2020.152577>
 29. Abdelmoula M., Zarazag A.M. Scanning strategy investigation for direct powder bed selective laser processing of silicon carbide ceramic. *Applied Sciences*. 2022;12(2):788. <https://doi.org/10.3390/app12020788>
 30. Abdelmoula M., Küçüktürk G., Grossin D., Zarazag A.M., Maury F., Ferrato M. Direct selective laser sintering of silicon carbide: Realizing the full potential through process parameter optimization. *Ceramics International*. 2023;49(20):32426–32439.
<https://doi.org/10.1016/j.ceramint.2023.07.189>
 31. Zarazag A.M., Abdelmoula M., Küçüktürk G., Maury F., Ferrato M., Grossin D. Process parameters investigation for direct powder bed selective laser processing of silicon carbide parts. *Progress in Additive Manufacturing*. 2022;7:1307–1322.
<https://doi.org/10.1007/s40964-022-00305-7>

Information about the Authors




Bogdan B. Bubnenkov – Junior Research Scientist, Institute of Metallurgy and Mechanical Engineering (IMME), JSC “SPA “Central Research Institute of Mechanical Engineering Technology (CRIMET)”

 **ORCID:** 0009-0001-4963-4229


 **E-mail:** bogis13@yandex.ru

Alps S. Zharmukhambetov – Head of the Laboratory of Additive Technologies, IMME of JSC “SPA “CRIMET”

 **ORCID:** 0009-0002-1977-2492


 **E-mail:** alps98@mail.ru

Ivan A. Ivanov – Cand. Sci. (Phys-Math.), Associate Professor, Director of IMME, Deputy General Director of JSC “SPA “CRIMET”

 **ORCID:** 0000-0001-9083-1059

 **E-mail:** ivalivanov@rosatom.ru

Artem V. Yudin – Deputy Director of IMME of JSC “SPA “CRIMET”

 **ORCID:** 0000-0002-0225-4771

 **E-mail:** avudin@cniitmash.com


Сведения об авторах

Богдан Борисович Бубненко – мл. науч. сотрудник Института металлургии и машиностроения (ИМиМ) АО «НПО «Центральный научно-исследовательский институт технологии машиностроения (ЦНИИТМАШ)»

 **ORCID:** 0009-0001-4963-4229


 **E-mail:** bogis13@yandex.ru

Алпс Савырович Жармухамбетов – зав. лабораторией аддитивных технологий ИМиМ, АО «НПО ЦНИИТМАШ»

 **ORCID:** 0009-0002-1977-2492

 **E-mail:** alps98@mail.ru

Иван Алексеевич Иванов – к.ф.-м.н., доцент, директор ИМиМ, зам. генерального директора АО «НПО ЦНИИТМАШ»

 **ORCID:** 0000-0001-9083-1059

 **E-mail:** ivalivanov@rosatom.ru

Арте́м Викторович Юди́н – зам. директора ИМиМ по новым технологиям, АО «НПО ЦНИИТМАШ»

 **ORCID:** 0000-0002-0225-4771

 **E-mail:** avudin@cniitmash.com

Andrey E. Taktashov – Head of the Department of IMME of JSC “SPA “CRIMET”

ORCID: 0009-0002-8948-5229

E-mail: aetaktashov@cniitmash.com

Alexey M. Starkov – Head of the group, JSC “SRI SPA “LUCH”

ORCID: 0009-0002-0827-5546

E-mail: StarkovAM@sialuch.ru

Ilya S. Sharapov – Deputy Director of the Department, JSC “SRI SPA “LUCH”

ORCID: 0009-0005-7449-6517

E-mail: SharapovIS@sialuch.ru

Elena M. Alekseeva – Engineer of JSC “SRI SPA “LUCH”

ORCID: 0009-0007-1731-6481

E-mail: AlekseevaEM@sialuch.ru

Андрей Евгеньевич Такташов – начальник участка ИМиМ, АО «НПО ЦНИИТМАШ»

ORCID: 0009-0002-8948-5229

E-mail: aetaktashov@cniitmash.com

Алексей Михайлович Старков – начальник группы АО «НИИ НПО «ЛУЧ»

ORCID: 0009-0002-0827-5546

E-mail: StarkovAM@sialuch.ru

Илья Сергеевич Шарапов – зам. директора отделения АО «НИИ НПО «ЛУЧ»

ORCID: 0009-0005-7449-6517

E-mail: SharapovIS@sialuch.ru

Елена Михайловна Алексеева – инженер АО «НИИ НПО «ЛУЧ»

ORCID: 0009-0007-1731-6481

E-mail: AlekseevaEM@sialuch.ru

Contribution of the Authors



Вклад авторов

B. B. Bubnenkov – conducting experiments and research, processing the results, writing the article.

A. S. Zharmukhambetov – conducting experiments and research, processing the results, writing the article.

I. A. Ivanov – determining the purpose of the work, supervising the research, participating in the discussion of the results.

A. V. Yudin – determining the purpose of the work, supervising the research and modernizing the SLS unit, participating in the discussion of the results.

A. E. Taktashov – conducting experiments, modernizing the SLS unit, supervising the research, participating in the discussion of the results.

A. M. Starkov – preparing initial raw materials for SLS, conducting experiments and research, supervising the research, participating in the discussion of the results, writing the article.

I. S. Sharapov – determining the purpose of the work, supervising the research, participating in the discussion of the results.

E. M. Alekseeva – conducting experiments, participating in the refinement of the laser-optical system for the SLS unit, participating in the discussion of the results, writing the article.

Б. Б. Бубненко – проведение экспериментов и исследований, обработка результатов, написание статьи.

А. С. Жармухамбетов – проведение экспериментов и исследований, обработка результатов, написание статьи.

И. А. Иванов – определение цели работы, курирование исследований, участие в обсуждении результатов.

А. В. Юдин – определение цели работы, контроль и модернизация установки СЛС, участие в обсуждении результатов.

А. Е. Такташов – проведение экспериментов, осуществление модернизации установки СЛС, координирование работ, участие в обсуждении результатов.

А. М. Старков – подготовка исходного сырья для СЛС, проведение экспериментов и исследований, курирование работы, участие в обсуждении результатов, написание статьи.

И. С. Шарапов – определение цели исследований, курирование работы, участие в обсуждении результатов.

Е. М. Алексеева – проведение экспериментов, участие в доработке лазерно-оптической системы установки СЛС, участие в обсуждении результатов, написание статьи.

Received 30.09.2023

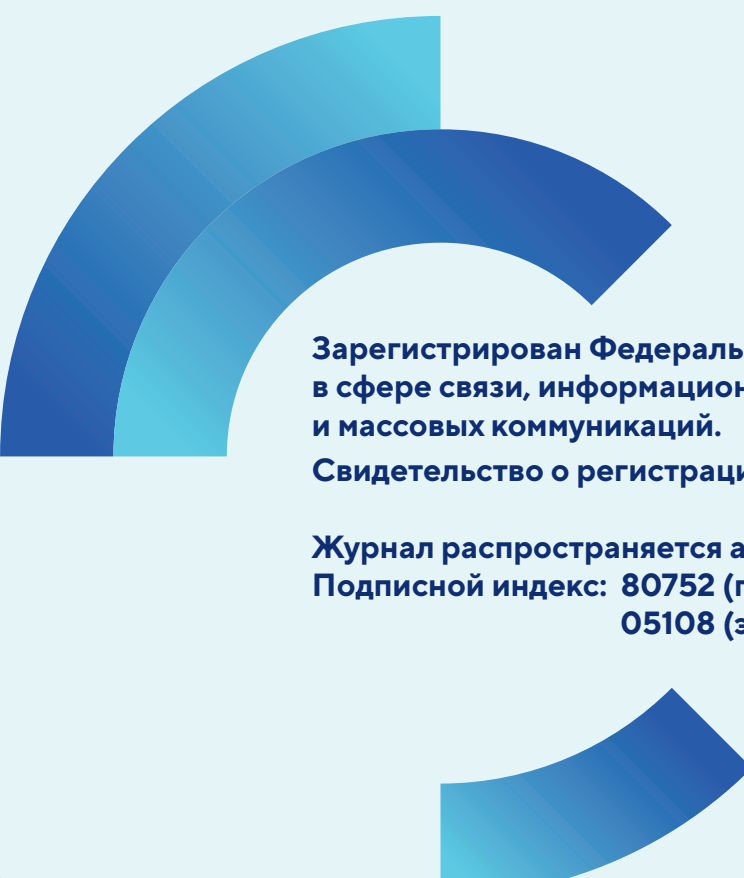
Revised 06.03.2024

Accepted 11.03.2024

Статья поступила 30.09.2023 г.

Доработана 06.03.2024 г.

Принята к публикации 11.03.2024 г.



**Зарегистрирован Федеральной службой по надзору
в сфере связи, информационных технологий
и массовых коммуникаций.**

Свидетельство о регистрации ПИ № ФС77-79230

**Журнал распространяется агентством «Урал-Пресс»
Подписной индекс: 80752 (печатная версия)
05108 (электронная версия)**